University of Alberta

Continuous Wave Terahertz Frequency Spectroscopy and Imaging for Explosives Detection and Security Screenings

by

Michael Andrei Startsev

A thesis submitted to the Faculty of Graduate Studies and Research
in partial fulfillment of the requirements for the degree of

Master of Science
in
Photonics and Plasmas

Electrical and Computer Engineering

Fall 2011
Edmonton, Alberta

Abstract

Continuous-wave terahertz (THz) spectroscopy was performed on high explosive materials using the Firefly-THz optical parametric oscillator (OPO). Cyclotetramethylene-tetranitramine (HMX), cyclotrimethylene-trinitramine (RDX), pentaerythritol-tetranitrate (PETN) and Composition-4 were scanned under experimental conditions modeling “real world” security screenings. Spectroscopy of RDX yielded broad spectral signatures at 0.83, 1.04, and 1.50 THz. HMX and PETN displayed singular spectral peaks of 1.45 and 1.78 THz, respectively. The OPO’s viability for use as a security system was further evaluated through demonstrations of concealed explosive spectroscopy, and raster scan imaging. A lamellar mirror interferometer was designed and constructed to investigate the system’s frequency range limitations. The interferometric scans concluded that, using Golay cell detection methods, the system could utilize coherent radiation between 0.75 and 1.8 THz. Lastly, a prototype external camera circuit was designed to further the development of a THz frequency camera system capable of both imaging and spectroscopy simultaneously.

Acknowledgments:

Sincerest thanks to my supervisor, Dr. Abdulhakem Elezzabi. Throughout my project, he has provided invaluable support, advice and guidance. Not only did he make this work possible, he was my greatest influence and insight into the world of research.

I also wish to thank the personnel in the University of Alberta machine shop: Herbert Dexel and Reiner Shwarze, for their exceptional craft and technical design suggestions.

Thanks to Edward Tiong for assistance with electrical circuit design and for permitting me to use his facilities to test circuits and upload code to microchip processors.

Thanks to Keith Franklin, Scott Munroe and Stephanie Bozic for nanofabrication laboratory equipment training and assistance.

Thanks to Explosives Technician, Sergeant Grant Jongejan from the Edmonton Police Force for assisting with the explosive sample preparation and acquisition.

Finally, thanks to my colleagues: Cameron Straatsma, Pouya Maraghechi, and Shawn Sederberg; for their camaraderie, encouragement, and countless thoughtful discussions.

TABLE OF CONTENTS

Chapter 1 .... **1**

1.1 Motivation 1

1.2 Background and Research Progress.. 5

1.3 Theoretical Framework 15

1.3.1 Molecular Model 16

1.3.2 Molecular Vibrations 17

1.3.3 Molecular Rotations 19

1.3.4 Rotational Vibrational Spectra.................................... 20

1.3.5 Normal Modes of Vibration.. 24

1.3.6 Spectral Assertions 27

1.3.6.1 Bulk Explosives Spectroscopy Considerations 27

1.3.6.2 Absorption Strengths 28

1.3.6.3 Spectral Line Broadening 29

1.3.6.4 Scattering Effects 30

1.4 Bulk Explosives Under Investigation 31

1.5 Thesis Scope 37

Chapter 2: Optical Parametric Oscillation Spectroscopy System **39**

2.1 Mechanism of Optical Parametric Oscillations................................... 39

2.2 OPO System Performance 42

2.3 THz Split Mirror Interferometer 52

2.3.1 Basic Theory of FT Interferometry 54

2.3.2 Design of Lamellar Mirror Interferometer 56

2.3.3 Data Collection and Methodology 61

2.3.4 Interferometry Results and Discussion 62

2.3.5 Interferometer Motor Control GUI 70

2.3.6 Future Prospects for the Lamellar Interferometer 73

Chapter 3: Continuous Wave and Time Domain Terahertz Spectroscopy 74

3.1 Explosive Sample Preparation 75

3.2 Methodology for CW Spectroscopy Experiments 76

3.3 Discussion of CW Spectroscopy Results 79

3.4 Origin Software Lorentzian Algorithm 87

3.5 Threshold of Thickness for Explosives Detection 95

3.5.1 Discussion of Threshold Experiments 95

3.6 Concealed Explosives Spectroscopy 100

3.7 Continuous Wave Terahertz Radiation Imaging 102

3.8 Terahertz Time Domain Spectroscopy (THz-TDS) 107

3.8.1 Comparison of TDS Results to CW Spectroscopy Results 114

Chapter 4: Circuit for THz Frequency Radiation Video Camera **118**

4.1 Lack of Suitable THz Frequency Detectors 119

4.2 Proposed THz Frequency Detectors for the Circuit Design 120

4.3 Design Constraints 120

4.4 Circuit Design 122

4.5 Frame Rate Considerations 133

Chapter 5: Summary **134**

Bibliography 141

Appendix A: Photographs of lamellar split mirror 155

Appendix B: Multiplexing program for PIC16 microchip design 158

Appendix C: Multiplexing Program for Arduino Microchip 170

Appendix D: Spectrocopic Scan Program 175

Appendix E: Interferometer Motor Control Code 179

Appendix F: Photographs of Circuit Designs for THz Video Camera 190

LIST OF TABLES

Number Page

1.2.0.1: Summary of the combined findings of Liu et al. attained through THz spectroscopy and Fourier Transform Infrared (FTIR) spectrometer (Bruker IFS 55 V/S) across the frequency range 0.1 – 21 THz.. 11

3.3.0.1**:** Absorption spectral peaks found in spectroscopic experiments performed in this work compared to the peaks that are expected from previous THz spectroscopic studies.................84

3.4.0.2: Lorentz fit algorithm (Origin software) peak values and FWHM values for each explosive compared to the spectral peaks obtained by observing the local peak values. 92

LIST OF FIGURES

Number Page

1.2.0.1: The plot on the left (a) shows the results of THz spectroscopy performed on explosives by Tribe. The plot on the right (b) are the results collected by Liu et al. The (a) peaks have been annotated with the publication's tabulated peak values for clarity. Note that the studies used similar methods of TDS spectroscopy but yielded differing results.. 10

1.2.0.2: Illustration of six lowest energy normal modes of vibrations for an RDX molecule derived from solid-state computational simulation of THz spectra. The simulated results show THz frequency spectral peaks that are shifted to higher frequencies in comparison to the empirically observed spectra. From Allis et al. 14

1.2.0.3: Simulated solid-state DFT spectrum of RDX shown with superimposed 298K and 7K experimental RDX spectra. 15

1.3.2.1: Potential energy with discrete energy states for linear harmonic oscillator. 19

1.3.4.1: Potential energy diagram for harmonic and anharmonic oscillator. 22

1.3.4.2: Term scheme of combined rotation and vibration oscillator for the transition $G(n=1, J \pm 1) \leftarrow G(n=0, J)$ 23

1.3.5.1: Vibrational modes (v_1, …v_R) of nonlinear (above) and linear (below) triatomic molecules. The Linear molecule exhibits four vibrational modes while the nonlinear has three vibrational and one rotational mode. 26

1.4.0.1: Illustration of potential implementation of THz for explosives detection in (a) reflection mode and (b) transmission mode. 33

1.4.0.2: Chemical structure diagrams of cyclotrimethylene-trinitramine (RDX), pentaerythritol tetranitrate (PETN), and cyclotetramethylene-tetranitramine (HMX). Composition 4 (C-4) explosive not shown since it is composed of an RDX mixture. 36

2.1.0.1: Schematic of non-colinear, intersecting cavity within the Firefly-THz optical parametric oscillator (OPO). 41

2.2.0.1: The intensity-frequency profile of the Firefly-THz OPO. A Golay cell was used to detect the signal strength directly from the THz output window. Power was determined from the Golay cell voltage signal using a responsivity of 21KV/W specified for a 50 Hz repetition rate. 45

2.2.0.2: Power from the auxiliary infrared output window vs the THz frequency tuning of the OPO. The general shape of the IR power should follow the THz profile (Figure1.2.0.1) 46

2.2.0.3: Plot of confidence for tuning frequency instruction vs. actual resultant THz output tuning that is performed by the Firefly OPO system.. 47

2.2.0.4: Error bars for tuning frequency instruction. The periodic nature of the error suggests that the OPO has quantized tuneable values for the frequencies. The discrepancies in tuning instruction vs actual tuning may be due to rounding errors. 48

2.2.0.5: Golay cell detected THz power as a function of angle from the output window. The points on the plot represent the measured Golay cell voltage signal converted to power using 21 KW/V responsivity specified for 50 Hz repetition rate signals. The data points are fit to a Lorentz lineshape represented by the solid line. 50

2.2.0.6: Scheme for determining THz emission angle and beam divergence from Firefly OPO 51

2.2.0.7: Plot of THz power as the detector is moved away from the Firefly THz output window. The noise floor is at 5.7 nW so at 50 cm distance, the signal becomes barely resolvable. Power was determined using Golay cell responsivity value of 21 KV/W. 52

2.3.1.1: Schematic of a Michelson interferometer set-up. A coherent light source emits a beam that is split into two by a beamsplitter (BS). The reflected beam is directed toward a movable mirror while the transmitted beam is directed toward a fixed mirror. Both beams meet at the detector and undergo constructive or destructive interference depending on the mirror translation, d, from the position of equal beam path length. 55

2.3.2.1: Lamellar mirror interferometer schematic drawing. The right most portion shows the motor configuration. The translation stage allows the plates of the interdigitated mirrors to slide past each other as the motor turns. For a photograph of the lamellar split mirror, see Appendix A.................... 59

2.3.2.2: The upper image is a visualization of the phase delay concept for the lamellar mirror. The lower image is an optical set up for the interferometric experiments. θ is the nine degree angle used as the correction factor in equations 2.3.2.1a and 2.3.2.1b. 60

2.3.4.1: Interferogram generated using the lamellar mirror interferometer scanning 10mm of phase displacement at step interval resolution of 5um (2.5um motor stepping). The Firefly OPO was tuned to at 0.9 THz continuous wave frequency. 65

2.3.4.2: Close up of interferogram at 0.9 THz frequency tuning. Noise effects are evident at the peaks and troughs. Wavelength of the THz frequency beam can be estimated by calculating the distance between two peaks and dividing by the number of peaks in between. In this plot, the wavelength is approximately 0.3305 mm (0.907 THz). 66

2.3.4.3: Fast Fourier transform (FFT) of interferogram generated by MATLAB software. The Bandwidth was found to be 48 ± 3 GHz. 67

2.3.4.4: Fast Fourier transform (FFT) of an interferogram made for the 1.8 THz firefly tuning. The interferogram was generated using half step phase intervals of 2.5 µm (1.25 µm motor stepping) It is evident that this tuning frequency yields a much less distinguishable FFT frequency profile. The periodic peaks are artefacts from the noise combined with the effects of apodization and zero-padding in the FFT. 68

2.3.4.5: Multiple frequency FFT transforms superimposed on one plot. The Dotted line draped over the FFT transforms indicates a more reliable frequency profile for the Firefly THz OPO system when used with the Golay detection scheme. Although Figure 2.2.0.1 indicates that the Firefly emits THz radiation as high as 2.5 THz, this result shows that the Golay may not be able to detect these high frequencies after it is attenuated by atmospheric moisture and reflection. 69

2.3.5.1: Screenshot of the MATLAB graphical user interface designed to control the interferometer stepper motor and acquire the interferogram. 71

3.2.0.1: Optical path set-up for THz transmission spectroscopy 77

3.3.0.1: Summary of transmission spectroscopy on explosives. The substances included in order of appearance from the top of the plot are: cyclotrimethylene-trinitramine (RDX), Composition 4 (C-4), pentaerythritol tetranitrate (PETN), cyclotetramethylene-tetranitramine (HMX), and icing sugar. 83

3.3.0.2: Comparison of cyclotrimethylene-trinitramine (RDX) spectrum to the Composition-4 (C-4) spectrum. RDX spectral peaks are 0.83, 1.04, 1.51 THz indicated by the vertical dotted lines. C-4 spectral peaks are 0.85, 1.02 and 1.38 THz indicated by the vertical solid lines. 86

3.4.0.1: Cyclotrimethylene-trinitramine (RDX) THz absorption spectrum. Notations (a), (b) and (c) represent the segmentation of the plot for Lorentz function analysis shown in Figure 3.4.0.2. Local maxima are annotated at the spectral peaks. 90

3.4.0.2: Isolated regions of the cyclotrimethylene-trinitramine (RDX) spectrum with Lorentzian fit analysis. Dots represent the spectrum data points. The solid line represents the Lorentz lineshape function fit. (a) is the 0.7 – 1.0 THz region (b) is the 1.0 – 1.2 THz region, (c) is the 1.2 – 1.9 THz region as indicated in Figure 3.4.0.1. The plots are annotated with the computed Lorentz fit peaks and their respective full width half maximum (FWHM) values... 91

3.4.0.3: Plot of Lorentzian fit algorithm performed on the Composition 4 (C-4) absorption spectrum. Grey dashed lines represent individual Lorentz lineshape functions with their central peaks annotated on the plot. The red dashed line represents the superimposed resultant fit. The solid line is the original spectrum. The spectral peaks as computed by the Origin are: 0.85, 1.02, 1.38 THz. (see Table 3.4.0.2) 93

3.4.0.4: Absorption curves of (a) cyclotetramethylene-tetranitramine (HMX) compared to (b) icing sugar and (c) pentaerythritol tetranitrate (PETN) with superimposed Lorentz fit functions. The peaks for HMX and icing sugar are similar when found by the Lorentz lineshape function as 1.43 and 1.44 THz respectively. However, the linewidth of HMX is 0.83THz while icing sugar has a 0.67 THz linewidth as determined by FWHM of the Lorentz function. PETN (c) exhibits a 1.78 THz spectral peak and 0.80 THz FWHM linewidth. 94

3.5.1.1: Threshold of detection for RDX samples. The plot shows the absorption spectrums of RDX samples of various thicknesses. If a sample is made too thick (1.81mm), the absorption spectrum resembles that of the Firefly OPO output spectrum since all the radiation is absorbed by the sample. If the sample is too thin (0.15mm), all the THz passes directly to the Golay cell and the absorption coefficient becomes approximately unity. 97

3.5.1.2: Spectra of explosives samples sandwiched between polystyrene plates. The thicknesses of the samples were selected to be within the criteria of validity. 99

3.6.0.1: Concealed cyclotrimethylene-trinitramine (RDX) spectroscopy. The various dielectric obstructions are compared to the unobstructed RDX spectrum. The rayon fabric spectrum is offset by two arbitrary units and the paper envelope spectrum is offset by four for clarity.......................... 102

3.7.0.1: On the left is a photograph of the “A” shaped out of tinfoil to be imaged with THz frequencies. On the right is the raster scan THz image of an “A” shaped tinfoil concealed by a 2 cm thick slab of Styrofoam. The width of the “A” is approximately 2.5 cm. The scan resolution was in 1 mm step intervals. 104

3.7.0.2: A photograph of a paperclip used for THz frequency imaging is shown on the left. On the right is the THz transmission image taken of the paperclip within a paper envelope. The clip was reshaped to a width of 15 mm in order to fit into the span of the translation stage. The angular appearance of the THz image may be attributed to the 1 mm resolution of the raster scan. Square pixels were smoothed through image processing. 105

3.7.0.3: Images of a triangle of cyclotrimethylene-trinitramine (RDX) explosive concealed within an envelope. Three images are shown using Firfely tuning frequencies of 0.77, 0.83 and 0.90 THz. The highest ratio of absorption in the explosive sample region occurs when transmitting the 0.83 THz frequency. 106

3.7.0.4: Profile of absorption for cyclotrimethylene-trinitramine (RDX) images at each frequency. This plot is a vertical slice of absorption for the y = 4 mm line in previous figure (Figure 3.7.0.3). The 0.83 THz absorption effect is the most significant as would be expected by the spectroscopy experiments performed in section 3.3. The x-direction coordinate is arbitrary but the scale is correct. 107

3.8.0.1: Illustration of the THz-TDS scheme. The Ti:Sapphire laser emits a femtosecond pulse that is split into a pump beam and probe beam by a 90(R)/10(T) beamsplitter (BS). The pump beam propagates through a variable delay line that controls the relative temporal delay between pump and probe pulses. Then the pump beam irradiates a photoconductive (PC) switch which generates the THz pulse that is focused on to the sample by two 2" diameter off-axis parabolic mirrors. Two more parabolic mirrors focus the transmitted THz pulse to an electro-optic (EO) crystal where it meets with the probe beam and modifies its polarization. The orthogonal polarizations of the probe beam are extracted by a quarter wave plate ($\lambda/4$) and a Wollaston prism (WP). The two emergent beams are detected by a balanced photodiode. 111

3.8.0.2: THz-TDS empty cell pulse. (a) The time domain pulse is approximately one picosecond in duration. (b) The power spectrum of the THz TDS pulse displays a bandwidth of approximately 0.7 THz.. 112

3.8.0.3: Absorption spectrum of water vapour in the THz frequency regime. The plot is formed by taking the Fourier transform of a THz pulse traveling through atmospheric water vapour conditions referenced against a pulse traveling in a chamber purged with dry nitrogen. The absorption lines are listed in the inset.. 113

3.8.1.1: Comparison of THz pulse travelling through empty sample cell and travelling through RDX explosive sample. Note that the RDX transmission experiences a decrease in amplitude and an increase in pulse length due to absorption. 115

3.8.1.2: Comparison of terahertz time domain spectroscopy (THz-TDS) to the continuous wave (CW) Spectroscopy of RDX performed using the Firefly THz in the previous section. The TDS spectrum was lower in amplitude so the spectrum was multiplied by three for the comparison. THz-TDS was only able to discern the first 0.8 THz region peak of the RDX spectrum since the lower bandwidth prevented access to the higher frequencies. 117

4.4.0.1: (a) indicates the basic schematic of the integrating amplifier IVC102 integrating amplifier. (b) shows the time-gated integration scheme. The charge is trapped within the capacitors of the amplifier and an analog to digital converter reads the voltage in a time gated scheme. Figure adapted from IVC102 microchip Manual 125

4.4.0.2: The first proposed design for the THz frequency camera circuit utilizing a PIC16 microcontroller to control an eight by six LED array connected by common rows and common columns in a crosshatched configuration. 129

4.4.0.3: Illustration of the oscilloscope reading that is probing the integrating amplification action for the crosshatched multiplexing design. The triangles represent the voltage accumulated by the integrating amplifier over time until the next element is accessed. Element 5 is being illuminated by light, however, element 2 is also experiencing a signal due to crosstalk effects on common column lines. However, the crosstalk effect only causes the element to build a signal up to a finite threshold. If this is set as the cutoff threshold, the crosstalk effects can be bypassed. 130

4.4.0.4: A second proposed design for the THz frequency camera circuit. An Arduino Duemilanove microcontroller was used to control a 2×3 array with independent leads running from the anode and a common wire from the cathodes. 132

A1: View of the lamellar split mirror interferometer.................................. 155

A2: Rear view of lamellar split mirror interferometer................................ 156

A3: Frontal view of lamellar split mirror interferometer............................ 157

F1: Photograph of first circuit design utilizing the PIC16 microcontroller 190

F2: Photograph of second circuit design utilizing the Arduino demiolove microcontroller board seen on the left. The

individual LEDs at the bottom of the photo are in use for
this design. 191

LIST OF SYMBOLS AND ABBREVIATIONS

Fundamental Constants

$c = 2.99792458\times10^{8}\ \mathrm{m/s^{2}}$	speed of light in vacuum
$h = 6.626\times10^{-34}\ \mathrm{Js}$	Planck's Constant

Symbols

ε	molar absorptivity (extinction coefficient)
λ	wavelength
$\widetilde{\upsilon}$	wavenumber
v	frequency
V	potential energy
T	kinetic energy
ψ	wavefunction
H	Hamiltonian operator
E	energy
ω	angular velocity
v_{rot}	rotational frequency
m	mass
I	moment of inertia
μ	reduced mass
$F(J)$	rotational "term"

$G(n)$	vibrational "term"
B	rotational constant
α_e	vibrational-rotational coupling constant
α	absorption coefficient
I	intensity
ρ	concentration
A	absorbance
L	beam path-length difference
d	mirror displacement

Abbreviations

2D	two dimensional
3D	three dimensional
a.u.	arbitrary units
arb. units	arbitrary units
BS	beam splitter
CW	continuous wave
C-4	composition 4
EO	electro-optic
FWHM	full-width at half-maximum
FFT	fast Fourier transform
HMX	High Melting eXplosive (cyclotetramethylene-tetranitramine)

IR	infrared
OPO	optical parametric oscillator
PC	photoconductive
PETN	pentaerythritol-tetranitrate
RDX	Research Department Explosive (cyclotrimethylene-trinitramine)
THz	terahertz
THz-TDS	terahertz time-domain spectroscopy
TPO	terahertz parametric oscillator
WP	Wollaston prism

Chapter 1

Introduction

1.1 Motivation

Security and safety is an ever-present public concern having critical consequences on society and economy. Government buildings, airport checkpoints, ground transit centers and public spaces are constantly under threat of attack. Standardized measures and practices have been established to deter illegal behaviour through the use of security camera surveillance, metal detector checkpoints and x-ray scanning, however, these have proven at times to be ineffective and inefficient. High security checkpoints must follow a fragmented approach which requires multiple steps and screenings, utilizing many expensive detectors, each screening for a different type of threat. Ultimately, these systems rely on the judgement of a specialist security officer who is present at all times to perform a visual inspection or an invasive search through luggage or packages deemed as a potential threat by an automated screening.

A major impetus for the fragmented security screening approach is that each individual detection system used currently has associated drawbacks and limitations. Metal detectors indiscriminately detect the presence of metallic objects, yielding no information on whether the object poses an actual threat. For example, metal from a gun is indistinguishable from metal found in belt buckles.

Furthermore, metal detectors are incapable of detecting non-metallic weapons and threats such as ceramic guns and explosives. On the other hand, X-ray imaging systems are capable of producing contrast images of the concealed weapons. However, repeated exposure to full body X-ray imaging may result in adverse health effects due to the high energy ionizing nature of x-ray radiation. Although studies conducted on the health effects of full-body radiation screenings have stated that modern X-ray backscattering systems apply very low doses of radiation that is comparable to the ambient radiation levels experienced during an airplane flight [1, 2], it has been argued that even small doses of high ionizing radiation may be carcinogenic [3]. Furthermore, x-ray images still rely on a security officer to perform a proper image inspection and assessment to classify the threat. Airport security organizations have also considered more complex X-ray systems for purposes of explosives detection. The Smiths Detection EDtS (Explosive Detection tomography System) [4] uses X-rays to compute the effective atomic number (Z_{eff}) of explosives based on their effective nuclear charge. However, the Z_{eff} of some explosives is very similar to that of common non-threatening materials. Hence, the EDtS must also compute the density of materials in order to make the distinction between materials with similar Z_{eff} values such SEMTEX explosives and chocolate.

Both handheld, and walk-through Ion Mobility Spectrometry (IMS) systems have been employed to detect trace amounts of explosives at security checkpoints. This detection scheme has high sensitivity and selectivity for explosives, but has a slow response, often showing results several minutes after the scan. The large scale systems require the subject to enter a testing chamber and wait while sampling air pulses dislodge particles from the subjects clothing and body for analysis. In order to detect concealed weapon threats IMS must also be used in conjunction with imaging systems. Such multi-tiered security approaches become unattractive when faced with the expense of manning specialized personnel to each individual phase of the security screening [5]. There will be an inevitable drive in security screening technology toward a singular comprehensive approach that is both affordable and reliable.

Terahertz (THz) radiation technology presents promising solutions to many of these challenges facing modern security and surveillance systems. THz frequencies, typically recognized as the 0.3 to 10 THz frequency region (wavelengths of 1mm to 30μm), have access to electromagnetic properties of matter unavailable to other spectral regions. While extended periods of exposure to ionizing radiation such as x-rays can cause DNA damage in living cells, there are no adverse health effects due to THz radiation exposure since a THz photon energy is low and non-ionizing (1 THz = 4 meV) [6, 7]. THz can penetrate most dielectric materials such as plastics, clothing and cardboard. However, metallic objects strongly reflect THz so if a metallic object was concealed beneath an article of clothing, it would be visible with high contrast in a THz image.

While the adjacent wavelength regimes have been studied for many years, until recently, the THz regime has been largely ignored due to the notorious difficulty involved in generating and detecting this particular radiation frequency. Hence, it has been appropriately referred to as the “terahertz gap”. Terahertz frequencies emitted as part of black body radiation have a low spectral radiance. The Sun’s THz spectral radiance is calculated to be merely 1.77 $W/m^2/sr/THz$. Hence, astronomical studies of terahertz emitted from celestial bodies like the sun or from distant galaxies must be conducted at high altitudes in order to keep atmospheric attenuation to a minimum. Using ambient THz emitted from the sun is clearly impractical for security screening applications. Powerful and coherent sources are required to present THz radiation as a viable for security system.

On the other hand, the adjacent regions of the electromagnetic spectrum can be investigated with less difficulty. Microwave and radio waves exist below THz frequencies (<0.1 THz), which can be generated by vacuum tube devices that operate on ballistic motions of electrons such as Magnetrons [8], klystrons [9], traveling-wave tubes (TWT) [10] and gyrotrons [11] or by semiconductor devices such as Schottky diodes and IMPATT (IMPact ionization Avalanch Transit-Time) diodes [12]. Infrared and visible waves exist above THz frequencies (> 10 THz) and may be produced by laser systems, whereby quantum transitions within a gain medium trigger the release of photons. Titanium doped Sapphire solid state lasers [13] are widely tuneable in this frequency regime and are useful for infrared spectroscopy.

Recent technological advancements have finally presented suitable sources and detectors for the THz frequency regime. Optical parametric oscillators (OPO) [14], optically pumped THz lasers (OPTL) [15], backward-wave oscillators (BWO) [16], photomixers [17], and quantum cascade lasers (QCL) [18] are now capable of generating THz radiation. CW detection of terahertz radiation can be accomplished with the use of Golay cells [19] and photoacoustic bolometers [20]. Short pulsed THz can be detected by electro-optic (EO) crystals [21, 22], and by photo-conductive-gated antenna (PCGA) [23]. With these technologies, THz radiation has become a more attractive and affordable research pursuit. The following section gives insight on how these THz frequency technologies can be utilized and provides an assessment of the viability of THz radiation for security purposes through a literature review of recent research conducted.

1.2 Background and Research Progress

Concurrent with the advent of THz generation and detection technologies, research into THz for security applications has grown significantly. Michael Kemp, as Senior Vice President at terahertz TeraView Ltd., Cambridge, was responsible for the company's activities in security screening and non-destructive THz testing. He has demonstrated the viability and potential of THz for security imaging and spectroscopy in several studies [24-26]. In his 2003 paper "Security applications of terahertz technology" [24], Kemp described and tested the "TeraView" Terahertz Pulsed Imaging (TPI) system in its capability to perform both time-domain (TD) imaging [27] and Terahertz time domain spectroscopy (THz-TDS) [28] through a series of comprehensive proof-of-principle experiments. Reflection imaging was shown to be possible through fabric layers such as wool, and cotton. Imaging was performed by a raster scanning technique using a single electro-optic (EO) detector to observe small metallic objects like the tip of a scalpel and a microchip. Spatial resolution of imaging was found to be diffraction limited (350 um). Depth imaging capability was also demonstrated as pages within an envelope could be individually resolved. Text on the pages could even be read if the lettering print type was large. The depth resolution was found to be 20-40 um depending on the refractive index.

Despite THz technology having proven its vast applications in laboratory setting, it has experienced a reluctant reception commercially and has yet to experience wide-spread utilization. On the other hand, an adjacent sub-terahertz band of frequencies, “millimeter waves” also known as the microwave regime (30-300GHz) has already been implemented in some airport security screening systems. Appleby and Anderton [29] made a comparison of millimetre-waves (MMW) to submillimeter-waves (SMMW) -- referred to here as terahertz frequencies -- and concluded that atmospheric absorption severely limits the capability of SMMW (THz) systems to perform stand-off detection at long range. MMW on the other hand, are not limited as such and would even be effective for poor weather navigation. Dielectrics and clothing materials are transparent to both SMMW (THz) and MMW, but unlike in the SMMW (THz) regime, there is no spectral information available for material identification in the MMW regime. SMMW (THz) was described to be potentially ideal for applications such as security screenings which benefit from the combined capability of THz spectroscopic detection of hidden explosives and clothing/packaging transparent imaging. However, Kemp explained in his short review [26] that before THz systems can be produced for widespread commercial use, further development must be made in THz system architectures as well as in both THz source and detector technology.

Contrary to this notion, a publication by Baker et al. [30], demonstrated that the TeraView with the hand-held wand attachment was capable of explosives detection and imaging of concealed weapons beneath several layers of clothing in a scheme similar to a handheld metal detector scan. In the same paper, a prototype pulsed THz system for stand-off detection was demonstrated to be capable of explosive detection at distances of 1m, behind layers of clothing, and under atmospheric absorption conditions. Baker concluded that over time, with some optimizations to the sensitivity of the system, the TeraView could be a powerful alternative to conventional security screening technology.

Of particular interest to this thesis are studies involving the application of THz in the continuous wave (CW) mode for spectroscopy and imaging. Specifically, this thesis focuses on the optical parametric oscillation (OPO) methods for generating THz [31, 32]. Several studies have already investigated some security screening applications utilizing CW terahertz radiation. Kawase [33] presented a method for screening drugs and explosives in mail using the tuneable terahertz wave parametric oscillator (TPO) source. Although similar to the OPO systems, the TPO developed by Kawase in the 1990s included a number of improvements upon the basic OPO system in terms of compactness, wavelength selectivity and output power [34]. An alternative candidate for CW THz generation is the mechanism of photomixing [35] first described by Brown et al. Using this approach, M.R. Hofmann [36] presented a cost-effective, and versatile CW photomixer based THz spectrometer to screen mail for illicit drugs and explosives.

CW THz has received considerably less attention than THz-TDS approaches because THz-TDS is capable of acquiring depth information within a sample. This can be achieved by observing the pulse travel time, electric field, and phase. THz-TDS also has an advantage that it can collect broad spectral information (0.1-3 THz) in a single picosecond pulse duration. However, the advantage of CW systems is that each distinct narrowband THz frequency tuning has higher power when compared to the TDS system, which must distribute power across a broad band. Furthermore, a narrow band CW signal tuned across the frequency range is instrumentally easier to measure at high resolution since there is no need for long scanning delay lines which are a necessity for time domain schemes.

In order for terahertz spectroscopy to achieve status as a reliable method for explosives detection, it is necessary to develop a comprehensive database of common explosives for use as a reference in security screenings. Several groups have contributed to such a movement by performing spectroscopy on the most common varieties of high explosives and collecting results of other research groups [37-41]. However, the characteristic spectral signature of an explosive found by one group is sometimes conflicting with the results of another. For example, the explosive spectroscopy work done by Tribe [37] using the TeraView system yielded spectral signatures differing from the results obtained by Liu [39]. Both studies employed a similar terahertz time domain spectroscopy (THz-TDS) scheme, yet, as seen in Figure 1.2.0.1, they arrived at dissimilar results. Tribe observed cyclotrimethylene-trinitramine (RDX) to exhibit THz spectral absorption peaks at 0.72, 1.26, and 1.73 THz, while Liu observed peaks at 0.82, 1.5, and 1.96 THz in the same region. Similar inconsistencies were evident for pentaerythritol tetranitrate (PETN), cyclotetramethylene-tetranitramine (HMX) and trinitrotoluene (TNT). PETN scanned by Tribe exhibited a 1.73 THz peak while Liu observed a 2.0 THz peak. HMX tested in Tribe's laboratory showed absorbance peaks at 1.58, 2.21, and 2.91 THz. Liu observed HMX absorption peaks of a similar shape, but they were shifted in frequency to 1.78, 2.51 and 2.82 THz. TNT spectral peaks 1.44 and 1.91 seen by Tribe were seen as 1.66 and 2.2 THz by Liu. Table 1.2.0.1 shows a more comprehensive summary of spectral results observed by Liu using a combined THz spectroscopy and FTIR spectroscopy approach. The inconsistencies between papers suggest that there may be some variations in the composition of explosives depending on the manufacturer. Variations in moisture content and sizes of powdered grains may affect the spectrums.

In an attempt to improve the resolution of explosives spectroscopy, Malinger et al. [42], performed THz guided-wave spectroscopy on RDX/aluminum and RDX/gold thin films. Much sharper THz spectral peaks were observed, however, cryogenic cooling was employed to minimize the broadening effects. This approach is not practical for security applications; however, the research may be utilized to augment the current databases and aid in understanding the nature of the THz frequency molecular motions. Clearly, there is need for more experimentation in order to establish a confidence in THz frequency technology as a potential scheme for explosives detection at security checkpoints.

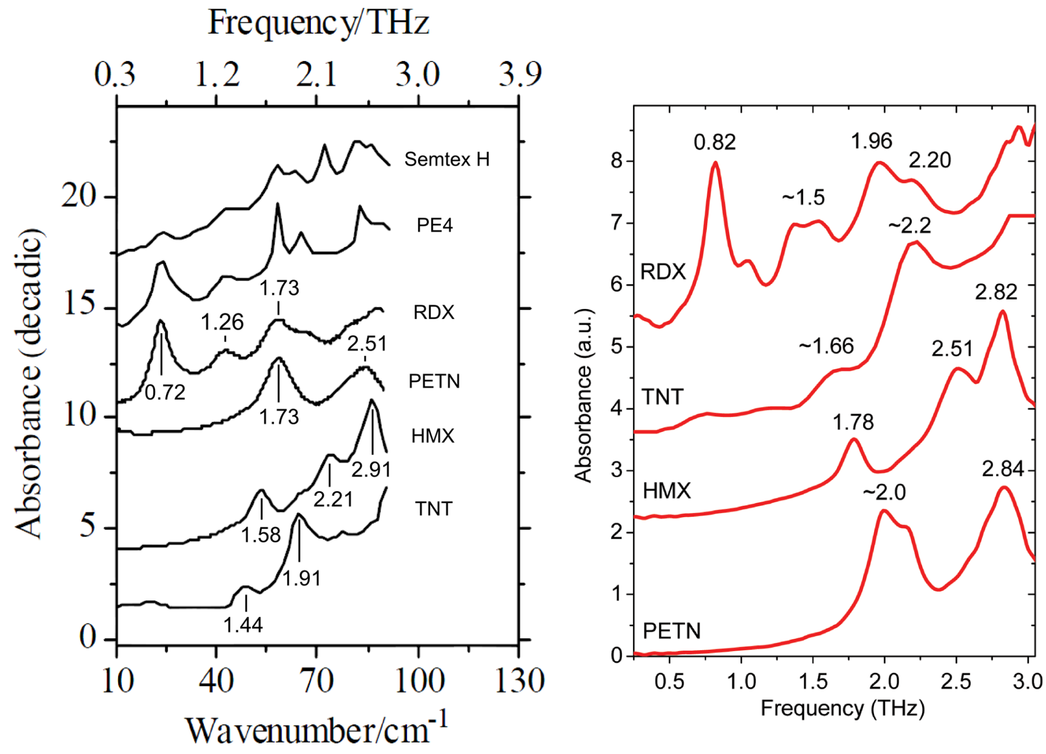

(a) (b)

Figure 1.2.0.1: The plot on the left (a) shows the results of THz spectroscopy performed on explosives by Tribe [37]. The plot on the right (b) are the results collected by Liu et al. [39]. The (a) peaks have been annotated with the publication's tabulated peak values for clarity. Note that the studies used similar methods of TDS spectroscopy but yielded differing results.

Explosive Compound	Measured Absorption Peak Position (THz)
TNT	1.66, 2.20, 3.69, 4.71, 5.52, 8.28, 9.12, 9.78, 10.65
RDX	0.82, 1.05, 1.50, 1.96, 2.20, 3.08, 6.73, 10.35, 11.34
HMX	1.78, 2.51, 2.82, 5.31, 6.06, 11.28, 12.54, 12.96
PETN	2.0, 2.84
Tetryl	5.97, 10.11, 11.28, 14.67, 16.14, 18.36
2-amino-4, 6-DNT	0.96, 1.43, 1.87, 3.96, 5.07, 6.27, 8.49, 9.87, 10.77
4-amino-2, 6-DNT	0.52, 1.24, 2.64, 3.96, 5.04, 5.82, 7.53, 9.30, 10.20
4-Nitrotoluene	1.20, 1.37, 1.86, 6.75, 8.85, 10.83, 14.04, 15.66
1,3,5-TNB	4.17, 4.62, 10.05, 11.19, 13.80, 15.75, 19.05
1,3-DNB	0.94, 1.19, 2.37, 10.56, 12.18, 15.33, 17.13
1,4-DNB	3.24, 3.96, 5.55, 10.38, 12.45, 13.29, 15.21, 15.54
2,4-DNT	0.45, 0.66, 1.08, 2.52, 4.98, 8.88, 10.56, 11.58, 12.81
2,6-DNT	1.10, 1.35, 1.56, 2.50, 5.61, 6.75, 9.78, 11.43, 13.32
3,5-dinitro aniline	0.96, 1.20, 3.18, 4.62, 5.04, 5.91, 7.44, 10.62, 10.98
2-nitro diphenyl anine	2.19, 2.58, 2.88, 3.45, 5.13, 6.18, 7.56, 10.08, 12.33

Table 1.2.0.1: Summary of the combined findings of Liu et al.[39] attained through THz spectroscopy and Fourier Transform Infrared (FTIR) spectrometer (Bruker IFS 55 V/S) across the frequency range 0.1 – 21 THz.

Due to the complex nature of molecular interactions in the THz frequency regime, simple computational models are insufficient to predict the spectra. The standard method for predicting signatures in the infrared region was by density function theory (DFT) computation [43, 44]. It is essentially a quantum mechanical model for studying the ground state electrical structure of a many-atom system. However, the basic model has proven less successful when computing the molecular motions in the THz frequency regime. Groups have used programs like GAUSSIAN [45] and GAMESS [46] or similar modeling programs to perform gas-phase DFT computations for explosives molecules to determine the theoretical THz spectra. However, gas-phase models of terahertz spectral signatures assumed isolated-molecule calculations and are incapable of accurately predicting the collective molecular vibrations featured in experimental results. Allis et al. [47-50] demonstrated that solid-state molecular modeling is necessary to predict the nature of collective molecular motions that give rise to the broad spectrums seen in the lower THz regime. Simulations of pentaerythritol tetranitrate (PETN) and cyclotetramethylene-tetranitramine (HMX) [49] were found significantly simpler than that of cyclotrimethylene-trinitramine (RDX), since PETN and HMX can be modeled with two molecules in a unit cell whereas the unit cell for RDX must contain eight molecules. The most promising computational results by Allis et al. [51], were obtained for polycrystalline RDX using DMol^3 software [52]. These results were compared with both room temperature (298K) and cryogenically cooled (7K) experimental spectra. The simulation involved first calculating and optimizing the bond lengths between atoms, then determining the subsequent changes to the intermolecular hydrogen-bonding that results when the RDX molecules are set in close proximity (i.e. solid phase). The normal modes of vibrations were calculated and are shown in Figure 1.2.0.2. The computation shows some inconsistency with empirical results. Specifically, all the calculated molecular motions occur above 1 THz while many of the experimental studies indicate a strong 0.8 THz absorption in RDX. A plot shown in Figure 1.2.0.3 compares the experimental THz spectroscopy results at room temperature and 7K superimposed with the computed data using the solid state DFT model. It can be seen in the plot that the 298K room temperature spectrum differs significantly from the simulation while the low temperature 7K spectra approaches the features predicted by DFT. The 0.8 THz peak appears to shift to higher THz frequencies as the temperature is decreased. This effect was experimentally confirmed for PETN by Fan et al.[53]. While the DFT calculations provide reasonable basis for low temperature spectral predictions, the algorithm must be optimized in order to make correlation with spectral features caused by collective molecular vibrations that occur at higher temperatures.

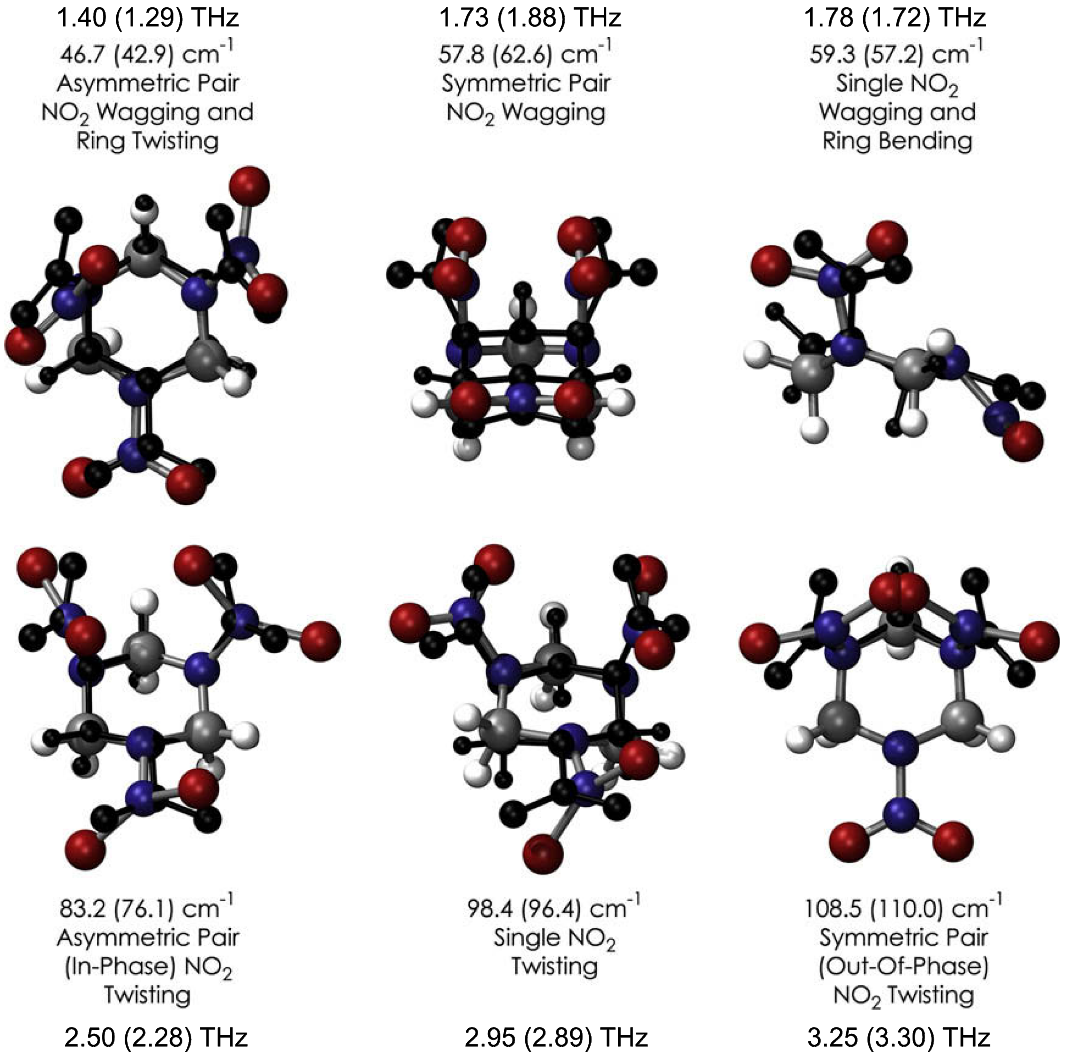

Figure 1.2.0.2: Illustration of six lowest energy normal modes of vibrations for an RDX molecule derived from solid-state computational simulation of THz spectra. The simulated results show THz frequency spectral peaks that are shifted to higher frequencies in comparison to the empirically observed spectra. From Allis et al. [51]

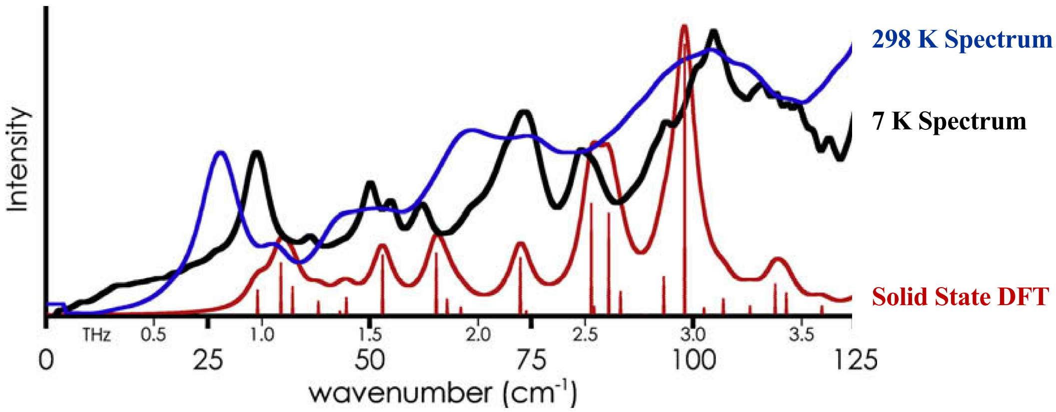

Figure 1.2.0.3: Simulated solid-state DFT spectrum of RDX shown with superimposed 298K and 7K experimental RDX spectra.

1.3 Theoretical Framework

The following sections are intended to provide a general understanding of spectroscopy and relevant physical phenomena. It is, by no means, a comprehensive review of the subject. Readers are advised to refer to textbooks in order to satisfy a deeper curiosity [54-57]. Mittleman [58] is a suitable starting text since it describes the significance of terahertz radiation and addresses the state-of-the-art today with reviews on the various applications and methods for generating THz frequencies. Unfortunately, a strong theoretical understanding of the molecular motions specific to the THz regime is lacking [59]. However, the fundamental molecular interactions observed in infrared (IR) and microwave spectroscopy conceptually extend to the THz spectroscopy regime. Therefore, the abundance of textbooks addressing the IR regime are useful for comprehending the studies of this thesis. Griffiths [60] provides a concise introduction to IR spectroscopy and the modern analytical methods. Gunzler [61] provides emphasis on practical guidance and methods for IR spectra analysis and optimization.

1.3.1 Molecular Model

Molecular structures and motions cannot be simply defined since they are best calculated through models of applied quantum mechanics. However, classical mechanics can facilitate a basic understanding of the spectroscopic relationships. While the wave mechanics (Schrödinger) scheme is far more powerful for computation and evokes deeper comprehension, the simpler classical Bohr atomic model is illustrative of basic atomic structure and is sufficient for the purposes of this thesis.

Atoms have associated energy levels defined by the nature of electron orbits of around the nucleus. These orbits are quantized such that only specific energies are permitted. Energy can be transferred to an atom by various ways, (e.g. collisions with atoms) but most often by interaction with radiation.

$$E_1 - E_2 = hv = h\frac{c}{\lambda} = hc\widetilde{\upsilon} \qquad (1.3.1.1)$$

E_1 and E_2 correspond to the energy level in orbit 1 and 2, $h = 6.626 \times 10^{-34}$ Js is Planck's constant, v is the frequency, λ is the wavelength, $\widetilde{\upsilon}$ is the wavenumber and c is the speed of an electromagnetic wave in freespace (speed of light). The value, hv, is the radiant energy measured in Joules. The relationship of proportionality between radiation energy and frequency means that only specific frequencies of electromagnetic radiation can undergo an energy transfer interaction with an atom that results in an orbital transition.

The wave mechanics model replaces electron orbitals in the Bohr model with wave functions that satisfy the Schrödinger equation. This model is required to predict more complex electron state interactions. The reader is directed to more comprehensive texts on quantum mechanics [62, 63] to understand the mechanisms of selection rules and transition probabilities between energy states.

1.3.2 Molecular Vibrations

Atoms are joined in relative proximity as molecules by the interactions between electrons of the outermost orbits and the atomic nuclei. The balance of forces result in vibrational and rotational energy states. Through the uptake of energy, atoms can be excited into motion about their equilibrium displacement positions. A diatomic molecule can be modeled as a simple harmonic oscillator and compared to a vibrating mass (m) on a spring with an elastic force constant k . Using this model, the resultant motion is sinusoidal with the total energy dependant on the maximum displacement. Throughout the vibration process, energy is transferred between potential energy ($V = 1/2k\Delta r^2$) and kinetic energy ($T = 1/2m(dr/dt)^2$). Where Δr represents the displacement from the equilibrium and dr/dt represents the instantaneous rate of displacement change (velocity). The sum of potential and kinetic energy remains constant.

Due to the consequences of these vibrational interactions occurring on a small scale, classical mechanics is insufficient for describing molecular motions.

In order to accurately model the motions of molecule, it is necessary to apply some concepts from quantum mechanics. Mechanical parameters called "operators" act on the state function of the molecular system in question. The Hamiltonian operator $H = T + V$ corresponds to the total energy, which is the value of interest for spectroscopy. Time-independent energy states of the system yield a solution to the eigenvalue equation of this operator: $H\psi = E\psi$. This is called the Schrodinger equation in which ψ represents the eigenfunction and E represents the corresponding energy value of the system. For the case of a one-dimensional single particle system, the Schrödinger equation becomes:

$$-\frac{\hbar}{2m}\frac{d^2\psi}{dx^2} + V(x)\psi = E\psi \qquad (1.3.2.1)$$

Where $\hbar = h/2\pi$ is the Planck's constant. The consequence of this treatment is that the energy for vibrational modes is quantized.

$$E_n = hv(n + 1/2) \qquad \text{where } n = 0,\ 1,\ 2\ \ldots \qquad (1.3.2.2)$$

n is the vibrational quantum number and v is the oscillator frequency seen in classical mechanics. Equation 1.3.2.2 indicates that vibrational energy is analogous to electron states in the sense that the energy is quantized. Figure 1.3.2.1 illustrates the discrete energy states for a harmonic oscillator.

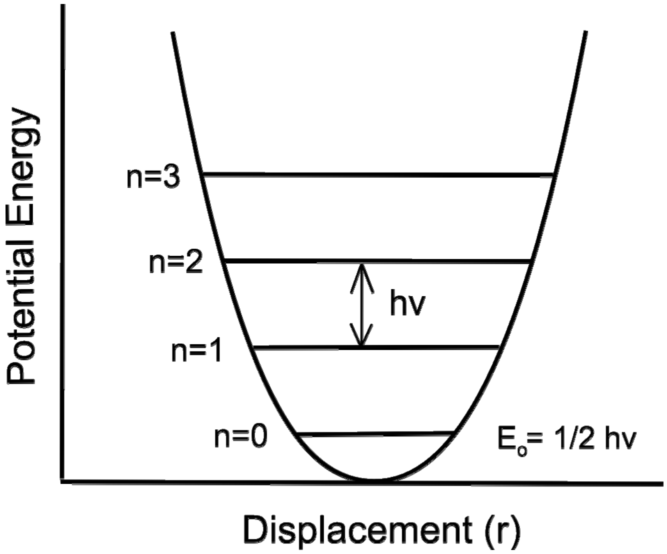

Figure 1.3.2.1: Potential energy with discrete energy states for linear harmonic oscillator

1.3.3 Molecular Rotation

Classical mechanics describes rotational energy E_r as:

$$E_r = 1/2I\omega^2 \tag{1.3.3.3}$$

Where $\omega = 2\pi v_{rot}$ is defined as the angular velocity, v_{rot} is the frequency of rotation and I is the moment of inertia. The moment of inertia for diatomic molecules of masses m_1 and m_2 is

$$I = m_1 r_1^2 + m_2 r_2^2 = \frac{m_1 m_2}{m_1 + m_2} r^2 = \mu r^2 \tag{1.3.3.4}$$

Where μ is the reduced mass, and r_1 and r_2 are the respective distances from the axis of rotation of masses m_1 and m_2.

The solution to the Schrödinger equation gives the discrete energy eigenvalues:

$$E_r = \frac{h^2}{8\pi^2 I} J(J+1) \qquad J = 0, 1, 2 \ldots \tag{1.3.3.5}$$

Where J is the rotational quantum number. Recall the energy-frequency condition must be fulfilled for vibration or rotational energy transfer from equation 1.3.1.1.

1.3.4 Rotational Vibrational Spectra

In reality, molecules rotate and vibrate simultaneously, so the effect of the two types of energy transfer must be combined. First rotations and vibrations are converted into common terms. Using the infrared spectroscopy convention, the wavenumber $\tilde{\upsilon}$ resulting from a state transition between energy E' and E'' is:

$$\tilde{\upsilon} = \frac{E'}{h \cdot c} - \frac{E''}{h \cdot c} \tag{1.3.4.1}$$

In the case of a rotational transition, the two values in the above equation are each defined as a “term” $F(J)$:

$$F(J) = \frac{E_r}{h \cdot c} = \frac{h}{8\pi^2 c \cdot I} J\left(J+1\right) = BJ\left(J+1\right) \tag{1.3.4.2}$$

Where B is defined as the rotational constant and E_r is the rotational energy. A rotational transition can then be described by the difference of two terms with rotational quantum numbers

$$F(J') - F(J'') = BJ'(J'+1) - BJ''(J''+1) \qquad (1.3.4.3)$$

Similarly for vibrations, using the "term" notations, we have the vibrational term $G(n)$:

$$G(n) = \frac{E_n}{h \cdot c} = \frac{v}{c}\left(n + \frac{1}{2}\right) \qquad (1.3.4.4)$$

Where E_n is the vibrational energy defined in equation (1.3.2.2). The selection rule for a harmonic oscillator is $\Delta n = \pm 1$ so vibrational transitions can only occur to the next nearest 'term'.

Empirically, molecules do not act like an ideal harmonic oscillator but as "anharmonic" oscillators. The attractive forces acting between atoms approaches zero with increasing distance until the atoms dissociate at the "dissociation energy" level. This is modeled as the Morse potential (Figure 1.3.2.2).

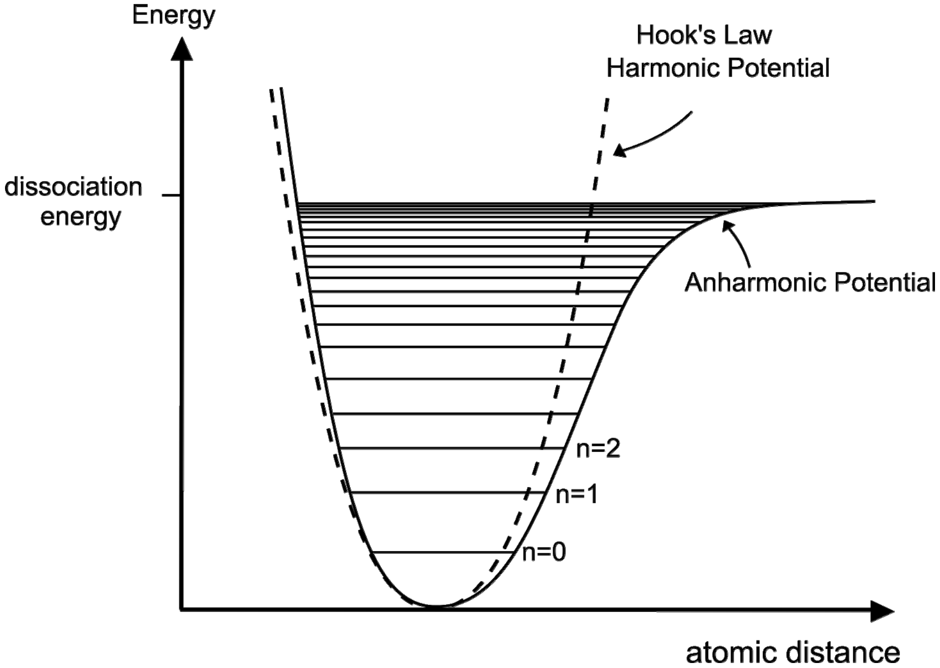

Figure: 1.3.4.1: Potential energy diagram for harmonic and anharmonic oscillator.

If observing the anharmonic model, oscillations are no longer sinusoidal. Also, the term differences, $G(n') - G(n'')$, decrease with increasing quantum number. However, the most important difference introduced by the anharmonic model is that transitions are no longer limited to adjacent terms. Transitions into higher terms are possible but with greatly decreasing probability. The selection rule becomes $\Delta n = \pm\, 1, 2, 3, \ldots$

An important effect when considering rotations and vibrations simultaneously is that vibrations increase the average interatomic distance between molecules and thus increase the moment of inertia. This augments the value of the, previously defined, rotational constant B. The actual rotational constant, B_n, becomes smaller than the equilibrium distance rotational constant B_e.

$$B_n = B_e - \alpha_e \left(n + \frac{1}{2} \right) \tag{1.3.4.5}$$

α_e in equation 1.3.3.9 is the vibrational-rotational coupling constant which is smaller than B_e. The difference between B_n and B_e increases with increasing quantum number. The combined “term” scheme for rotational-vibrational oscillator is shown in Figure1.3.4.2.

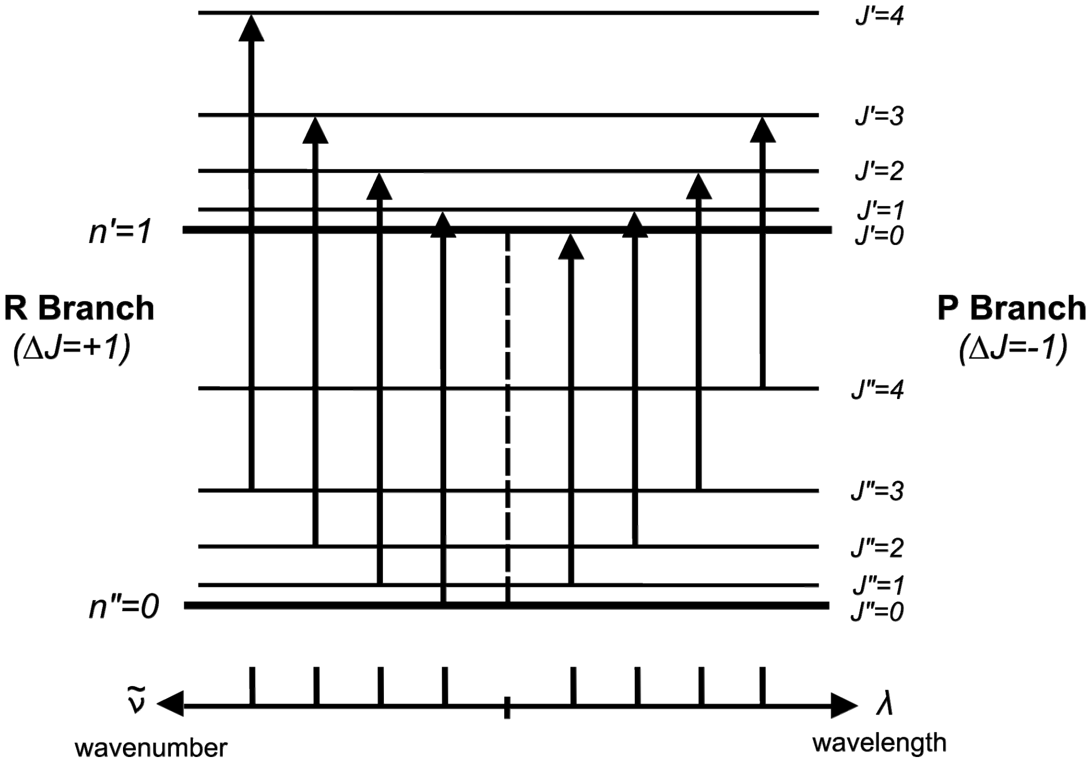

Figure 1.3.4.2: Term scheme of combined rotation and vibration oscillator for the transition $G(n=1, J \pm 1) \leftarrow G(n=0, J)$

The summarized selection rules for this rotating oscillator are as follows:

For a rotational transition:

$$\Delta J = \pm 1 \tag{1.3.4.6a}$$

$\Delta J = +1$ is an R-branch transition and $\Delta J = -1$ is a P-branch transition.

For the vibrational transitions:

$$\Delta n = \pm\ 0, 1, 2, 3\ldots \tag{1.3.4.6b}$$

However, note that for the special case of paramagnetic molecules: $\Delta J = \pm\, 0,\, 1$

The absorption spectrum is defined as the sum of the term differences of the vibrational and rotational transitions.

$$\tilde{\upsilon} = \underbrace{G(n') - G(n'')}_{Vibrational} + \underbrace{B_n' J'(J'-1) - B_n'' J''(J''+1)}_{Rotational} \tag{1.3.4.7}$$

The B_n' and B_n'' are the rotational constants that are modulated by the atomic vibration in the respective vibrational energy level.

1.3.5 Normal Modes of Vibration

The equations in the previous section were applicable to diatomic molecules, which can perform only a single vibrational motion. Multi-atomic molecules can have each of its atoms move in three spatial directions. This corresponds to 3N spatial coordinates for N number of atoms. N atoms have 3N degrees of freedom available. However, there are several types of motions that become irrelevant for spectroscopic vibrations and rotations studies and must be accounted for. If all atoms move in the same direction, then they do not oscillate relative to one another. They simply travel in unison to a direction. This can occur in three directions so these degrees of freedom must be removed. Also three rotational motions may be removed which represent all molecules rotating together around a center of mass. So the total degrees of freedom for multi-atomic molecules is:

$$Z = 3N - 6 \tag{1.3.5.1}$$

For linear molecules, there are only two rotational degrees of freedom because rotation around their molecular axis is not linked with any movement of the atoms or the center of mass. Thus, a linear molecule has one more degree of freedom than nonlinear molecules:

$$Z = 3N - 5 \tag{1.3.5.2}$$

An illustration of the vibrations possible with a tri-atomic linear molecule following the normal modes of vibration rules is shown in Figure 1.3.5.1.

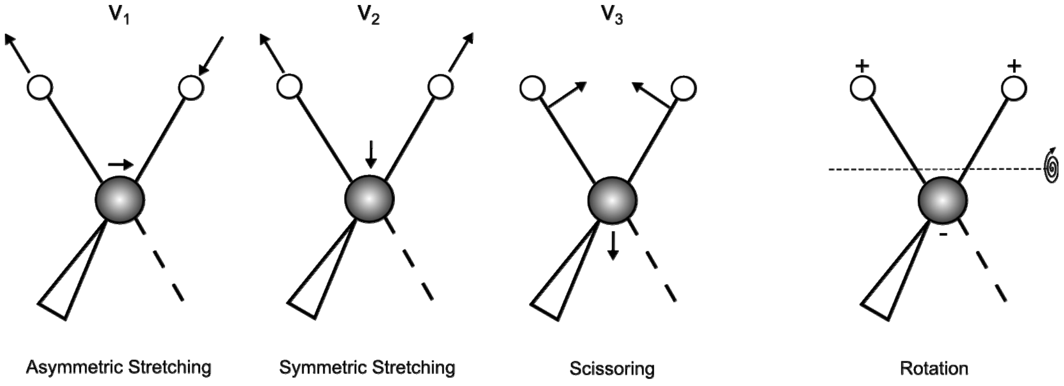

Nonlinear Triatomic molecule of H_2O

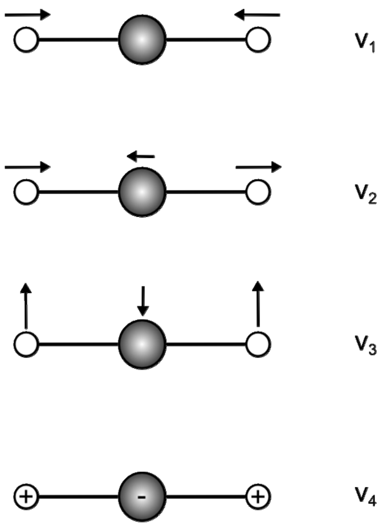

LinearTriatomic molecule of CO_2

Figure 1.3.5.1: Vibrational modes (v_1, … v_R) of nonlinear (above) and linear (below) tri-atomic molecules. The Linear molecule exhibits four vibrational modes while the nonlinear has three vibrational and one rotational mode.

1.3.6 Spectral Assertions

Spectral properties depend on the concentration and state of a substance in question. The amount of absorbed electromagnetic radiation is determined by sample density, optical path length, and temperature. Measurement of absorption involves simply finding the parameter that is the ratio of radiation intensity before and after passing through a sample. However, there are several considerations that must be taken into account specifically for the spectroscopic studies of “bulk” solid phase samples in this thesis.

1.3.6.1 Bulk Explosives Spectroscopy Considerations

In the case of bulk explosives spectroscopy studied in this thesis, only collective vibrational motions are evident in the spectra. This is due to the fact that all the samples under spectroscopic investigation are composed of solid-phase powders. The rotational motions of molecules in solid-phase (and liquid-phase) are quenched due to high rates of collisions occurring in a dense collection of neighbouring molecules [58]. While the single-bond intermolecular vibrations do occur in solid-phase explosives, they mainly give rise to the well-known infrared fingerprint features [38]. The solid-phase explosives investigated in this thesis experience a significant broadening effect and thus have a “continuum” spectra in the THz region. The spectral shape is due to the collective intermolecular motions rather than single bond vibrations. Also, due to the nature of these kinetic interactions, the spectrum becomes temperature dependent [53]. As temperature decreases, the spectral peaks become sharper and slightly blue shifted. Additional “matrix” effects are a result of the interactions with neighbouring molecules. If a THz transparent “matrix” filler substance is used to manipulate the concentration of explosive powder within the cell, the explosive molecules interact with the matrix and the collective motion is modulated. The typical matrix effect on the terahertz spectra is to broaden and shift the spectral peaks.

Regardless of these anticipated effects, the broad spectral features caused by collective intermolecular vibrational motions correspond uniquely to terahertz frequencies and still present a promising method of explosives detection.

1.3.6.2 Absorption Strengths

The absorption coefficient of the THz intensity I transmitted through a material is defined as

$$\alpha = -\left(\frac{1}{I}\right)\left(\frac{\Delta I}{\Delta x}\right) \qquad (1.3.6.3.1)$$

ΔI is the infinitesimal intensity change that occurs during a propagation through a material by an infinitesimal distance Δx. Near the microwave region limit where $hv << kT$, the peak absorption coefficient between two rotational levels p and q is

$$\alpha_{pq} = \frac{8\pi^2 NF_p v^2}{3ckT(\Delta v))}\mu_{pq}^2 \qquad (1.3.6.3.2)$$

NF_p is the number of molecules per unit volume in state p, v is the rotational transition frequency, Δv is the linewidth, and μ_{pq} contains contributions from the components of the permanent dipole moment along each of the principal axes of moment of inertia tensor that is determined by the rotational selection rules [62].

Integration of equation (1.3.6.3.1) between $x = 0$ and $x = l$, gives a relationship between incident intensity I_o and transmitted intensity I dependent on a sample thickness.

$$I = I_o e^{-\alpha l} \tag{1.3.6.3.3}$$

An additional effect was observed by Beer in 1852, that the concentration had a uniform influence on the radiation attenuation. Consequently, we define $\alpha = \varepsilon \cdot \rho$ where ε is the molar absorptivity (extinction coefficient) and ρ is the concentration. Equation (1.3.6.3.3) arrives at Beers Law:

$$\log(I) - \log(I_o) = -\varepsilon \cdot l \cdot \rho \tag{1.3.6.3.4}$$

For convenience the absorbance, "A" is introduced:

$$A \equiv -\log\left(\frac{I}{I_o}\right) = \varepsilon \cdot l \cdot \rho \tag{1.3.6.3.5}$$

Hence, the absorbance A is a measure directly proportional to the concentration and it must be considered in order to quantitatively analyse a spectrum of mixed sample explosives (e.g. in a "matrix" filler substance). However, the scope of this thesis is limited to pure samples so equation (1.3.6.3.3) applies. Further studies in mixed explosive powders and powders with matrix fillers would require absorbance calculations.

1.3.6.3 Spectral Line Broadening

In studying of transitions of atomic spectra, it is important to be aware that transitions will not manifest as precise "sharp" spectral peaks. There is an inherent "natural line width" which arises from the uncertainty in energy of the states involved in the transition. However, this broadening is rarely significant when compared with other line broadening effects such as temperature or collisional broadening caused by interactions of adjacent molecules within the sample.

Within a solid explosive sample, both homogeneous broadening (similar atom interaction) and inhomogeneous broadening (dissimilar atom interaction) can occur. Homogeneous broadening of solid explosives was found to be temperature dependent and could be represented by a Lorentz function fit curve while inhomogeneous broadening could occur if there are imperfections and impurities within the sample and the resultant spectral shape resembles that of a Gaussian curve [64]. The samples studied in this project were nearly pure so all molecules were expected to resonate in an identical, homogeneous manner in response to interaction with THz frequency radiation. The broadening caused by minor imperfections may still be represented by a multiple Lorentz linefunctions because the inhomogeneous Gaussian broadening trend is effectively composed of the homogenously broadened peaks of each molecule type involved in the system.

An awareness of this spectral line broadening effect can aid in identifying peaks in an explosive spectrum that are partially obscured by the broad signature of an adjacent broadened peak. This is an important consideration when correlating results with a database of spectral fingerprints.

1.3.6.4 Scattering Effects

Important considerations for detection of concealed explosives or weapons are factors that cause signal attenuation that are not due to vibrational/rotational energy state transitions. Ideally, in spectroscopic scans, attenuation is considered equivalent to the absorption since it is assumed that all signal attenuation is due to the energy transfer driving molecular motions. However, this is not the case when there are significant scattering effects introduced by a material blocking the optical path to the sample [65]. Studies were performed to investigate the consequences of scattering when various concealing materials were introduced [66, 67]. J. E. Bjarnason et al. investigated THz transmission through common types of fabrics in garments and baggage and observed that materials became progressively opaque at higher THz frequencies [66]. They explained that the material became "optically dense" in the higher frequency region. THz transmission became exponentially dependent on material thickness. The rate of attenuation was dependent on the type of material used, but some attenuation effect was evident for all materials. The general result of the study showed that the capability of THz chemical mapping systems is limited at high THz frequencies when dielectric material obstructions are introduced. When samples are concealed, higher THz frequency radiation signals drop below the noise floor of the detection system and can no longer resolve the spectral absorption peaks of samples.

Accurate knowledge of the balance between scattering and absorption is critical in THz applications for spectroscopy and imaging.

1.4 Bulk Explosives under Investigation

Bulk explosive spectroscopy in the THz regime is of significant interest for security applications due to the prospect of non-destructive, stand-off explosive identification capability. The ultimate goal of research in explosives spectroscopy is to develop an automated system that can scan people or packages efficiently at security checkpoints. Figure (1.4.0.1) illustrates two possible configurations for explosives detection systems in transmission and reflection spectroscopy modes.

The purpose of explosives material is to induce damage on a target. Different explosives cause damage in different ways depending on the progress of the chemical reaction and the way the explosive is prepared. Explosive reactions are exothermic (releasing energy). However, as opposed to the commonly observed slow exothermic reactions, an explosion occurs at an extremely rapid rate such that a great amount of energy is released into a small volume in a short time. This energy release can be manifested as heat and a rapid expansion of gas which, in turn, creates a shockwave or propels fragments at high velocity. During an explosion, the component molecules of an explosive undergo several, relatively simple chemical reactions in the following priority:

1. Metal + O = Metallic Oxide
2. C + O = CO (gas)
3. 2H + O = H_2O (gas)
4. CO + O = CO_2 (reaction that continues from reaction 2) (gas)
5. Release and expansion of excess O, H, N, O_2, N_2, H_2 (gas)

If there is no metal in the explosive substance such as in the case of plastic explosives, then the next priority reaction proceeds.

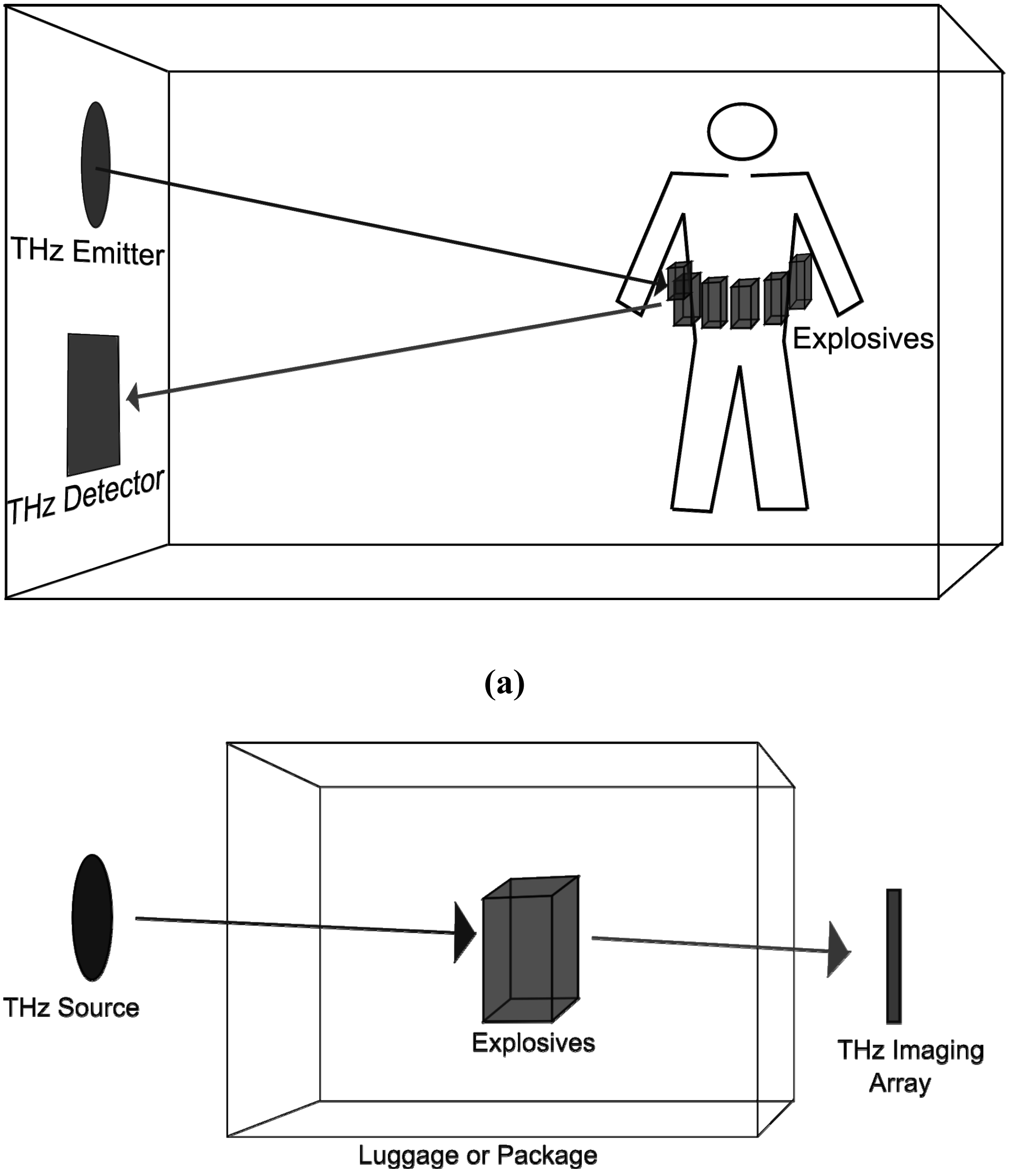

(a)

(b)

Figure 1.4.0.1: Illustration of potential implementation of THz for explosives detection in (a) reflection mode and (b) transmission mode.

The bulk explosives investigated in this thesis were homogeneous samples of military grade high explosives. The following is a list of these explosives:

Cyclotrimethylene-trinitramine (RDX)

Molecular formula: $C_3H_6N_6O_6$

RDX (abbreviated form of: Research Department eXplosive) is a crystalline white powder that is considered one of the most stable and powerful high explosives. It is found in many military grade explosive compositions. The structure of RDX is a six membered heterocyclic ring comprised of three nitrogen and three methylene groups. Nitrite groups are attached to each of the nitrogen atoms in the ring. Figure 1.4.0.2 shows the chemical structure of the RDX molecule.

Cyclotetramethylene-tetranitramine (HMX)

Molecular formula: $C_4H_8N_8O_8$

HMX (abbreviated form of: High Melting eXplosive) is a powerful and stable nitroamine high explosive. It is chemically related to RDX. Its structure is an eight-membered ring of alternating nitrogen and carbon atoms (Figure 1.4.0.2). A nitro group is attached to each nitrogen atom. Its high molecular weight makes it one of the most potent chemical explosives just below Octanitrocubane and HNIW (Hexanitrohexaazaisowurtzitane)

Pentaerythritol tetranitrate (PETN)

Molecular formula: $C_5H_8N_4O_{12}$

PETN is a powerful and stable high explosive that has a high brisance (shattering capability). It attains maximum pressure very quickly so it can potentially launch shrapnel and fragmented shells very effectively. Its structure is depicted in Figure

1.4.0.2. It is often mixed with RDX and other additives to form a common explosive compound called SEMTEX.

Composition 4 (C-4)

Contains RDX : $C_3H_6N_6O_6$

C-4 is an explosive compound composed of 91% RDX, 5.3% diethylhexyl (plasticizer) and 2.1% polyisobutylene (binder). The compound is easily shaped and is very stable so it is utilized for strategic demolition of buildings or structures.

These explosive substances are most commonly used in a mixture form as a plastic explosive such as C-4. The explosive reaction of C-4 must be initiated by a specialized detonator or blasting cap since RDX within the C-4 will remain stable even if burned by external flame or if shot with a rifle. When the explosion is triggered, C-4 violently decomposes into a variety of gasses such as nitrogen and carbon oxides as described earlier. The gasses expand at about 8050 meters per second to deliver a large magnitude of force to anything in proximity to the blast.

The explosive damage occurs in two phases. The initial expansion of gasses inflicts the majority of the damage. Then a low pressure area at the origin of the explosion results a second implosive blast due to the gases rushing back into the partial vacuum. This second energy wave is slightly less destructive than the first.

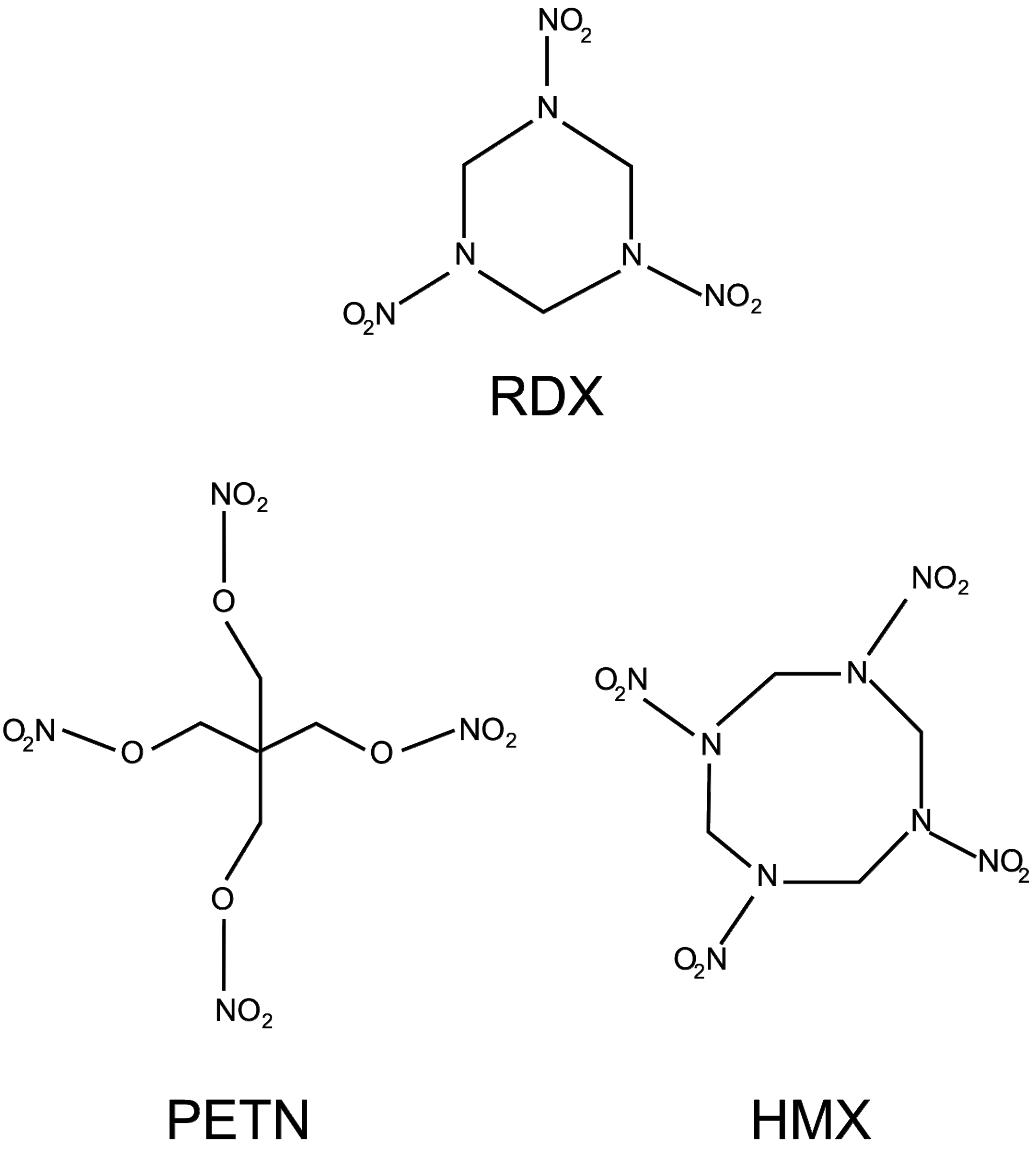

Figure 1.4.0.2: Chemical structure diagrams of cyclotrimethylene-trinitramine (RDX), pentaerythritol tetranitrate (PETN), and cyclotetramethylene-tetranitramine (HMX). Composition 4 (C-4) explosive not shown since it is composed of an RDX mixture.

1.5 Thesis Scope

In Chapter 2, a continuous wave, optical parametric oscillator (OPO) called the Firefly – THz is introduced and characterized. To further investigate the coherency and quality of the THz beam across all frequencies, a split lamellar mirror interferometer was employed to extract free-space interferograms of the THz output beam. The design and construction of the lamellar mirror was discussed and further applications in interferometry beyond laser characterization were proposed and justified.

In Chapter 3, the spectra of military grade explosives are investigated and analyzed. cyclotetramethylene-tetranitramine (HMX), cyclotrimethylene-trinitramine (RDX), and pentaerythritol tetranitrate (PETN) and Composition 4 were chemically mapped using the Firefly OPO system. The THz system was then used to determine the thickness threshold of detection for each explosive sample by using polystyrene window plates to vary the transmission pathlength through the explosive powder. Explosives spectroscopy was also performed on samples obstructed and concealed by various dielectric materials such as cloth and envelope paper. Raster scan spatial imaging of small metallic objects through concealing materials was performed to determine the transmission imaging capability of the OPO system. Concealed explosives were imaged within an envelope to demonstrate a method for screening mail for package and letter bombs.

In an attempt to confirm the results derived from the OPO Firefly-THz system experiments, a THz-TDS system is used to perform spectroscopy on the explosives. THz-TDS was a well-established method used in the laboratory so it served as a reference point to the function of the Firefly system.

In Chapter 4, a circuit was designed to form the external electronics foundation for a potential video rate THz security camera. Two potential prototype circuits were designed to utilize THz antenna detectors fabricated as quantum cascade metal-insulator-metal structures (QC-MIM). Since the THz detectors were not yet developed, LEDs set in detection mode were used as detectors and served to demonstrate the functionality of the circuit.

Chapter 2

Optical Parametric Oscillation Spectroscopy System

2.1 Mechanism of Optical Parametric Oscillations

The OPO system used for CW experiments throughout the project was an M-Squared Firefly-THz optical parametric oscillator (OPO) [68]. The following introduction describes the basic function of the Firefly OPO. For a more in-depth comprehension of the theory of optical parametric oscillation, the reader is referred to concise papers on the subject [31, 69, 70].

The vital components of the Firefly system consist of an optical resonator and a nonlinear crystal. The OPO cavity is designed to contain optical frequency oscillations and convert the input pump wave (v_{pump}) into two output waves of lower frequency signal (v_{signal})and idler (v_{idler}).

$$v_{pump} = v_{signal} + v_{idler} \tag{2.1.0.1}$$

The mechanism of this conversion is by non-colinear interaction within a crystalline gain medium within the cavity. The process of oscillation essentially involves wave amplification as the beam undergoes multiple trips within the resonator. The nonlinear MgO:LiNbO$_3$ crystal within the cavity converts a 1064 nm wavelength pump beam from a Q-switched ND:YAG source into the THz ‘signal’ beam and an ‘idler’ beam. The cavity resonates the idler wave while directing the THz (signal) wave to the output. It is the temporal and spatial overlap of pump, signal and idler waves that results in the amplitude gain for signal and idler waves, and the depletion of the pump wave. As with the typical laser conditions, a sufficient pump power is required such that the round trip gain becomes equal to the round trip losses.

The Firefly THz OPO output is a narrow band signal (50 GHz width) that can be scanned across a range of THz frequencies using a computer control console. The tuning of the signal and idler beams is performed by changing the crystal angle within the cavity and thus changing the geometry at which the three beams intersect within the crystal. The idler beam produced within the cavity can vary in frequency between 1060-1080 nm by this crystal angle tuning mechanism. A schematic of the Firefly OPO cavity is shown in Figure 2.1.0.1.

The THz output can be described as “pseudo-continuous”. 10ns long THz pulses are emitted at a slow, fixed 50Hz repetition rate with up to 10nJ of energy depending on the selected output frequency. This corresponds to a potential 0.5 μW of average output power. Although the factory specifications state that THz frequency radiation can be produced from 1.2 to 2.5 THz tuning range, this varies slightly depending on the OPO cavity calibration. After several modifications were made to the system, the tuning motor itself was able to scan the OPO frequency as low as 0.65 THz and as high as 2.7 THz.

What makes the Firefly system attractive for security applications is its ease-of-use and compact form factor. The OPO head measures 47 x 17 x 8cm, (L x W x H) and can be controlled by a ‘netbook PC’ via Ethernet communications protocol or remotely by a secured internet connection.

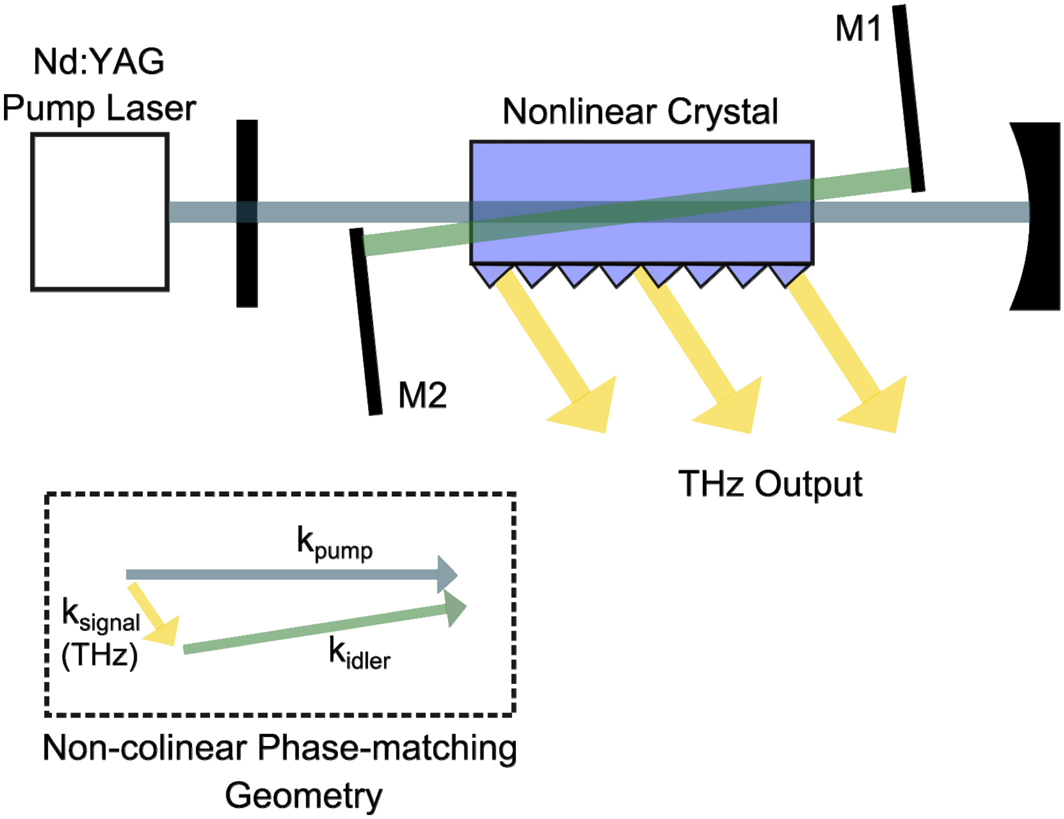

Figure 2.1.0.1: Schematic of non-colinear, intersecting cavity within the Firefly-THz optical parametric oscillator (OPO).

A Golay cell [19] optoacoustic detector (TYDEX GC-1P) was used to read the THz signal for all Firefly experiments in this thesis. The detector essentially functions as a temperature sensor. A gas inside of a sealed compartment within the Golay is illuminated by the radiation signal. The gas expands due to the thermally induced pressure increase and causes a deflection in a mirrored membrane. The degree of mirror deflection is then measured by light that is reflected off the distended membrane and detected by a photodiode. The Golay cell functions at room temperature and detects a wide range of wavelengths. Ideally, an optical chopper modulates incident radiation at a frequency of 10 Hz. However, since the Firefly OPO operates at a constant 50 Hz repetition rate, the Golay cell could be used without a chopper albeit with a somewhat diminished responsivity (21 kV/W at 50 Hz). It was found that using the Golay cell without the chopper resulted in higher amplitudes of detectable THz frequency signals despite the diminished responsivity. The GC-1P Golay cell uses a built-in 2 mm high density polyethylene (HDPE) long pass filter window to eliminate detection of wavelengths below 15 μm (filters out frequencies above 20 THz). The upper limit of detectable wavelengths is approximately 10 000 μm (filters out frequencies below ~ 30 GHz). This upper limit is not determined by the filter but rather by the aperture size of the entrance cone (11mm).

2.2 OPO System Performance

The Firefly-THz OPO outputs a different THz power depending on the specified tuning frequency. This output profile may be adjusted if calibrations are made to the OPO cavity. Although this would shift the peak power to a desired frequency, it would undermine the intended “turn key” design of the system. In this thesis, the optimized factory default cavity calibration was used for all experiments.

Figure 2.2.0.1 shows the OPO output profile across the tuneable range. This result was attained by detecting the THz signal using a Golay cell situated directly in front of the THz output window. Although focussing optics would yield higher THz intensities, this method was repeatable and most convenient for the purpose of comparison to previous day spectral frequency profiles. Furthermore, this direct detection method minimized THz signal loss due to absorption by atmospheric moisture. It should also be noted that a single tuning of the OPO THz radiation has a bandwidth of 50 GHz. The power spectrum was constructed by scanning this 50 GHz wide output across the entire tuning range of the OPO. However, this bandwidth is relatively small in comparison to the tuning frequency (~THz) so spectral density does not play a significant role. Therefore, Figure 2.2.0.1 approximates the average output power of the OPO at the specified tuning frequencies.

Figure 2.2.0.1 shows that the OPO outputs peak intensities between 8.5 – 1.05 THz and between 1.2 – 1.4 THz. At the peak frequency power point (0.9 THz), only 250 nW could be measured by the Golay instead of the bolometer detected, 500 nW specified by the manufacturer. This could be due to variations in atmospheric humidity, cavity calibration, or by the type of filter used to eliminate non-THz frequencies. At higher THz frequencies, the OPO produced lower intensity radiation.

In order to confirm the tuning operation as directed by the manufacturer, the infrared window was opened and the IR power was measured across the tuning frequency. During cavity calibration, the IR power spectrum should be maximized to yield a recommended spectral peak of approximately 10 mW and the overall shape of the spectrum should be relatively proportional to the THz output. Figure 2.2.0.2 indicates that the IR spectrum indeed follows the THz output in Figure 2.2.0.1, however the peak with maximum power was 8.5 mW. The manufacturer reassured that this result is within specifications for the OPO to be considered fully functional.

There were various noise factors from acoustic, vibrational and ambient light sources that resulted in an approximate 0.12 mV Golay signal fluctuation at all OPO tuning frequencies. Since this noise was constant, it also defined the noise floor of the signal and hence, the limit of detection. From the specified responsivity of the Golay cell at 50 Hz repetition rate (21 KV/W), the 0.12 mV fluctuation corresponds to a power noise of 5.7 nW across the tuning spectrum of the OPO. Since this noise is constant, the signal to noise ratio follows the output frequency profile shown in Figure 2.2.0.1. There also was an observable calibration drift over time that modulated the profile slightly. However, this drift was no more prevalent than the effects of variable day to day humidity and could be minimized if related experiments were completed in the same day. There was also an additional noise factor evident at the low THz extreme of the tuning range. At frequencies below 0.75 THz, the Golay cell shows sporadic fluctuations in signal from the THz radiation output window but it was difficult to quantify since these fluctuations would occur as short spikes of noise which were averaged out during the data acquisition.

For the purposes of imaging, the high intensity peak frequency regions of 8.5 – 1.05 THz and 1.2 – 1.4 THz would undoubtedly be the most effective since these regions can afford the most signal attenuation due to the high signal to noise ratio.

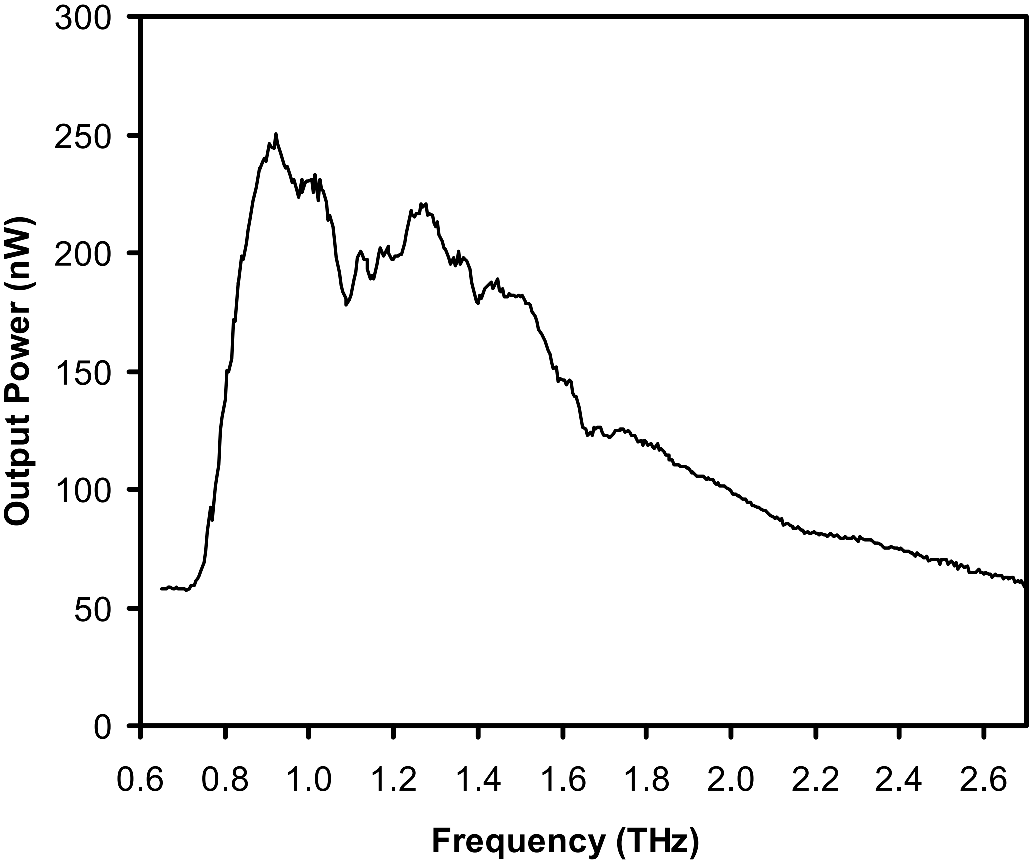

Figure 2.2.0.1: The intensity-frequency profile of the Firefly-THz OPO. A Golay cell was used to detect the signal strength directly from the THz output window. Power was determined from the Golay cell voltage signal using a responsivity of 21KV/W specified for a 50 Hz repetition rate.

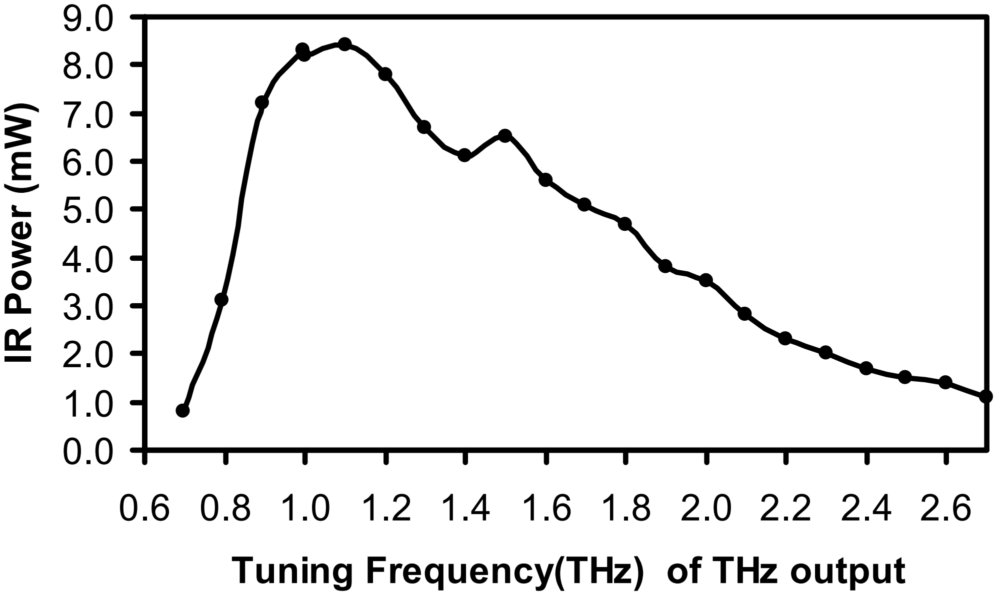

Figure 2.2.0.2: Power from the auxiliary infrared output window vs. the THz frequency tuning of the OPO. The general shape of the IR power should follow the THz profile (Figure1.2.0.1)

The noise effects could be partially mitigated by averaging the signal multiple times at each data acquisition frequency. More averages resulted in decreased noise levels, but the time interval required for the scan process increased proportionally. For most cases, three averages were sufficient in order to balance the noise vs. time expenditure.

Another notable source of instrumental uncertainty is the presence of a slight error in tuning due to the OPO software control system. By successively issuing frequency tuning commands and interrogating the OPO for its frequency tuning status, it was measured that there was a deviation between the instructed frequency and the actual frequency by approximately ± 0.75 GHz (standard deviation). The maximum deviation was ± 1.30 GHz. This is discrepancy is not significant since the bandwidth of the CW output was 50 GHz. Even during high resolution scans, these slight deviations could not noticeably affect the result of spectral analysis since the natural bandwidth of the Firefly OPO completely envelopes any potential frequency error. Figure 2.2.0.3 is a plot of confidence for the tuning instruction system for frequencies between 0.8 to 0.85 THz. Figure 2.2.0.4 shows the isolated error bars for a single sequential set of frequency instructions between 0.8 to 1 THz. The periodicity of the error in the plot suggests that the tuning discrepancies are likely due to a rounding error. If the system performs tuning on quantized steps, the instructed frequency may simply be rounded to the nearest frequency that the Firefly is capable of achieving.

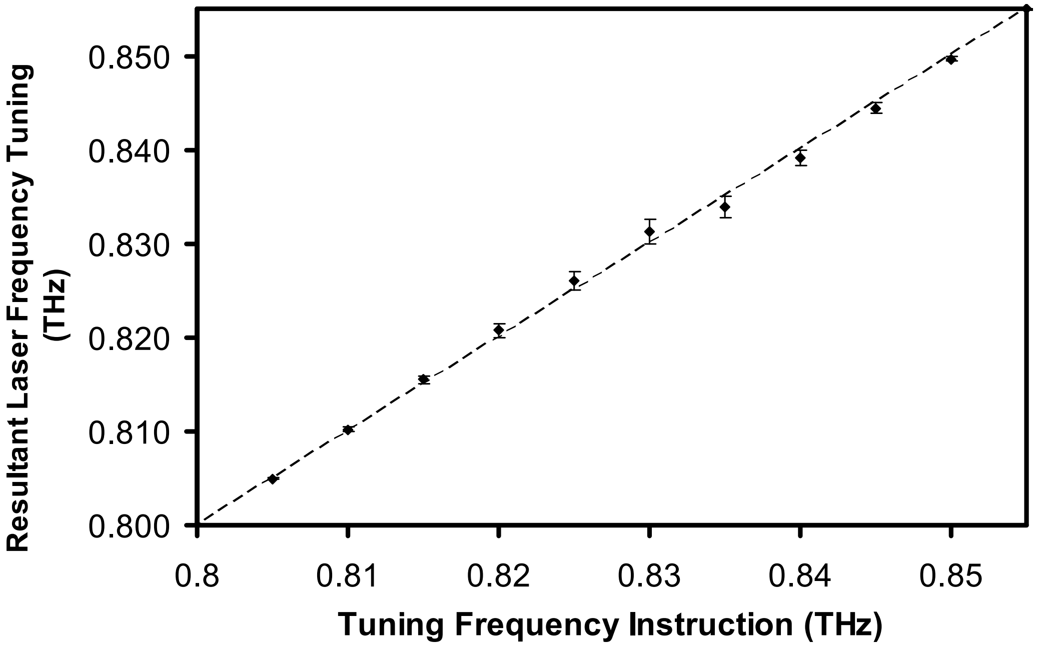

Figure 2.2.0.3: Plot of confidence for tuning frequency instruction vs. actual resultant THz output tuning that is performed by the Firefly OPO system.

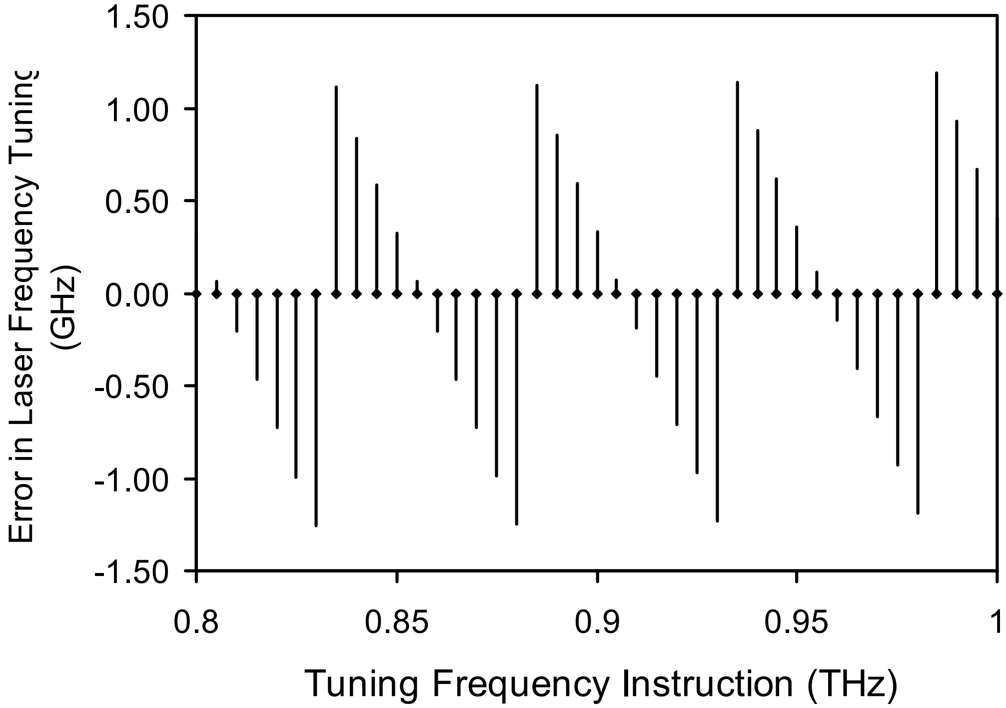

Figure 2.2.0.4: Error bars for tuning frequency instruction. The periodic nature of the error suggests that the OPO has quantized tuneable values for the frequencies. The discrepancies in tuning instruction vs. actual tuning may be due to rounding errors.

The THz beam divergence or “spread” was measured by placing the Golay cell 15 cm away from the THz output window and shifting the position relative to the center of the window. The output window of the Firefly OPO was a rectangle that measured 10×4 cm (H×W) but the output beam shape depended on the nature of the overlap of the pump and idler beams within the nonlinear crystal. For the purpose of beam characterization, an additional polyethylene film (from a garbage bag) was attached to the lens tube to suppress the collection cone action and to minimize indirect and non-THz signals. The internal Golay cell HDPE filter window was designed to pass a wide range of frequencies. Ambient air fluctuations, diffuse reflections from the Firefly OPO, and even body heat could affect the detection. Without the additional filter, these non-THz frequencies could obscure the desired THz frequency signal and yield misleading results. The collection cone was designed to catch radiation approaching at wide angles. While this wide-angle detection capability is typically advantageous for high sensitivity and ease of alignment, it is detrimental for the beam divergence test since the precise direction of the beam is parameter of interest. The filter attachment effectively narrowed the aperture, decreased the angle of detection, and thus counteracted the wide-angle collection cone. Figure 2.2.0.5 shows the power detected by the Golay cell as a function of angle with respect to the output window. Figure 2.2.0.6 illustrates how the characterization was performed. The maximum signal was detected at 52 degrees from the THz output window. The full width half maximum (FWHM) of the plot is 5 degrees. At 15 cm detector distance, this corresponds to an arc length of translation of 1.3 cm. At this relatively small angle, 1.3 cm also approximates the physical beam width. However, it is important to note that, despite the advantages of the additional polyethylene filter, some of the desired THz signal is attenuated as well due to minor scattering effects discussed in Section 1.3.6.8. The filter may have attenuated the sides of the spatial profile below the noise floor of the Golay cell, thus making the beam appear narrower.

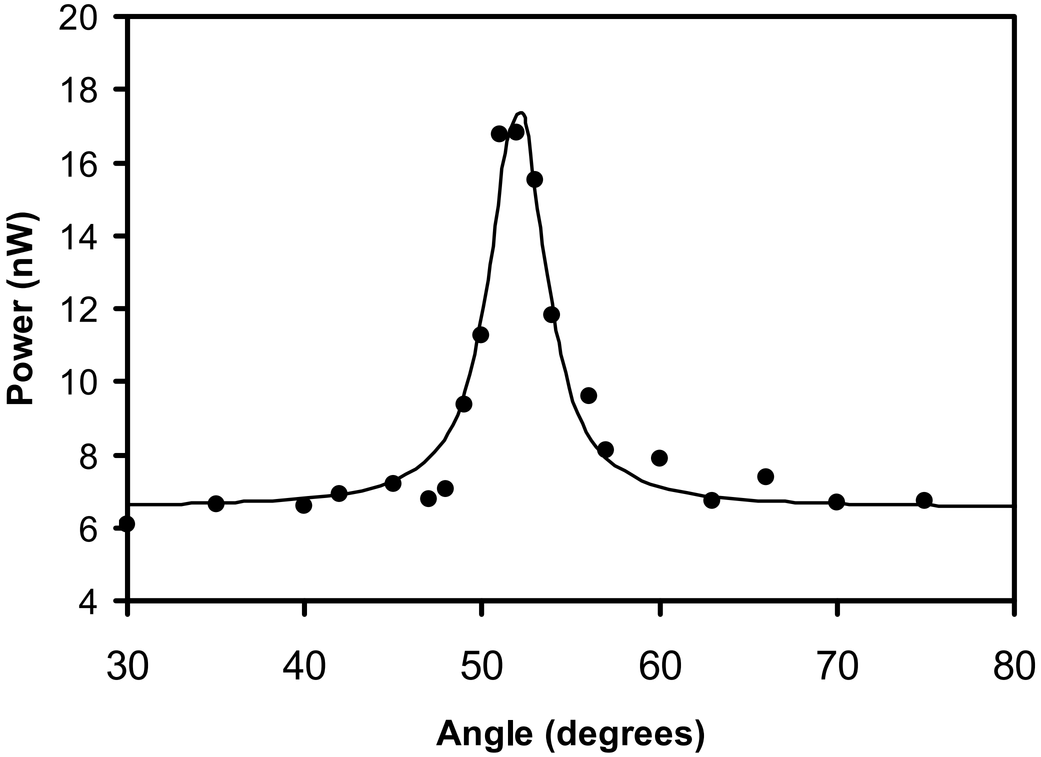

Figure 2.2.0.5: Golay cell detected THz power as a function of angle from the output window. The points on the plot represent the measured Golay cell voltage signal converted to power using 21 KW/V responsivity specified for 50 Hz repetition rate signals. The data points are fit to a Lorentz lineshape represented by the solid line.

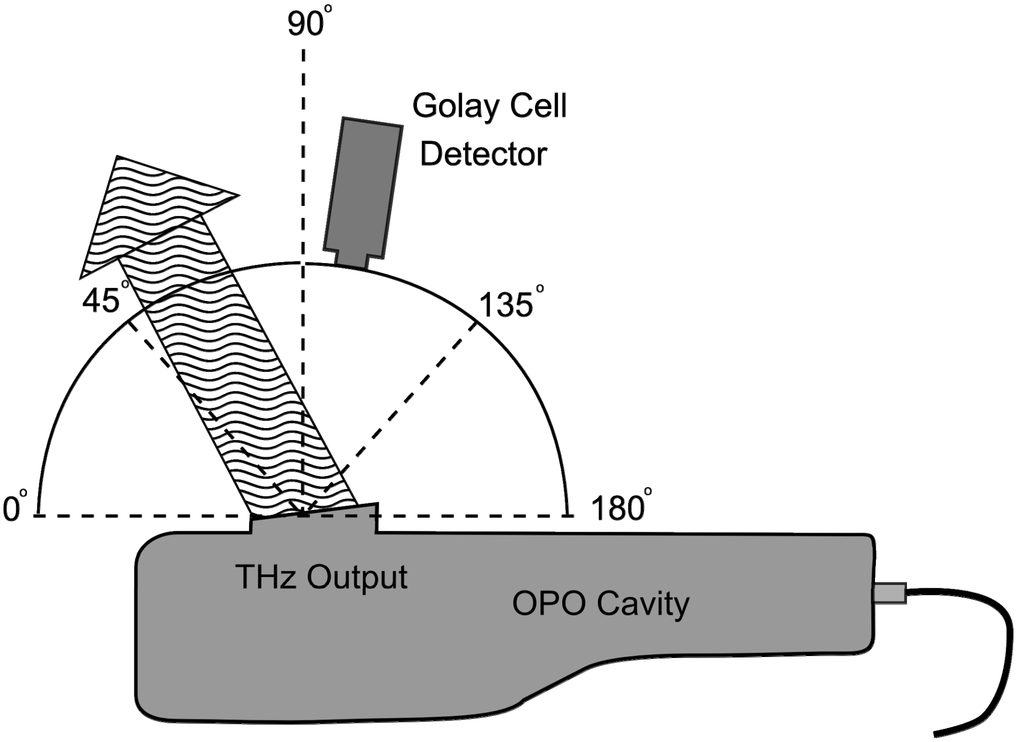

Figure 2.2.0.6: Scheme for determining THz emission angle and beam divergence from Firefly OPO

Terahertz signals are highly attenuated by absorption due to atmospheric water vapour. In order to quantify this behaviour, the Golay cell was set at the maximum THz output angle of 52 degrees determined earlier and the THz signal was measured while the detector was incrementally shifted further from the output window. The results are plotted in Figure 2.2.0.7. As would be expected, the THz power decreases as the beam path length is extended. Note that the polyethylene filter was attached during the characterization. If the filter is removed, the range of readable signal propagation extends to nearly a meter; however, there is uncertainty that the detected signal would be purely THz.

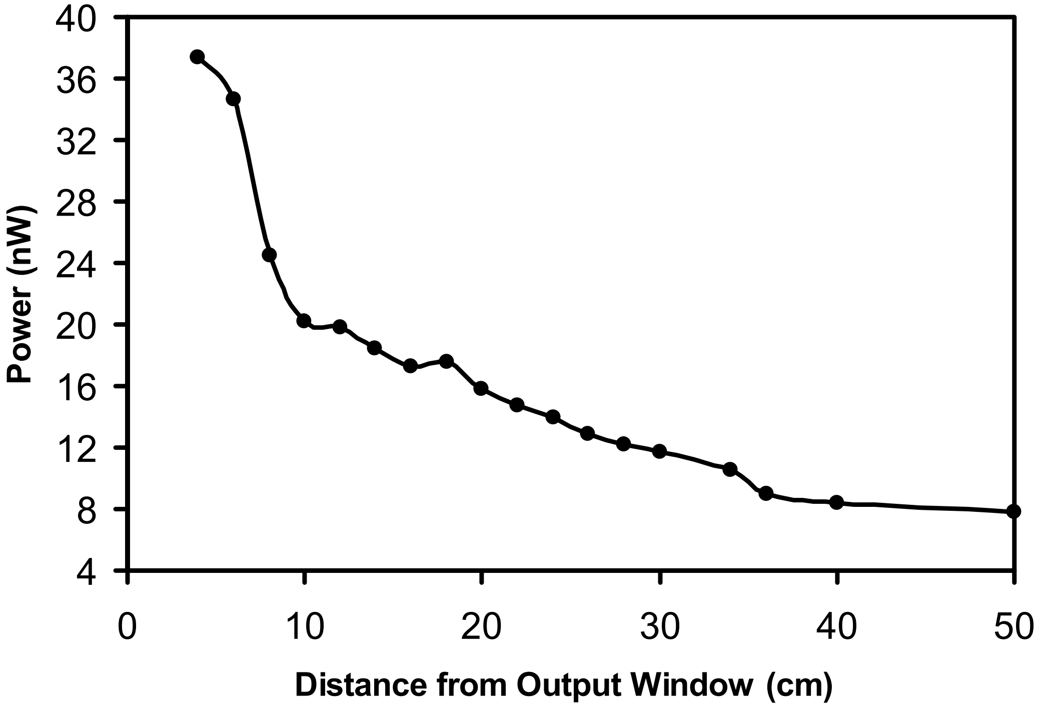

Figure 2.2.0.7: Plot of THz power as the detector is moved away from the Firefly THz output window. The noise floor is at 5.7 nW so at 50 cm distance, the signal becomes barely resolvable. Power was determined using Golay cell responsivity value of 21 KV/W.

2.3 THz Split Mirror Interferometer

The most practical and cost-effective method of detecting continuous wave THz radiation from the Firefly OPO was by thermal detection using a Golay cell detector. However, the Golay cell signal cannot indicate the frequency of the radiation it detects. All radiation frequencies are detected indiscriminately so long as they lie within the frequency band passed by the filtering elements.

This limitation of the Golay cell detection provided the motivation to design and construct an interferometer device that is capable of confirming the frequency output of the Firefly OPO. Specifically, there was an instance when a minor malfunction occurred in the OPO control system whereby the interface incorrectly displayed frequency tunings that did not match with the actual output of the OPO. The Golay cell, alone, could not diagnose this error. Without, first, having means to test the Firefly system and confirm correct frequency tuning functionality, reliable spectroscopy could not be performed.

A lamellar split mirror interferometer was found to be the most suitable interferometer design for the purpose of THz OPO system. In terms of functionality, the lamellar mirror resembles that of a standard Michelson interferometer [61]. However, the lamellar design greatly simplifies the optical set up and bypasses the need for beam splitting optics and delay lines that would otherwise be required in the Michelson interferometer design. Instead, the beamsplitting action and differential delay is achieved simultaneously by a moving split mirror mounted on a translational stage. This approach is particularly advantageous for THz frequency applications since beamsplitters and lenses are highly absorbing of THz frequency radiation. Other advantages of the lamellar mirror interferometer are: polarization independence, and minimized dispersion from reflections. The directness of the optical path minimizes THz atmospheric absorption due to moisture while simultaneously limiting vibration noise effects, which are typically aggravated by long beam paths. Alignment was also greatly simplified by the compact design. Interferometery experiments could be easily performed in the THz regime with the use of this lamellar interferometer and a Golay Cell as the detector for the interfering beams.

2.3.1 Basic Theory of FT Interferometry

The basic idea of Fourier transform (FT) interferometry involves the splitting of a beam of light into two beams which then follow paths of slightly different distance (optical path difference). As mentioned earlier, the most basic device that does this is the Michelson interferometer [61]. The device employs a beamsplitter that transmits half the incident radiation and reflects the other half. The two beams, reflected and transmitted travel their respective paths and meet again at the detector. To construct the interferogram (i.e. a plot of light intensity versus optical path difference) one of the optical beam paths distances is varied by a mobile mirror while the other beam maintains a constant path-length, encountering only stationary mirrors. The interferogram is formed by detecting the interference intensity of the two beams at the point of detection for each interval of mirror displacement. The power reaching the detector is varied by the phase difference between the two beams. When two beams are "in phase", the power is maximized. When two beams are "out of phase", the power is minimized. Specifically, destructive interference occurs according to the relationship $2d = (n + 1/2)\lambda$ where n is an integer, λ is the wavelength, and d is the distance of mirror translation from the point of at which both beams undergo an equal path length. $L = 2d$ is the beam path length difference of collinear beams at the detector location since the beam path difference is twice the mirror displacement (approaching beam and reflected beam). Constructive interference occurs when the beam path difference is $2d = n\lambda$. A typical Michelson interferometer design is shown in Figure 2.3.1.1.

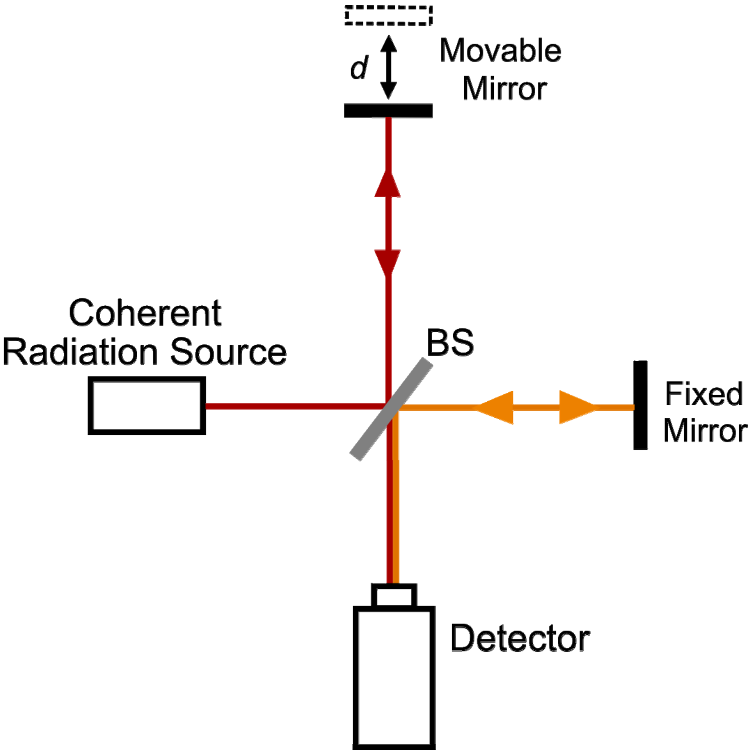

Figure 2.3.1.1: Schematic of a Michelson interferometer set-up. A coherent light source emits a beam that is split into two by a beamsplitter (BS). The reflected beam is directed toward a movable mirror while the transmitted beam is directed toward a fixed mirror. Both beams meet at the detector and undergo constructive or destructive interference depending on the mirror translation, d , from the position of equal beam path length.

In order to perform spectroscopy with an interferometer, a sample is placed in the path of the stationary beam. The frequency content differences between the sample beam and the reference beam would be evident in the interferogram.

Ideally, an interferometer creates a symmetric interferogram. The frequency content of the radiation is completely contained in the interferogram and can be extracted using a fast Fourier transform (FFT) algorithm common in many commercial software packages [57]. The FFT is essentially an optimized algorithm to determine the discrete Fourier transform. The discrete Fourier transform converts a function in the time domain into a function in the frequency domain. In the case of an interferometer, the spatial dimension of the relative mirror displacement can be converted into the time domain by considering the time of electromagnetic wave propagation (factoring-in the speed of light). For a more in-depth treatment of Fourier transforms, please refer to textbooks on digital signals processing [71, 72].

When the expected output of the OPO is a continuous wave, there is an alternative method to FFT, which is easier, more intuitive, but less accurate in determining the peak CW output frequency using an interferogram. Measuring the distance between two peaks or two troughs in an interferogram gives the wavelength, which can then be converted to a frequency value. However, this method is merely a qualitative calculation and does not give any information on the bandwidth of the CW signal, nor does it identify other potential frequency components that may not be evident by visual inspection of the interferogram.

2.3.2 Design of Lamellar Mirror Interferometer

The lamellar mirror interferometer is essentially a mirror that is split into two interleaved sections such that the shape of the mirror pieces fit into each other. The pieces fit in so that one interleaved section is free to translate with respect to the other section in the normal direction. The system is aligned such that half of the THz beam is incident on each movable mirror segment. The beam must be collimated to be wide enough to cover each mirror as evenly as possible. This type of mirror interferometer design was implemented in the past for infrared interferometry [73, 74]. Eisele et al [75], modified the interferometer design to suite the THz regime.

In order for the interferometer to function for THz frequencies, the geometry of the interdigitated mirror segments were designed to be maximally reflective to THz radiation in the frequency range of 0.6 – 3.0 THz. The sizes of the lamellar segments were chosen based on a simple diffraction theory [76]. In order to avoid polarization effects, the height, h, of each of the lamellar segments should be $h > 2\lambda_{max}$. Where λ_{max} is the maximum wavelength the interferometer would reflect. The height, h, was selected to be 5mm for each of the 12 segments in order to comfortably detect a lower frequency limit of 0.3 THz (1 mm wavelength). A schematic of the design of the lamellar mirror stage is shown on Figure 2.3.2.1. Figure 2.3.2.2 shows how the optical set-up was configured and illustrates the way the phase difference is induced in the THz radiation beam. Ideally the phase difference in the beam would be produced by configuring the mirror for normal reflection. However, this was not practical since the THz beam would simply return to the source and no detection could be performed. Instead, the mirror was turned slightly with respect to the THz beam to cause a slightly oblique angle of incidence measured at nine degrees. The slight change path difference caused by this angled geometry was compensated in calculation by a trigonometric factor: $\cos(\theta)$, where θ is the nine degree angle. The beam path length difference becomes $L = 2d\cos(\theta)$ rather than the previously mentioned $L = 2d$ for the Michelson interferometer case. The relationship for constructive interference becomes:

$$2d\cos(\theta) = n\lambda \tag{2.3.2.1a}$$

And the relationship for destructive interference becomes:

$$2d\cos(\theta) = (n + 1/2)\lambda \qquad (2.3.2.1b)$$

Where, as defined earlier n is an integer, and d is now the relative displacement of lamellar mirror segments.

The frequency resolution of the system is defined by $\Delta v = c/(2d_{\max}\cos(\theta))$ [76]. $d_{\max}$ is the maximum displacement of the mirror and c is the speed of light. In these trials, the maximum translation was set to $d_{\max} = 10$mm so that $\Delta v = 15$ GHz. This value is smaller than the specification bandwidth of 50 GHz for the Firefly system so the lamellar mirror should be capable of discerning the output frequency bandwidth of the OPO. Note that in order to improve the resolution, it is possible to simply increase the maximum displacement of the mirrors. However, an increase in displacement increases the spatial misalignment and defocusing of the beam on the Golay cell. As the mirror segments part, the focus points of the two reflected beams separate due to the oblique angle reflection. 10 mm displacement was chosen because this formed the cleanest spectrum for this particular optical alignment while still offering a resolution capable of discerning the narrow band of the Firefly.

To form a sufficiently reflective and optically smooth surface for THz, a gold coating was evaporated on the lamellar glass plates. The plates were cut out of optically smooth fused quartz photolithographic mask substrates. Approximately 20 nm of chromium was deposited as an adhesion layer and 150 nm of gold was evaporated on top of the chromium.

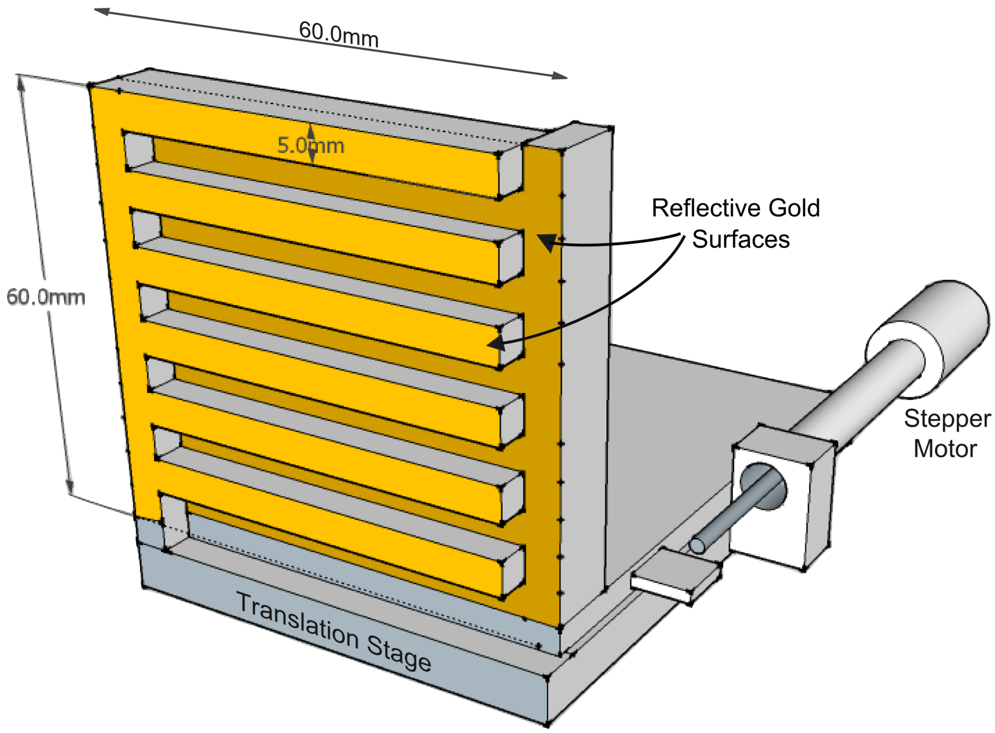

Figure 2.3.2.1: Lamellar mirror interferometer schematic drawing. The right most portion shows the motor configuration. The translation stage allows the plates of the interdigitated mirrors to slide past each other as the motor turns. For a photograph of the lamellar split mirror, see Appendix A.

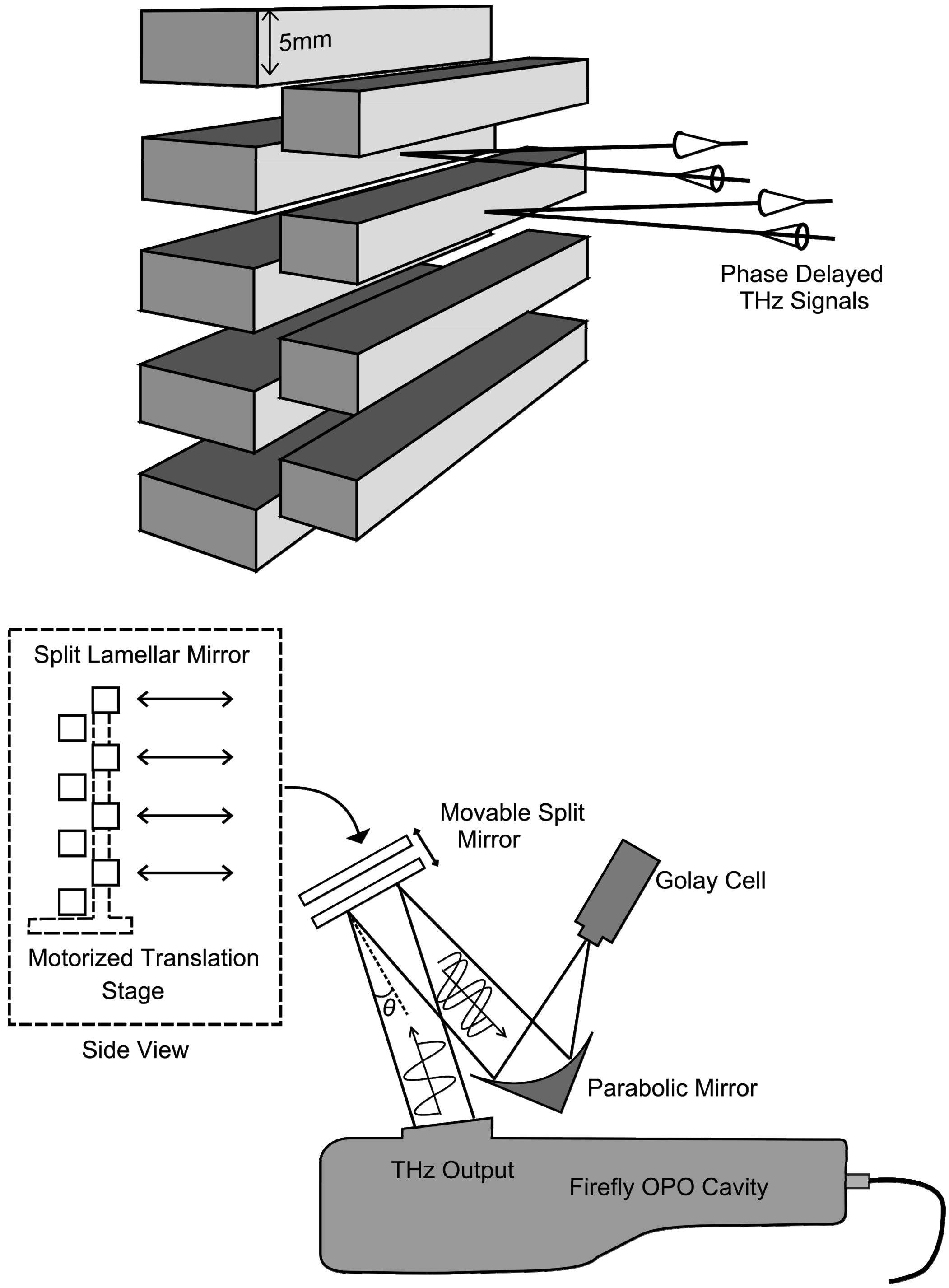

Figure 2.3.2.2: The upper image is a visualization of the phase delay concept for the lamellar mirror. The lower image is an optical set up for the interferometric experiments. θ is the nine degree angle used as the correction factor in equations 2.3.2.1a and 2.3.2.1b.

2.3.3 Data Collection and Methodology

The characterization of the Firefly OPO began with setting the system to output a single frequency. The THz output of the OPO was a collimated beam so additional collimating optics were not required. The interferometer was placed directly in front of the output approximately 30 cm away to allow sufficient space for reflection beams. The reflected beam was then directed to a parabolic mirror which focused the phase shifted beams into the Golay cell (with the extra polyethylene filter removed). Once the alignment was completed for optimal detection, the lamellar interferometer motor was instructed to move 4000 steps of 2.5 μm increments. Before beginning the scan sequence, the mirror was centered and offset by -2000 steps so the maximum peak of the interferogram occurred in the center of the interferogram. Note that, although the steps of the motor were 2.5 μm increments, the path length of the THz light beam changed by 5 μm at each step since two arms of the beam (incident and reflected) were both changed by 2.5 μm at each step. The same interferometry procedure was repeated at individual frequencies spaced by 1 THz tuning increments spanning the entire tuning range of the Firefly THz OPO. In order to control the motor and collect the data, a control interface was written in MATLAB (see Appendix E). An oscilloscope was used to read the Golay cell voltage signal corresponding to the intensity incident on its collection window. Future iterations of the design could completely bypass the need for an oscilloscope. With a data acquisition interface, the Golay signal could be communicated directly to a computer system. However, for the purposes of this prototype, the oscilloscope aided in alignment, debugging and fixing problems that would be otherwise undetectable. The data collected by the oscilloscope was transferred to a computer where it was integrated and averaged over three data points. Once the entire scan has completed, the software performed a fast Fourier transform (FFT) to reveal the spectral content.

2.3.4 Interferometry Results and Discussion

The lamellar mirror experiments indicated that the Golay detector had limited capabilities in sensing the Firefly OPO frequencies higher than 1.8 THz, while lower THz frequencies remained distinguishable and coherent. Figure 2.3.4.1 shows an interferogram of the THz output of the Firefly while it is tuned to 9.0 THz. The maxima and minima are clearly visible and periodic. Under closer inspection (Figure 2.3.4.2) it is evident that this signal has a great deal of noise. The sinusoidal shape appears almost triangular. There were some noise effects evident in interferograms for all frequencies tested. The system was capable of reducing the noise by performing more data averaging, however, the scan becomes unreasonably time consuming if more than four averages are taken. The Figure 2.3.4.3 shows the FFT of the interferogram shown in Figure 2.3.4.2 and indicates that, despite the noise effects, the frequency content is well defined by a spectral peak at 9.0 THz. The wavelength can also be easily estimated by calculating the distance between two peaks in Figure 2.3.4.2 and dividing by the number of peaks in between. In this plot, the wavelength is approximately 0.3305 mm, which translates to a 0.907 THz CW frequency which is consistent with the FFT result. Similar interferograms performed at a high frequencies yield less definitive results. Figure 2.3.4.4 shows an FFT of THz output for 1.8 THz tuning. The 1.8 THz spectral peak is barely resolvable at this in the plot. The amplitude of the spectrum is much lower and there were higher noise peaks at the low frequency portion of the plot. This low frequency noise is attributed to the spatial depth misalignment as the mirror planes moved. The focus of the THz beam could not be perfectly centered at the entrance of the Golay cell since the mirror surface must be moved to perform the scan. The low frequency noise exists for all frequency tunings, but becomes particularly strong with longer scan displacements. Also the figures appear to also have a periodic sinc function shape along the bottom of the signal plot. This is due to the zero-padding of the FFT. Zero padding is used in FFT in order to artificially improve the resolution of the FFT. This process is essentially an interpolation of the frequency domain. Extra zeros are added to the end of the time domain data to extend the number of data points. When zero padding is performed, the function is effectively multiplied by a rectangular box window in the time domain which, in the frequency domain, translates into convolving the original function with a sinc function and results in a sinc-like output. Figure 2.3.4.5 is a superposition of all the FFT transforms together. It is evident from the plot that at 1.9 THz and above, the THz output is no longer resolvable using the interferometer and Golay cell detector method.

The frequency resolution limitation for the interferometer is determined by the step size interval of the motor, which is considerably smaller than the wavelength of the radiation. The interferometer effectively traces out the waveform of interference as the phase is shifted. If the wavelength is too short (high THz frequencies), there may not be enough data acquisition points to trace the waveform. The intervals of the step sizes in the trace must be smaller than the wavelength of the radiation being analyzed. The 1.8 THz frequency corresponds to a wavelength of 166.5 μm so a 5 μm step configuration should have no difficulty resolving the radiation. However, noise effects combined with a relatively large step size could prevent a clear interferogram at high frequencies. To ensure that resolution was high enough at shorter wavelengths (high THz frequencies), an alternative “halfstep” driver stepper for the motor was used. However, no improvement was observed in the results. The Fourier transform amplitude dropped off at 1.9 THz regardless of the step size. The frequency limitation may also be attributed to the Golay detector’s limited ability to sense low power THz radiation. The THz radiation output from the Firefly is lower at higher frequencies. Also, the THz radiation experiences significant attenuation through atmospheric absorption. Due to these combined factors, it is possible that noise floor of the Golay cell overtakes the signal amplitude for frequency tunings above 1.9 THz by the time the radiation reaches the detector.

A dotted outline is shown in Figure 2.3.4.5, draped above the superimposed FFT plots for each frequency tested. This dotted line implies a more accurate representation of the Firefly OPO frequency profile that is detectable by a Golay cell than what was provided by the direct Golay cell detection intensity scan. Although, in the previous section 2.2, it was shown that the OPO was capable of outputting power at frequency settings all the way across the tuneable range up to 2.5 THz, this experiment shows that the high frequency radiation above 1.8 THz is not “useful” for spectroscopy since its frequency content is of too low amplitude. There is less confidence in data collected using the Firefly OPO coupled with the Golay cell detector for frequencies above 1.8 THz. This is a more stringent limitation than the 2.5 THz tuning limit suggested in the previous section (Figure 2.2.0.1). However, it is a more realistic constraint. With this in mind, all spectroscopy plots in this thesis were truncated just around the usable region of the THz spectrum 0.6 THz to 1.9 THz.

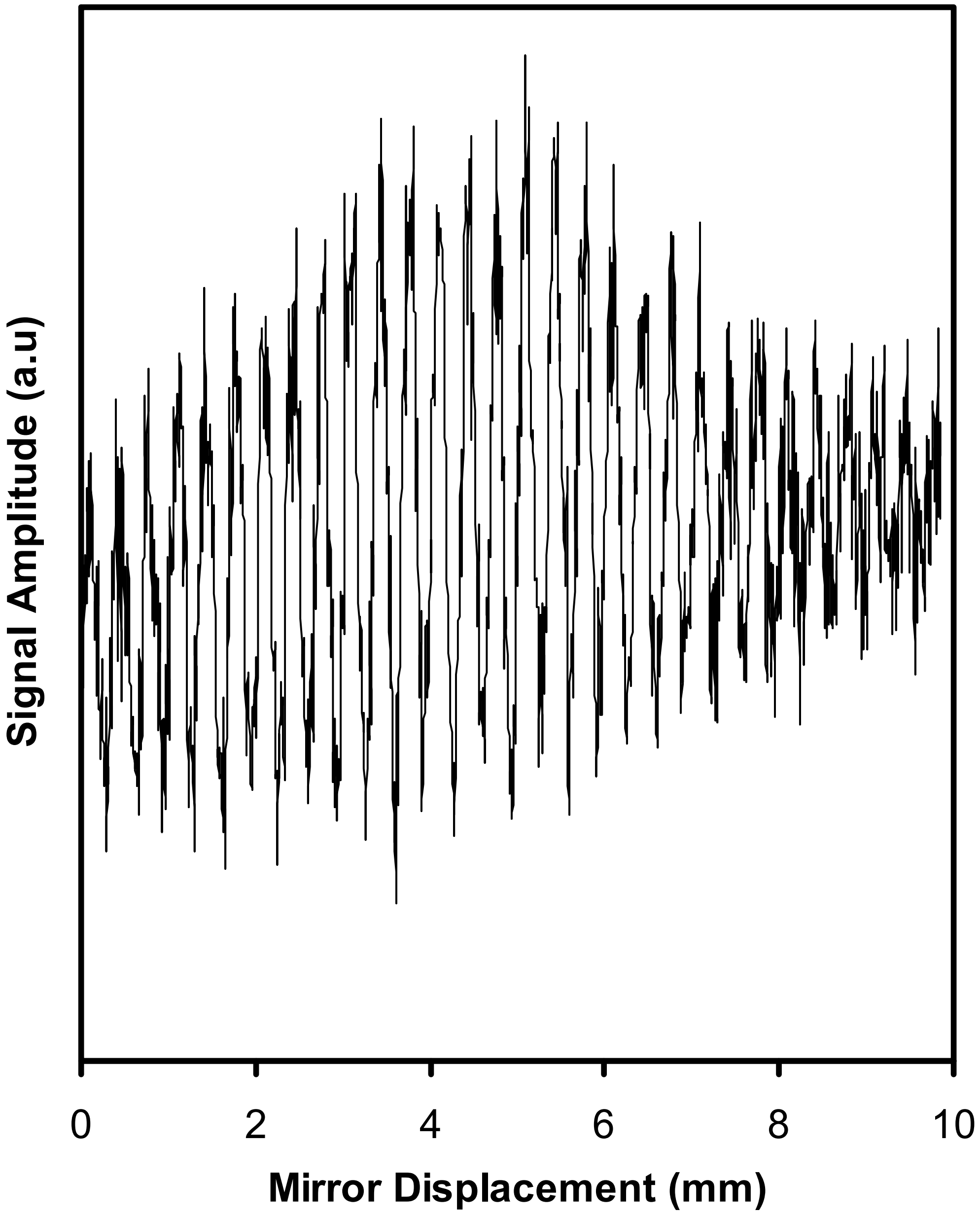

Figure 2.3.4.1: Interferogram generated using the lamellar mirror interferometer scanning 10mm of phase displacement at step interval resolution of 5um (2.5um motor stepping). The Firefly OPO was tuned to at 0.9 THz continuous wave frequency.

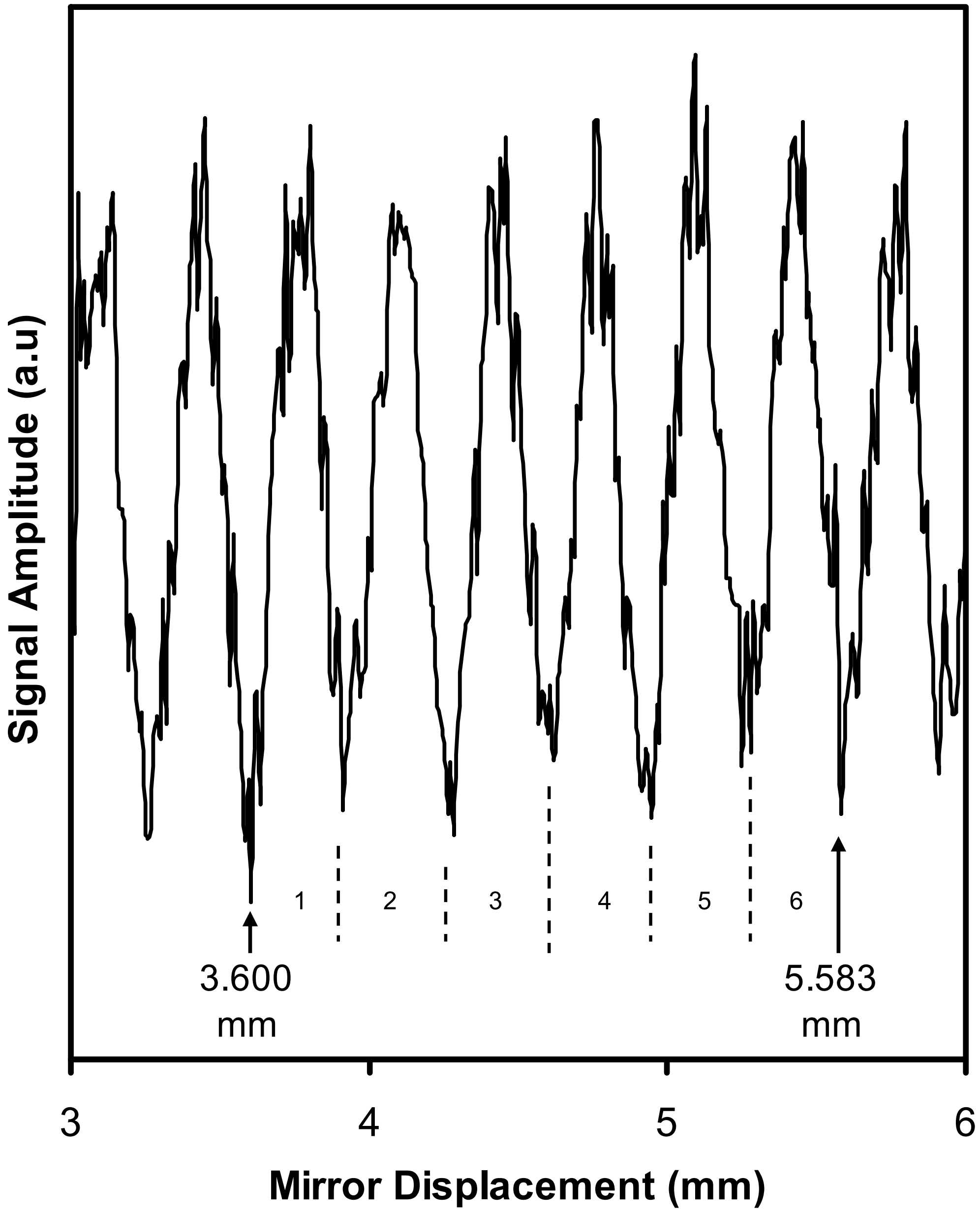

Figure 2.3.4.2: Close up of interferogram at 0.9 THz frequency tuning. Noise effects are evident at the peaks and troughs. Wavelength of the THz frequency beam can be estimated by calculating the distance between two peaks and dividing by the number of peaks in between. In this plot, the wavelength is approximately 0.3305 mm (0.907 THz).

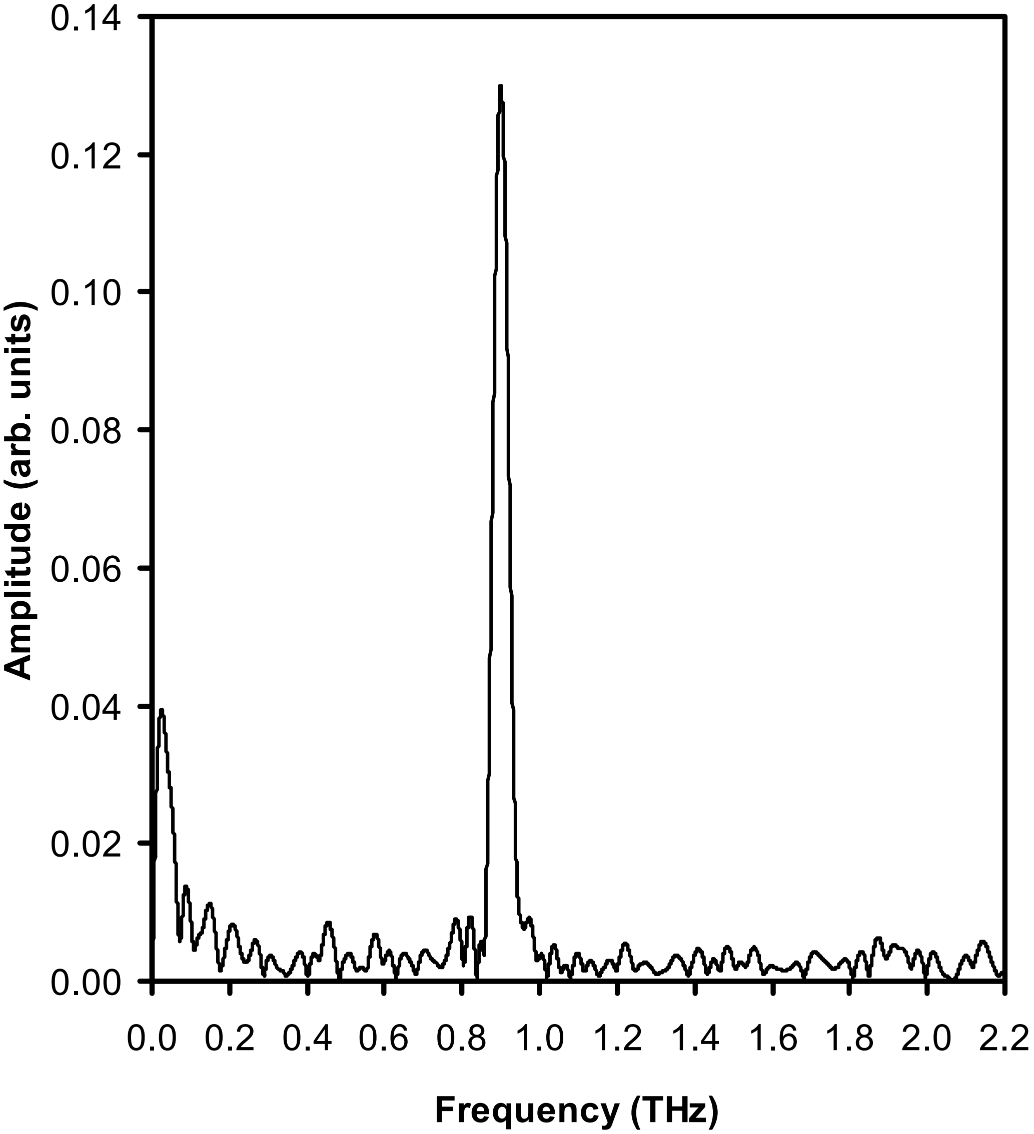

Figure 2.3.4.3: Fast Fourier transform (FFT) of interferogram generated by MATLAB software. The Bandwidth was found to be 48 ± 3 GHz.

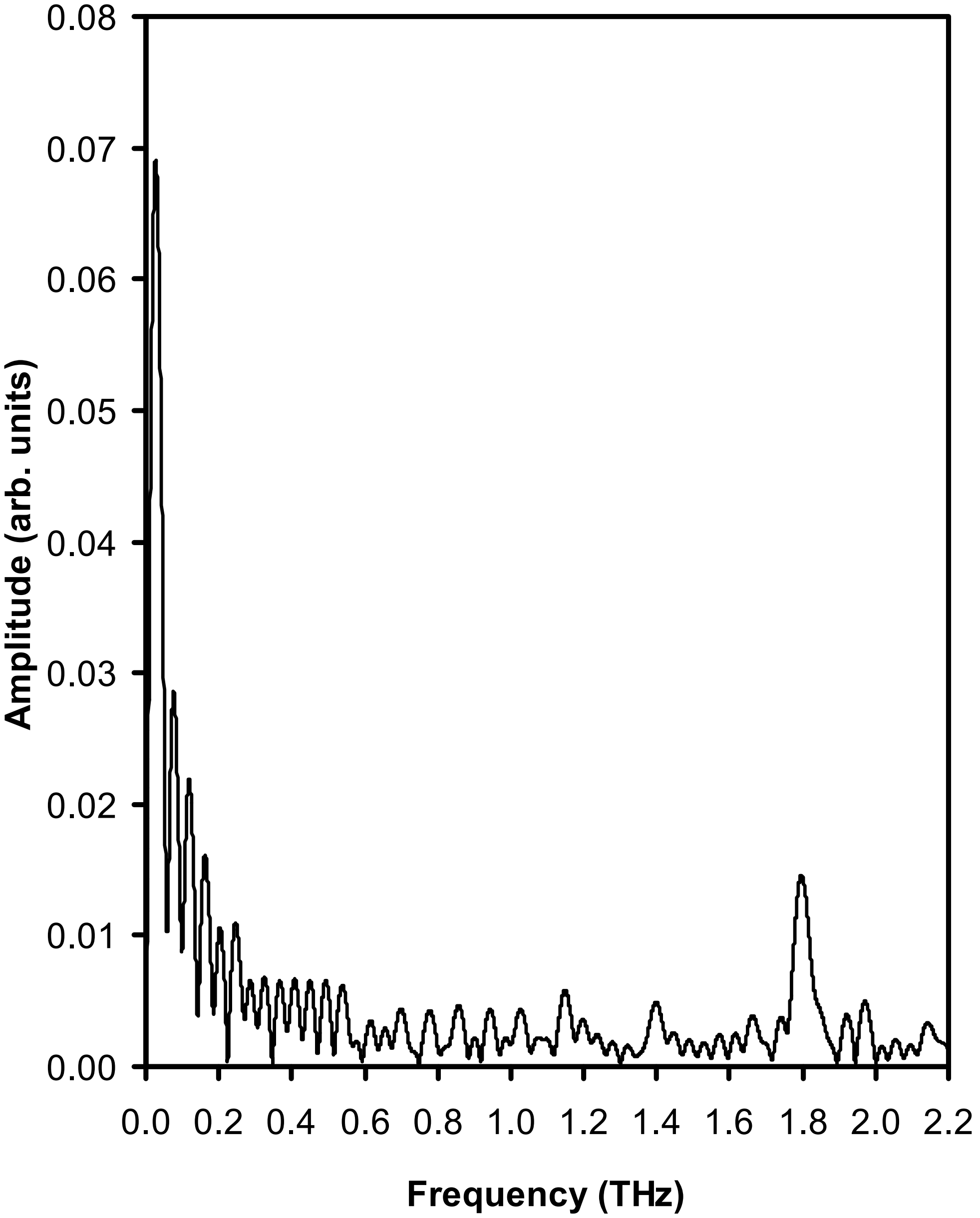

Figure 2.3.4.4: Fast Fourier transform (FFT) of an interferogram made for the 1.8 THz firefly tuning. The interferogram was generated using half step phase intervals of 2.5 μm (1.25 μm motor stepping) It is evident that this tuning frequency yields a much less distinguishable FFT frequency profile. The periodic peaks are artefacts from the noise combined with the effects of apodization and zero-padding in the FFT.

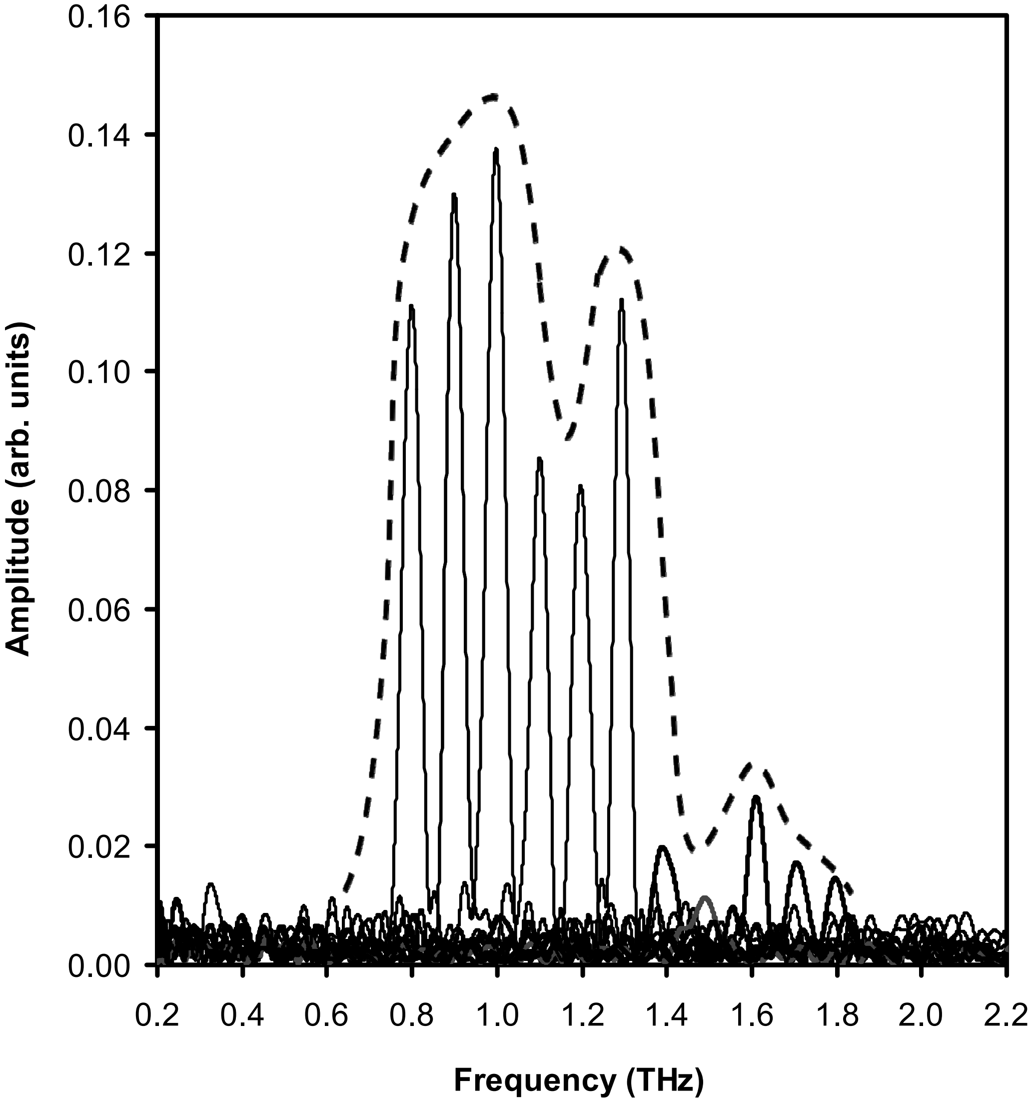

Figure 2.3.4.5: Multiple frequency FFT transforms superimposed on one plot. The Dotted line draped over the FFT transforms indicates a more reliable frequency profile for the Firefly THz OPO system when used with the Golay detection scheme. Although Figure 2.2.0.1 indicates that the Firefly emits THz radiation as high as 2.5 THz, this result shows that the Golay may not be able to detect these high frequencies after it is attenuated by atmospheric moisture and reflection.

In addition to the tuning frequency characterization, the interferometer was also used to confirm the bandwidth of the OPO output. The measurement was taken as a full-width half-max (FWHM) calculation of the FFT plot for each frequency tuning. The bandwidth was found to be 48 ± 3 GHz which was consistent with the original specifications of the OPO system which was stated as a 50 GHz bandwidth.

2.3.5 Interferometer Motor Control GUI

The interferometry results seen in the previous sections were collected using a program specially designed for this purpose. A MATLAB code, graphical user interface (GUI) was written to simultaneously control the motor system and to perform data acquisition (Appendix E). The program essentially functions by instructing an external microprocessor (Arduino Deumilanove [77]) to step the motor, then instructing the oscilloscope to record and transfer the Golay signal waveform back to the computer, and then integrating the signal and recording the results. This process repeats for the indicated number of steps, and then it performs a fast Fourier transform (FFT) of the acquired interferogram. A screenshot of the graphical user interface is shown in Figure 2.3.5.1. The following are descriptions for the various fields and pushbuttons.

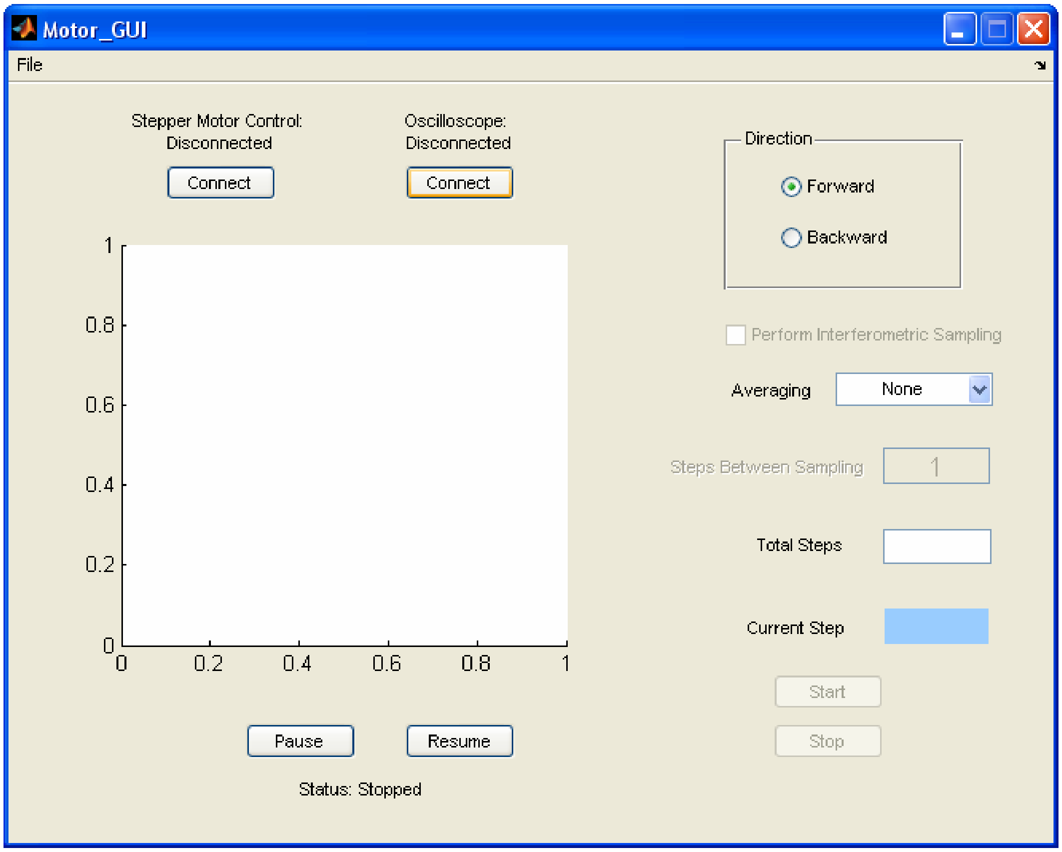

Stepper Motor Control: Disconnected

Oscilloscope: Disconnected

● Forward

○ Backward

☐ Perform Interferometric Sampling

Averaging: None

Steps Between Sampling: 1

Status: Stopped

Figure 2.3.5.1: Screenshot of the MATLAB graphical user interface designed to control the interferometer stepper motor and acquire the interferogram.

Stepper Motor Connect [Push Button] Connects the GUI to the stepper motor through the Arduino board.

Oscilloscope Connect [Push Button] Connects the GUI to the oscilloscope making measurements of the THz signal arriving at the Golay Cell.

Direction (Forward/Backward) [Toggle Radial Buttons] Indicates the direction of advancement for the stepper motor.

Perform Interferometric Sampling [Checkbox] Specifies weather to plot the interferogram or to adjust the motor position without acquiring any data.

(This box is greyed out unless both the oscilloscope and the stepper motor is connected)

Averaging [Scrolldown] Selects the number of averages to take for each step. Higher average values reduce the noise level but increase time required for the scan.

Total Steps [Text Box] User input to instruct the motor on the total number of steps to take during a reading

Steps Between Sampling [Text Box] User input to instruct the program to take specific number of steps between each data acquisition sequence. (only available if "perform interferometric sampling" checkbox is checked)

Current Step [Display box] Indicates to the User what is the current motor step in the interferometric scan.

Start/Stop [Push Buttons] Instructs the program to begin scan or to terminate scan. Pressing start after pressing stop begins the program from the beginning.

Pause/Resume [Push Buttons] Instructs the program to pause at the current step or resume from the pause location

The plot axis displays the interferogram in real time during the scan. A Fourier Transform of the resulting interferogram opens in a new window once the scan is completed.

2.3.6 Future Prospects for the Lamellar Interferometer

The design of the interferometry system could be improved and adjusted to suit more specific applications. Certain limitations such as the misalignment that occurs during the scan may be rectified by assembling a moving platform for the Golay cell detector so that it may follow the beam center. The system could also benefit from more advanced focusing optics. Although the output of the Firefly OPO is collimated, a lensing system could result in less loss and a higher THz intensity over the surface of the split lamellar mirror.

The lamellar mirror system has potential applications beyond the mere characterization of a laser system. It may be used in further research projects in both pulsed and continuous wave systems. The mirror system would effectively function like a compact delay line for pulsed laser systems.

High resolution spectroscopy may also be possible with the use of small motor step sizes. If the narrow band of 50 GHz attributed to the Firefly OPO is insufficient for resolving a thin spectral line, the band could be tuned to enclose the expected line and then the interferometer could extract the absorption lines. The function of the OPO would become effectively like a broad source analogous to that used infrared spectroscopy except in this case it would be for the purpose of high resolutions in the THz regime.

Chapter 3

Continuous Wave and Time Domain Terahertz Spectroscopy[1]

The spectral absorption characteristics of plastic military grade explosives were analyzed using the Firefly-THz continuous wave OPO. Cyclotetramethylene-tetranitramine (HMX), cyclotrimethylene-trinitramine (RDX), and pentaerythritol tetranitrate (PETN) and Composition 4 (C-4) were investigated. These specific explosive samples were chosen because they are some of the most powerful and most common high explosives in use. Even a small amount of such powerful explosives could be used to inflict harm on citizens and social infrastructure. Thus, it is critical that these substances do not pass through security checkpoints undetected. These particular explosives were suspected to have spectral absorption 'fingerprints' at low THz (<3 THz) due to lattice vibrational modes and collective intermolecular motions which would be detectable using the Firefly-THz system. However, due to limitations discussed in the earlier Section 2.3.4, the Firefly OPO system coupled with the Golay cell detection system, was only capable of reading below 1.8 THz frequencies. This prevented conclusive results being drawn on the spectral characteristics of explosives at frequencies higher than 1.8 THz. However, this does not mean that the Firefly system cannot

---

[1] A portion of this chapter has been submitted for publication in *Journal of Infrared, Millimeter, and Terahertz Waves.*

reach the higher frequencies desired. If some mirror alignment calibrations were performed within the cavity, it may be possible to shift the THz frequency output intensity profile to optimize the system for higher THz frequency functionality.

3.1 Explosive Sample Preparation

The explosive samples were supplied by the Edmonton Police Department under the condition that all Federal regulations were followed. The temporary licensing and clearance acquired prevented any tampering with the sample materials themselves. However, there was a freedom to choose the nature in which the explosives were contained. The samples were issued in standardized polystyrene cuvettes commonly used for IR spectroscopy, and also in polyethylene plastic bags in small, 2-3 gram weights. The explosives were in powder form so the particles could move freely within the relatively spacious sample bags. However, the samples were restricted to their pure form. No sample mixing was permitted since this could affect the volatility of the sample. Although these were serious limitations on sample preparation, it served to demonstrate that THz spectroscopy can be performed without any significant sample manipulations. In contrast to some previous studies, there was no sample matrix introduced to dilute the powder, nor was there any specialized treatment such as pelletization to make the radiation absorption more manageable. There were certain advantages to the pure sample approach. Spectroscopy studies in which concentration was diluted by mixing the samples observed matrix effects on terahertz spectra such as peak broadenings and peak shifts [41].

3.2 Methodology for CW Spectroscopy Experiments

The THz output of the Firefly OPO was focussed just in front of a Tydex Golay cell detector using a 90° off axis, gold coated parabolic mirror with a diameter of 2.5”. The explosive samples were placed at the sample target location where the THz beam is focussed, approximately 10 cm from the mirror. The Golay cell was situated directly behind the sample (1 cm away) in order to capture the largest area of transmitted THz radiation (Figure 3.2.0.1). In order to mitigate atmospheric absorption effects of THz radiation, the optical path length between the OPO and the sample was kept as short as possible. There was little to be gained by adding additional optics to the system to focus the beam to the Golay cell after transmission through the sample since the extra beam path distance in the humid air significantly diminishes the signal strength. In order to capture spectroscopic information, the Firefly THz OPO’s narrow band output frequency was incrementally tuned along its entire range of operation by the MgO:LiNbO$_3$ crystal rotation mechanism described in Section 2.1. At each frequency step, the signal from the Golay cell was captured by a digital oscilloscope. It was necessary to briefly stop at each frequency step in order to avoid the associated noise of the internal motor that tunes the OPO and also to allow the system to take sufficient averages to minimize the noise floor. The signal was then uploaded on a computer where the data was processed and integrated using a MATLAB code (Appendix D). Once all the frequencies were scanned and all Golay detected light intensities were recorded, a spectrum was constructed.

The frequency step size interval was variable but was chosen based on the limitations in bandwidth of the OPO. Since the output frequency of the OPO had a narrow band of 50 GHz width, the frequency step interval was set to be a matching 50 GHz as well. As mentioned in the introduction section, the expected spectral signatures were broad so this step size choice minimized redundant data points. Furthermore, it was a decision made in the interest of minimizing scan time. Small step sizes would require more data points to span the entire frequency range. Since the most time consuming process was the uploading of data from the oscilloscope, extra data points would greatly increase scanning time and hence decrease the practicality of such a method for security screenings. Each scan with three averages required approximately two hours. Future iterations of the THz spectrometer could incorporate a direct data acquisition interface between the Golay cell and the computer thus bypassing the need for an oscilloscope completely and improving the scanning time. However, this arrangement including the oscilloscope was best for diagnosing and debugging the system.

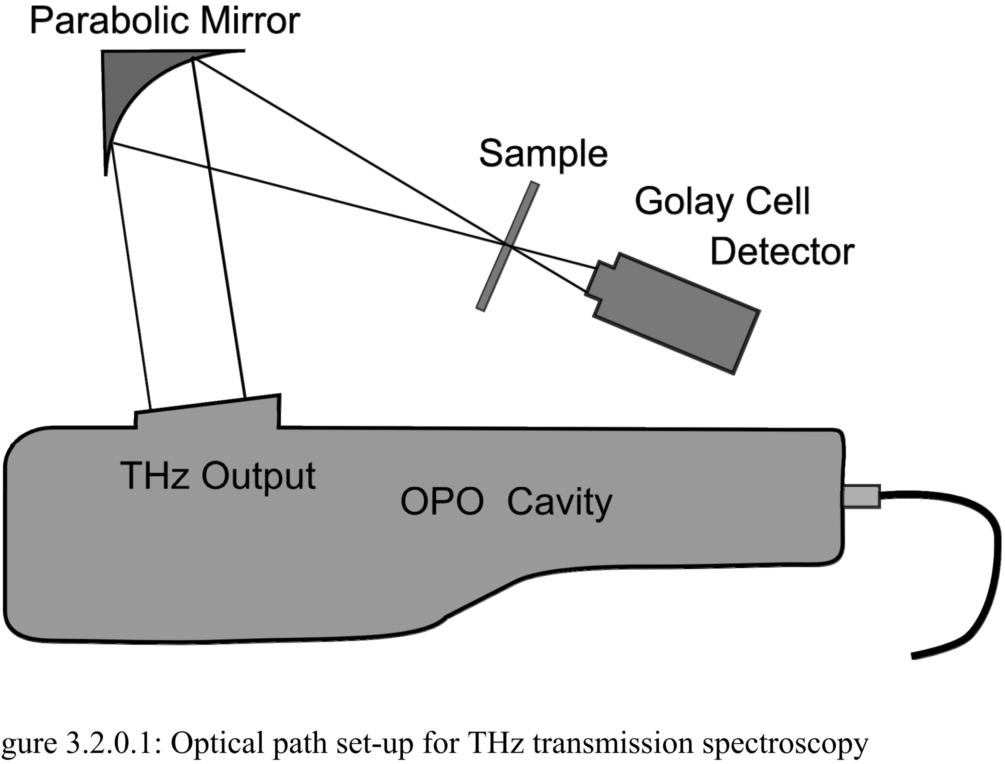

Figure 3.2.0.1: Optical path set-up for THz transmission spectroscopy

The output beam was specified by the manufacturer to be collimated so the focus of the beam was directly at the focus of the parabolic mirror. The sample explosive holder was placed 10 cm from the parabolic mirror which was the parabolic focal point. Before placing the sample cell containing the explosives in the path of the beam, an empty containment bag or cell is placed right in front of the entrance cone to the Golay cell detector in order to establish a reference spectrum. The surface of the containment cell completely eclipsed the Golay collection cone so that all THz waves collected by the Golay cell must first travel through the sample. During the actual scans, the explosive samples were placed exactly where the empty containers were situated. The spectroscopic results were then normalized to the empty container scans in order to eliminate any spectroscopic characteristics or scattering effects of the containment bag itself or any chemicals lining the bag.

It should be noted that a lock-in amplification scheme may also be used for this system in order to minimize the noise contribution from non-THz frequencies. However, these experiments focussed on applicability and viability in “real world” security screenings so a more simplistic approach was taken at these initial spectroscopic studies. Future work may incorporate an optical chopper synchronized with a lock-in amplifier to detect the THz signal.

3.3 Discussion of CW Spectroscopy Results

RDX, HMX, C-4, and PETN explosive samples were tested using the transmission mode spectroscopy method. However, only RDX and C-4 yielded multiple spectral peak signatures. This is potentially due to the limitations of the Firefly OPO itself or the low sensitivity of Golay cell. Spectroscopy at higher THz frequency tunings was difficult since the high THz frequency tuning output power of the Firefly OPO is low. Directing the THz through an absorbing sample material results in a THz signal that is below the noise floor of the Golay cell detector. As mentioned earlier, it was found that the detection scheme using the Firefly THz system coupled with the Golay cell did not produce useful spectra above 1.8 THz frequencies. This limitation was supported by the results in Section 2.3.4. The lamellar mirror interferometer coupled with the Golay cell could not discern Firefly frequency tunings at 1.9 THz and higher. Justified by these observations, the subsequent spectroscopic scans were truncated around 0.65 – 1.9 THz spectral region. Figure 3.3.0.1 shows a summary of the transmission spectroscopy plots for the explosives investigated. These signatures were processed through a MATLAB lowpass butterworth filter in order to minimize noise and smooth out the plots to emphasize the broad spectral characteristics of interest.

Before addressing the explosives spectra in detail, it is important to justify the lower THz frequency limit of tuning range used for spectroscopy. From the plot, it is evident that both HMX and PETN spectra share a distinct absorption characteristic at the low THz extreme of the scan (0.65-0.75 THz). However, the validity of this characteristic is questionable since this region of THz is outside of the Firefly THz calibrated range. Although the tuning motor is capable of tuning angles that produces low THz frequencies, the OPO manufacturer only tested a limited range of THz frequency tunings. Specifically, the manufacturer stated that the Firefly was capable of tuning frequencies between 1.2 to 2.5 THz [68] using default OPO cavity calibration. However, the THz frequency profiling conducted in Section 2.2 (Figure 2.2.0.1) indicated that frequencies below 1.2 exhibit the greatest THz radiation power as detected by a Golay cell detector. Furthermore, in Section 3.2.4, a mirror interferometer was used to characterize the OPO and found that coherent THz radiation was produced at tunings as low as 0.8 THz. However, despite a substantial Golay signal at 0.7 THz, the interferometer was not able to distinguish a THz frequency due to sporadic noise that became prevalent at the low THz tuning extreme. Based on all these factors, there is less confidence in the absorption spectrum that occurs within the range of 0.65 to 0.7 THz. Another motivating factor to disregard this low THz frequency characteristic is that icing sugar, which should be transparent in this frequency range, seems to exhibit the same anomalous step-like absorption characteristic as HMX and PETN indicating that this characteristic is not sample specific. Rather, it is observable for any material. In this thesis, all spectral plots frequencies below 1.2 THz were included regardless of the specified OPO calibration specifications in order to present a complete picture of the THz emission from the Firefly and also to include the important sub 1.2 THz spectral peak characteristics of RDX discussed later in this chapter.

As seen in Figure 3.3.0.1, the spectral peak observed from HMX was broad and centered about 1.45 THz. PETN also exhibited a broad spectral peak at approximately 1.78 THz, located near the upper limit of the scanning range. As discussed in the introduction (Section 1.2), Liu [39] found that HMX and PETN explosives have spectral peaks occurring at 1.78 and 2.0 THz, respectively. However, Tribe [37] found these spectral peaks to be 1.58 and 1.73 THz, respectively. The spectral peaks observed in this thesis are compared to the peaks observed by Tribe and Liu in Table 3.3.0.1. The THz peaks for HMX and PETN observed in this project are 1.45 and 1.78 THz which closely compare to results found by Tribe but not Liu. However, the RDX spectrum observed in this thesis closely matched the results obtained by Liu, not Tribe. This suggests that explosives spectra are dependent on the specific manufacturer of the explosive. There may be subtle differences between explosives depending on the purity, moisture content and filler. One way to confirm this would be to acquire the same type of explosives samples from various sources and compare the spectra.

Icing sugar was used for comparison as a non-explosive control material. The general spectral shape of the icing sugar closely resembled that of the HMX sample (Figure 3.3.0.1). The center spectral peak of icing sugar was 1.40 THz which is relatively close to the 1.45 THz peak observed for HMX, especially considering the broad characteristics of the spectra. These results suggest that the Firefly and Golay cell detection system used here may not be suitable for detecting HMX. During a regimented security screening, HMX may not be distinguishable from icing sugar using the Firefly within the current frequency range limitations. Furthermore, a single spectral absorption peak may not be sufficient for reliable spectroscopic explosives identification even if there are no materials with close spectral characteristics that could cause false alarms. The same concern applies to PETN since it only displays one spectral peak in this region as well. However, as mentioned earlier, it may be possible to modify and calibrate the Firefly OPO cavity to shift the THz frequency range slightly such that the system is able to detect a wider selection of explosives. With subtle adjustments of the cavity mirrors, the region of the MgO:LiNbO$_3$ crystal where the pump, probe and signal beams intersect may be aligned to output higher THz power at a specific crystal angle which corresponds to a specific THz frequency tuning.

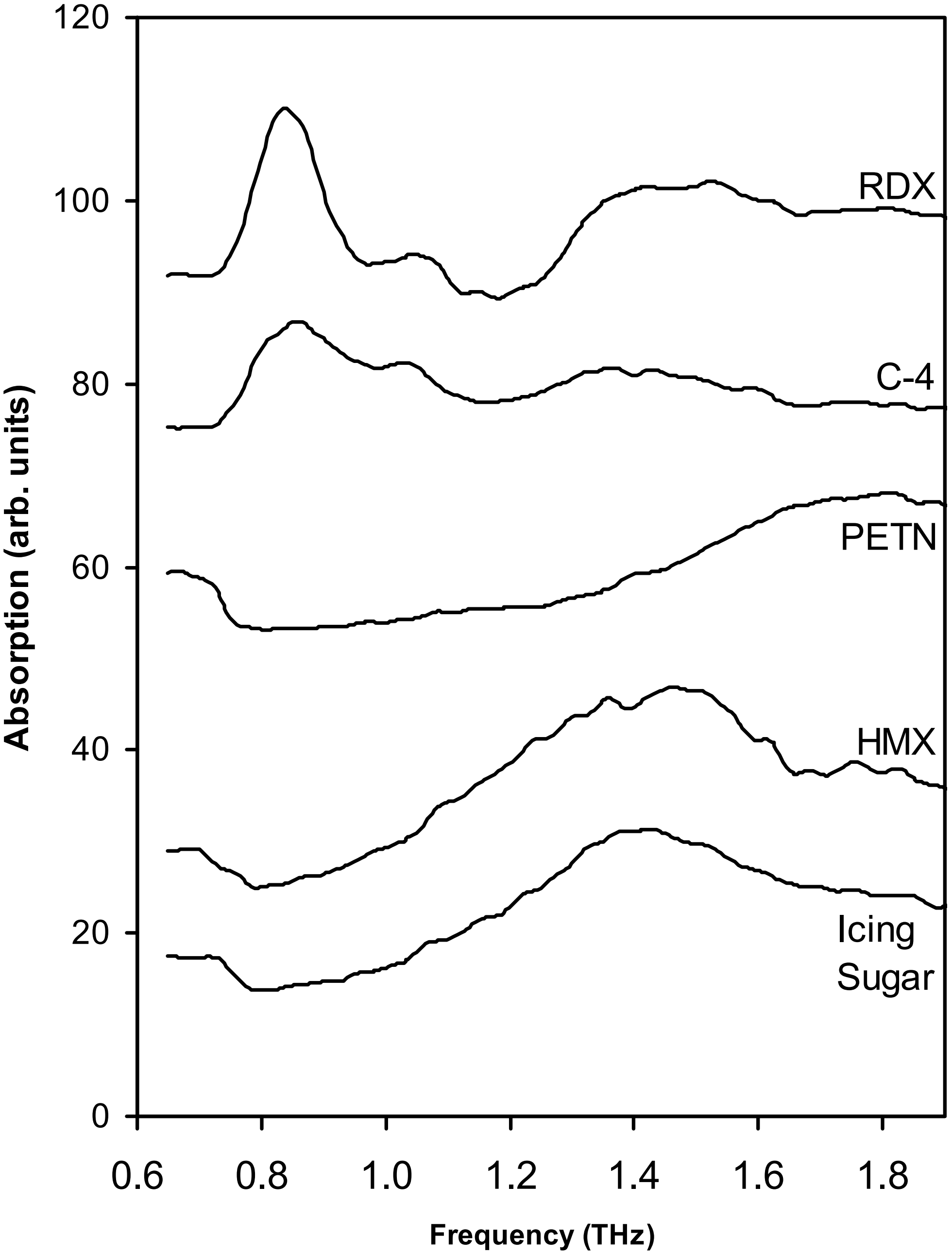

Figure 3.3.0.1: Summary of transmission spectroscopy on explosives. The substances included in order of appearance from the top of the plot are: cyclotrimethylene-trinitramine (RDX), Composition 4 (C-4), pentaerythritol tetranitrate (PETN), cyclotetramethylene-tetranitramine (HMX), and icing sugar.

Explosive Compound	Experimental spectral peaks (THz)	Spectral peaks from Lui [39] (THz)	Spectral peaks from Tribe [37] (THz)
RDX	0.83, 1.04 , 1.51	0.82, 1.05, 1.50, 1.96, 2.20, 3.08	0.72, 1.26, 1.73
HMX	1.45	1.78, 2.51, 2.82	1.58, 1.91, 2.21, 2.57
PETN	1.78	2.0, 2.84	1.73, 2.51

Table 3.3.0.1**:** Absorption spectral peaks found in spectroscopic experiments performed in this work compared to the peaks that are expected from previous THz spectroscopic studies [37, 39].

Compared to HMX and PETN, RDX and C-4 had denser and more interesting spectral characteristics. In Figure 3.3.0.1, RDX and C-4 are shown to display somewhat similar spectra, only differing in spectral peak intensity and slight central frequency offsets. A closer view of the RDX compared to the C-4 spectrum is shown in Figure 3.3.0.2. The RDX absorption peaks of 0.83, 1.04 and 1.51 THz evident in the Figures and listed in Table 3.3.0.1 were quantified by identifying the local maxima of the spectra. C-4 exhibited peaks of 0.85, 1.02 and 1.37. The similarities between the spectrum were expected since typical C-4 samples have a 91% RDX content while the remaining 10% consists of plastic binders, plasticizers and, odorizing taggant chemicals [78]. The slight shifts in spectral peaks in 0.85 and 1.02 THz regions in C-4 could be attributed to matrix effects discussed in Section 1.3.6.1. Since THz probes the collective intermolecular motions of solid phase explosives, any impurity molecules such as plasticizers and binders, could cause changes to the THz spectrum. The RDX molecules within C-4 would interact with the impurity molecules so the collective vibrations are affected and thus the frequency absorptions become shifted.

A more significant deviation between C-4 and RDX spectra is that C-4 did not share the 1.51 THz spectral peak found in the RDX spectrum. Although the general shape of the C-4 spectral peak resembled that of RDX, it appeared reduced and downshifted in frequency to 1.37 THz. Given this difference between RDX and C-4, it may be possible to clearly distinguish these substances despite C-4 being primarily composed from RDX. However, it should be noted that the fillers in C-4 were strongly absorbing of the Firefly THz radiation. It was necessary to thin the C-4 as much as possible so that THz radiation would propagate through the sample. It is conceivable that the transmitted THz signal through C-4 drops below the Golay limit of detection before the tuning reaches 1.9 THz. If this is the case, there may indeed be a C-4 spectral peak at approximately 1.5 THz that cannot be resolved. Further studies with higher power THz signals could confirm the higher THz frequency spectral peak observed here.

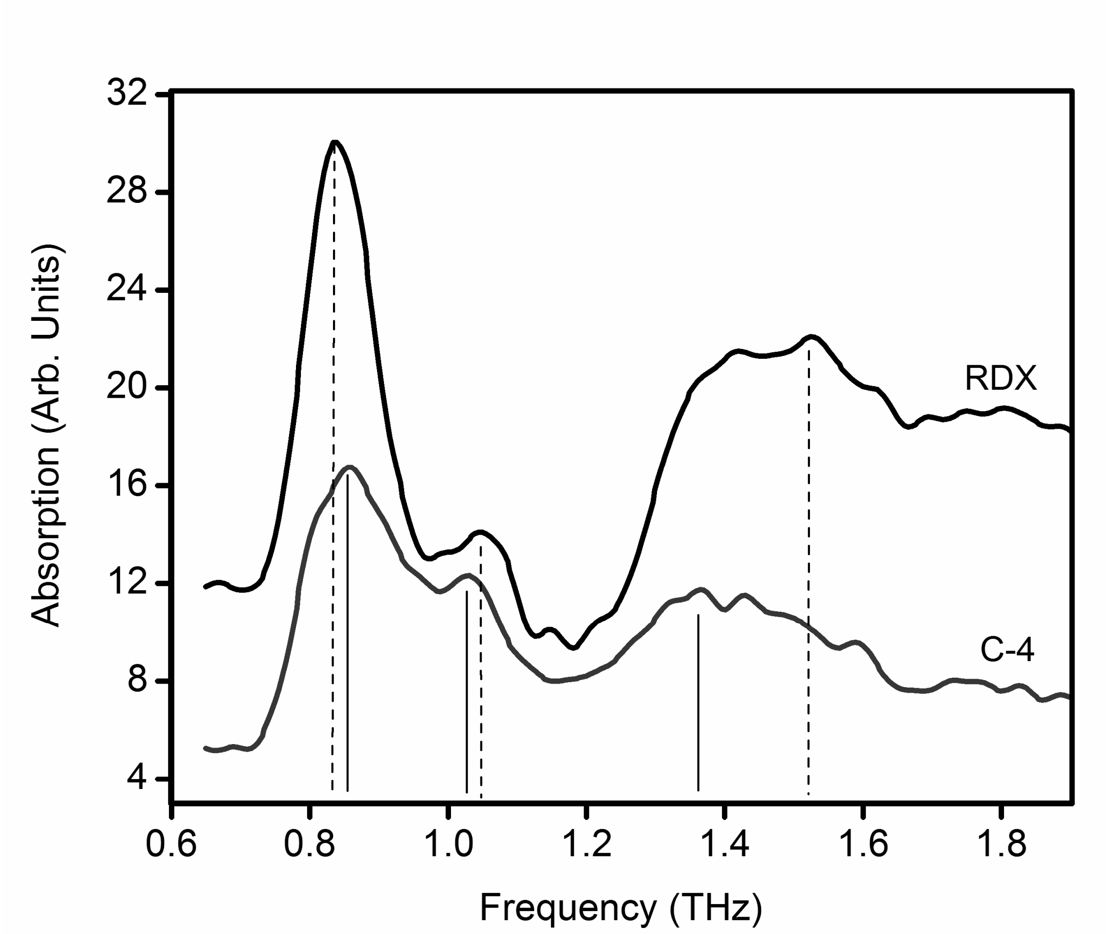

Figure 3.3.0.2: Comparison of cyclotrimethylene-trinitramine (RDX) spectrum to the Composition-4 (C-4) spectrum. RDX spectral peaks are 0.83, 1.04, 1.51 THz indicated by the vertical dotted lines. C-4 spectral peaks are 0.85, 1.02 and 1.37 THz indicated by the vertical solid lines.

3.4 Origin Software Lorentzian Algorithm

Motivated by the prospect of eventually automating the explosives detection procedure for all security screenings, commercial software was used to detect the absorption peaks using a Lorentz function fit algorithm. If this approach proves to be successful, the human element of error may be greatly reduced in explosives detection scenarios. The software used for this purpose was the “Origin” graphing and data analysis software suite [79]. The Lorentz lineshape function used by Origin software is defined as:

$$L(v) = L_0 + \frac{2\beta}{\pi} \frac{\gamma}{4(v - v_0)^2 + \gamma^2} \qquad (3.4.0.1)$$

Where L_0 is the axis offset, β is a multiplicative factor that affects the amplitude of the function, v_0 is the center frequency of the function, and γ represents the full width half maximum (FWHM) of the Lorentz lineshape function.

The basic procedure of a Lorentzian fit involves the superposition of several Lorentzian curves over the measured spectrum. The fit algorithm attempts to replicate the curves of the spectrum as accurately as possible by summing the combination of Lorentz lineshape functions. The Lorentz lineshape function in particular was selected because it effectively represents the inherent symmetrical broadening of spectral absorption peaks. Any peak characteristic, like sharpness, width and amplitude, can usually be represented by simply changing the coefficients in the Lorentz equation or adding extra Lorentz lineshape functions to the fit algorithm.

The spectrum of RDX was uploaded to the software interface and a multipeak Lorentzian fit was performed. The RDX spectrum best illustrates the utility of the Lorentz fit approach. Figure 3.4.0.1 and Figure 3.4.0.2 show how the spectral peaks of RDX were separated and analyzed using the Origin algorithm. Spectral peaks found by the Lorentzian algorithm do not precisely match the peaks that were attained by simply computing the local maxima. Table 3.4.0.2 summarizes the spectral peak values, full width half maximum, and the coefficient of determination derived by the Lorentz fit algorithm. This table also includes a comparison of the spectral peaks found by merely observing the local maxima peaks. In Figure 3.4.0.2(a) the Lorentz function suggests the spectral peak to exist at 0.84 THz while the observable peak is closer to 0.83 THz. This slight discrepancy is due to the slight asymmetry of the spectral data peak. Although it is possible that this asymmetry could be caused by another spectral absorption peak that is obscured by the 0.83 THz peak, but it is most likely that this asymmetry is due to noise effects that occurred during the data acquisition. The noise is no longer visible in the plots due to the low pass filtering used to smooth the plots. However the asymmetry may have remained as an artefact of the noise. A similar discrepancy was evident for the spectral region shown in Figure 5 (b). The local maximum spectral peak was found to be 1.04 THz while the Lorentz fit indicated a 1.05 THz spectral peak. In the 1.2 - 1.9 THz frequency range depicted in Figure 5(c), the Lorentz algorithm most accurately fit the data using three spectral peaks of 1.36, 1.52, and 1.81 THz rather than with a single peak as determined by Liu et al. and Tribe et al. It is not certain if these peaks are real vibrational modes or merely artefacts of noise attributed to the Golay detection method.

The Lorentz lineshape function fit algorithm presents a more reliable method for detecting spectral peaks than mere visual inspection or local maxima determination. Not only does this method accurately determine the spectral peaks, it also provides additional numerical criteria with which to determine the spectral signature. For example, the full width half maximum estimations within a cluster of spectral peaks may not be easily assessed visually; however, the Lorentz lineshape function fit provides this value as coefficients to the constituent equations. In a security screening, these coefficients can be referenced to tabulated values (similar to Table 3.4.0.2) and used to efficiently assess the chemical compositions of materials. This method is particularly useful for solid phase spectroscopy in the THz regime since there is a great amount spectral peak overlap due to the broad characteristics of the signatures.

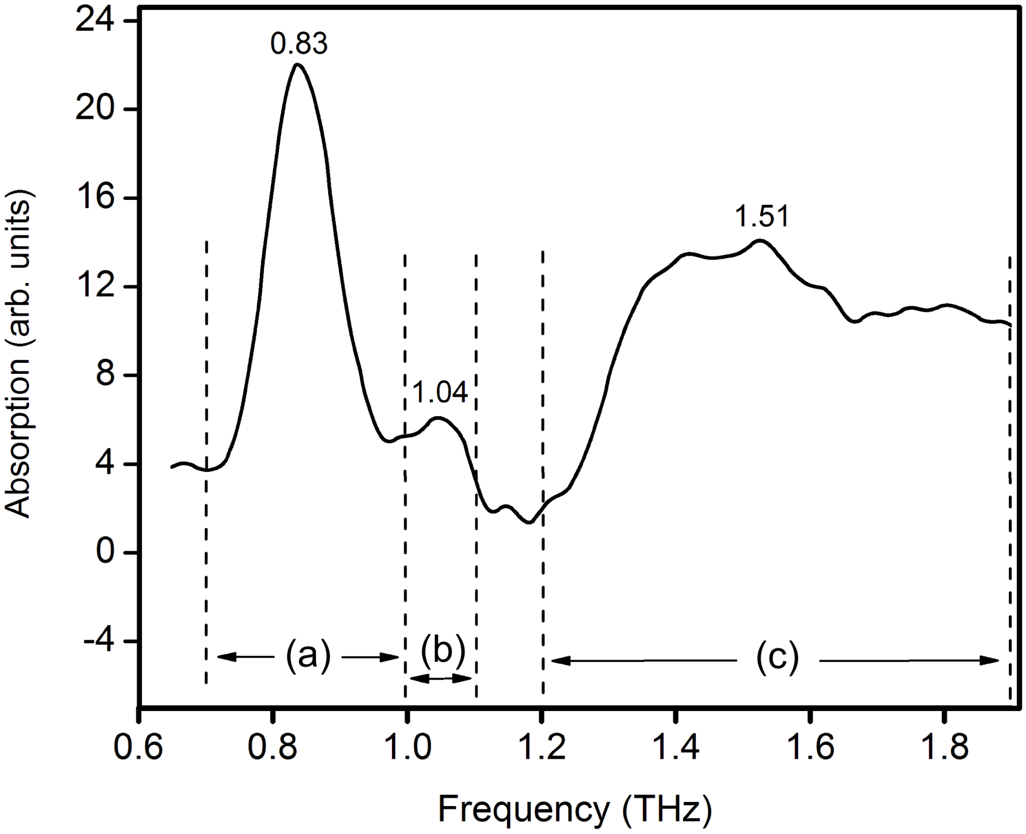

Figure 3.4.0.1: Cyclotrimethylene-trinitramine (RDX) THz absorption spectrum. Notations (a), (b) and (c) represent the segmentation of the plot for Lorentz function analysis shown in Figure 3.4.0.2. Local maxima are annotated at the spectral peaks.

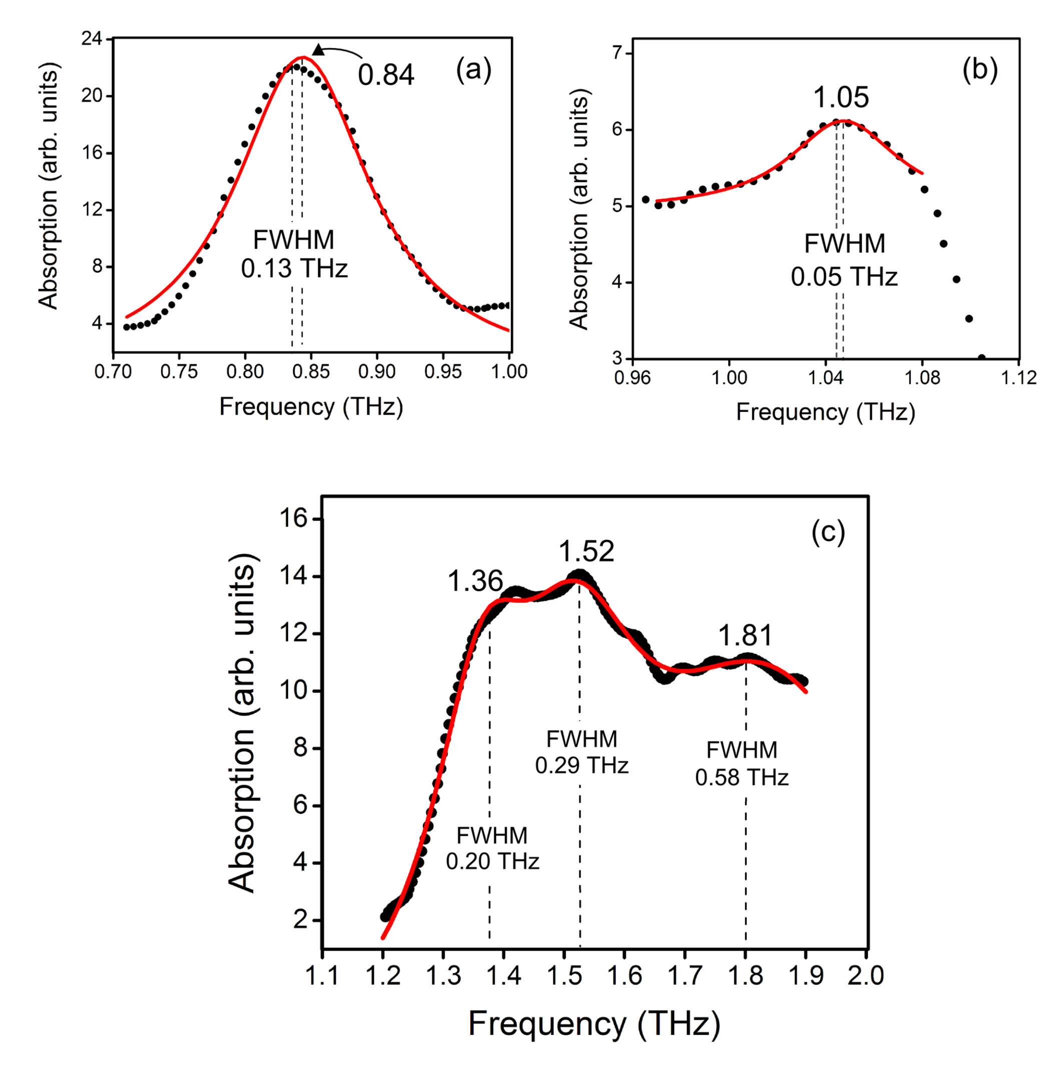

Figure 3.4.0.2: Isolated regions of the cyclotrimethylene-trinitramine (RDX) spectrum with Lorentzian fit analysis. Dots represent the spectrum data points. The solid line represents the Lorentz lineshape function fit. (a) is the 0.7 – 1.0 THz region (b) is the 1.0 – 1.2 THz region, (c) is the 1.2 – 1.9 THz region as indicated in Figure 3.4.0.1. The plots are annotated with the computed Lorentz fit peaks and their respective full width half maximum (FWHM) values.

Explosive Compound	Local maximum spectral peaks (THz)	Lorentz function fit of spectral peaks (THz)	FWHM (THz)	Coefficient of Determination (R^2)
RDX	0.83	0.84	0.13	0.98
	1.04	1.05	0.05	0.94
		1.36	0.20	0.99
	1.51	1.52	0.29	0.99
		1.81	0.58	0.99
HMX	1.45	1.43	0.83	0.98
Icing Sugar	1.40	1.44	0.67	0.99
PETN	1.78	1.78	0.80	0.99
C-4	0.85	0.85	0.17	0.98
	1.02	1.02	0.17	
	1.37	1.38	0.38	

Table 3.4.0.2: Lorentz fit algorithm (Origin software) peak values and FWHM values for each explosive compared to the spectral peaks obtained by observing the local maximum spectral peak values.

In addition to RDX, the spectrum of Composition 4 (C-4) was also processed by the Lorentz fit algorithm. The result of the computation is shown in Figure 3.4.0.3. The exact values of spectral peaks and FWHM are shown in Table 3.4.0.2. The peaks found by the Lorentz fit matched closely to the local maxima peaks. Only one Lorentz lineshape function was used to approximate the 1.38 THz region spectral peak.

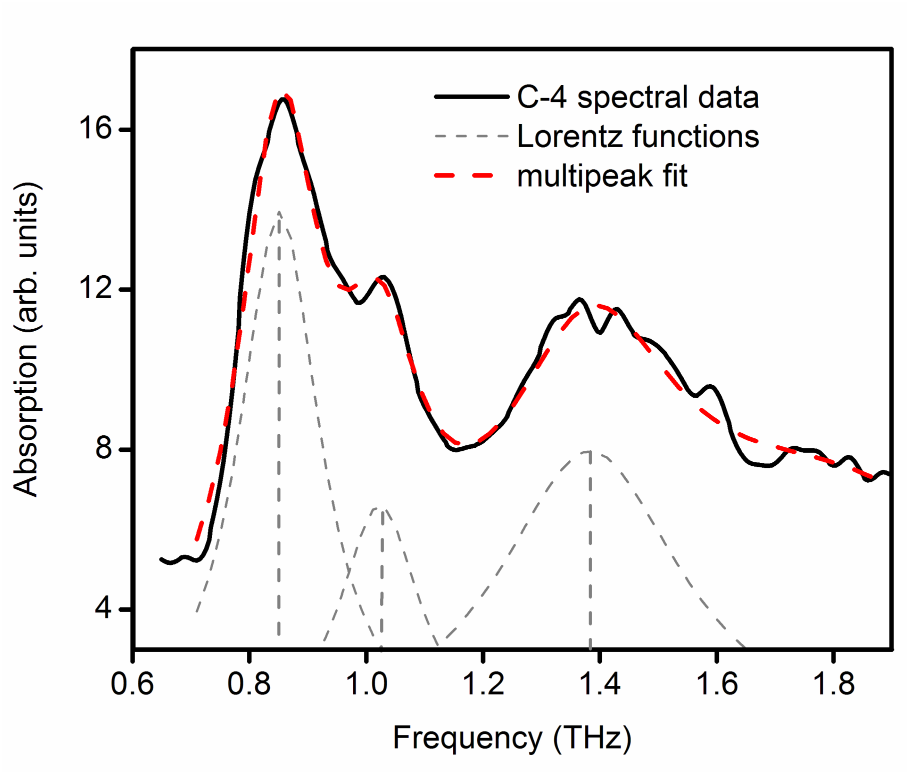

Figure 3.4.0.3: Plot of Lorentzian fit algorithm performed on the Composition 4 (C-4) absorption spectrum. Grey dashed lines represent individual Lorentz lineshape functions with their central peaks annotated on the plot. The red dashed line represents the superimposed resultant fit. The solid line is the original spectrum. The spectral peaks as computed by the Origin are: 0.85, 1.02, 1.38 THz. (see Table 3.4.0.2)

The broad spectral signatures of explosives similar to those exhibited by HMX and PETN spectra, shown in Figure 3.4.0.4, could benefit most from the application of the Lorentz fit algorithm. In Figure 3.4.0.4, the utility of the method is apparent by how successfully the spectral peak broadening effect can be quantified using the FWHM coefficient of the generated Lorentz lineshape function. In Figure 3.4.0.4 (a), the THz spectrum of HMX is compared to that of icing sugar. The HMX peak determined by the Lorentz function was 1.43 THz which is similar to the Lorentz function spectral peak for icing sugar at 1.44 THz. However, the FWHM of HMX was 0.83 THz while icing sugar had a FWHM of

0.67 THz. Using both, spectral peak and FWHM tabulated values together; HMX can be distinguished from icing sugar. If only local maximum peak values are available, the result would remain inconclusive.

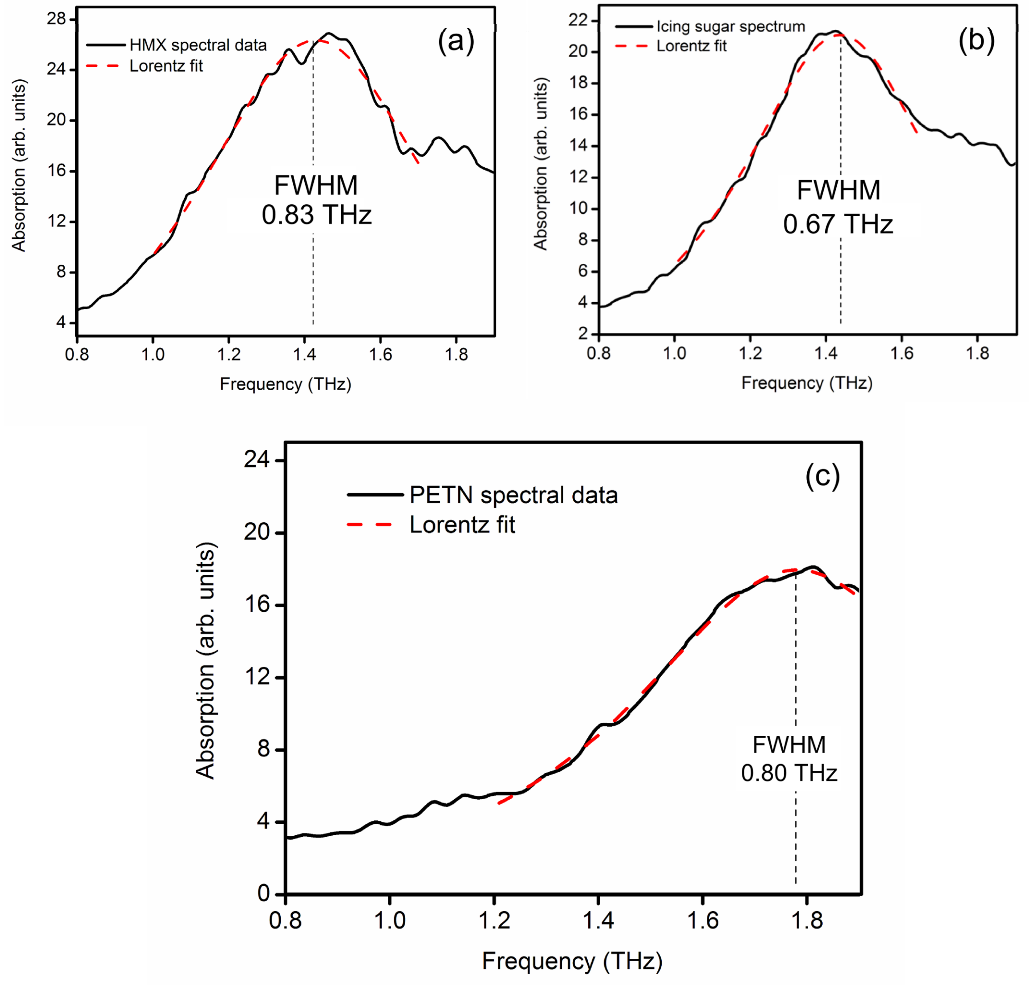

Figure 3.4.0.4: Absorption curves of (a) cyclotetramethylene-tetranitramine (HMX) compared to (b) icing sugar and (c) pentaerythritol tetranitrate (PETN) with superimposed Lorentz fit functions. The peaks for HMX and icing sugar are similar when found by the Lorentz lineshape function as 1.43 and 1.44 THz respectively. However, the linewidth of HMX is 0.83THz while icing sugar has a 0.67 THz linewidth as determined by FWHM of the Lorentz function. PETN (c) exhibits a 1.78 THz spectral peak and 0.80 THz FWHM linewidth.

3.5 Threshold of Thickness for Explosives Detection

In order to determine the limitations on detectability of the explosives samples, THz transmission experiments were performed through sample explosives of various thicknesses. A variable thickness sample holder was assembled in order to make repeatable and quantifiable measurements of material thickness that the THz beam must pass through. Two polystyrene plates of 0.8 mm thickness were pressed together to sandwich the explosive within the bag so as to create a uniform sample thickness throughout the area of the sample where the THz beamwaist passes through. Two screws on either side of the target region maintained the plate separation. In order to vary the thicknesses of the sample, the bags were simply shaken or perturbed in such a way that the powder particles redistribute to cover a larger area with thinner profile or a smaller area with a thicker profile.

3.5.1 Discussion of Threshold Experiments

Using the polystyrene plates to accurately vary the thickness of sample the THz beam must pass, it was possible to determine the sample specific limitations for detection as well as suggest a methodology for spectroscopic trials to be used in practice. The general thickness-detectability relationship for all the samples was intuitive. Figure 3.5.1.1 shows the spectrum of RDX with various thicknesses. Samples prepared too thick (0.96mm, 1.81mm) would block the entirety of the THz intensity across all frequencies. This blockage may not be entirely due to resonant absorption but also due to scattering and reflection. No spectral information can be extracted from such a trial since the scan would simply yield the original OPO output spectrum. Characteristic spectral peaks of the sample would not be significant or telling of the true spectrum of RDX. At the other extreme, samples prepared too thin would simply yield a blank spectral plot. Almost all of the incident THz radiation would pass through the sample cells unhindered. Certainly, some of the THz must interact and be absorbed, but if the sample is prepared too thin, there is not enough sample material propagation for the THz to experience any noticeable absorption. However, samples of thickness measurements between 0.32 mm and 0.82 mm seem to have a very similar general spectral trend that agrees with previous scans. The 0.8 THz and 1.5 THz frequency region peaks are generally visible, although slightly distorted.

The results shown in the plot suggest that a methodology should be adopted for transmission scanning which takes into consideration the sample thickness effects. There should be a criterion for how large or small the absorption coefficient may be such that the data can be considered valid. If the coefficient is too large, the sample likely absorbed too much of the THz signal, if it is too small, not enough of the THz signal interacted with the sample. This criterion would ensure that each sample was of a proper thickness such that the spectrum results are resolvable across the tuning range. The RDX threshold plot (Figure 3.5.1.1) suggests that an average absorption ratio of between 3 and 9 (arb. units) across the spectrum should yield reliable results for spectroscopic scans.

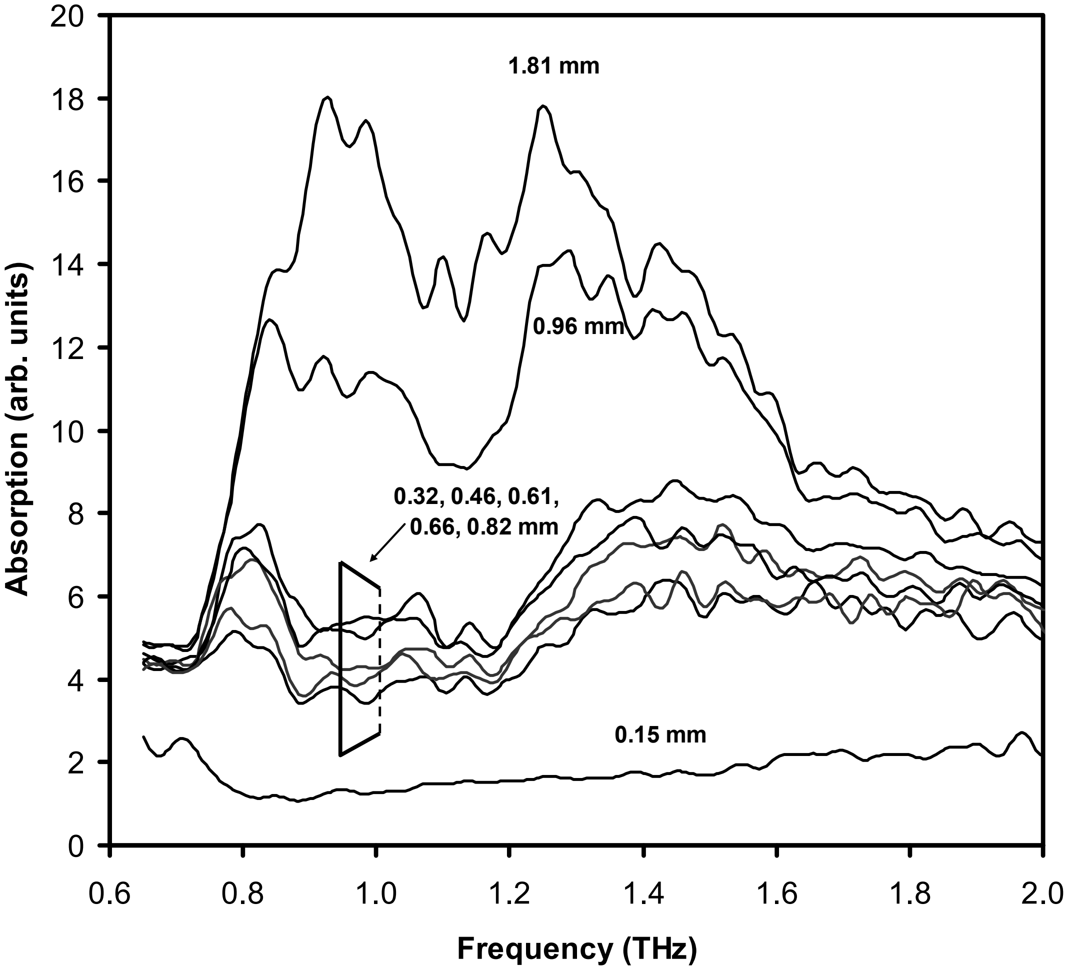

Figure 3.5.1.1: Threshold of detection for RDX samples. The plot shows the absorption spectrums of RDX samples of various thicknesses. If a sample is made too thick (1.81mm), the absorption spectrum resembles that of the Firefly OPO output spectrum since all the radiation is absorbed by the sample. If the sample is too thin (0.15mm), all the THz passes directly to the Golay cell and the absorption coefficient becomes approximately unity.

Similar threshold trials were performed with the other available explosive samples. The coefficient criteria mentioned earlier was similar for all samples. Figure 3.5.1.2 shows a summary of all plots together using sample thicknesses that fit the criteria for valid transmission spectroscopy. Note that when comparing this plot to the Figure 3.3.0.1, it is evident that the polystyrene sandwiching plates add distortion to the spectrum. This distortion is evident as fluctuations in intensity across the frequency spectrum. The amplitude of the 0.83 region spectral peak in RDX is nearly halved when compared to the Figure 3.3.0.1. The 1.3 THz spectral peak in C-4 is no longer distinguishable in relation to the noise fluctuations. Apparently, although the polystyrene plates were transparent to THz, they still contributed to increased reflection and scattering effects. It may be possible that there occurs a significant amount of internal reflection due to the index of refraction change from explosive sample to polystyrene. If the reflected THz waveform fits within the separation distance between the plates by an integer multiple of half wavelengths, constructive or destructive interference could occur. This would explain the undulating nature of the spectra in Figure 3.5.1.2. Polystyrene absorption and scattering may be minimized if the plates were fabricated to be thinner. However, this may also increase the tensile bending of the plates and decrease the uniformity of the samples. Another possible contributing factor to the distortion observed may be the diffusivity of the surface of polystyrene due to minute scratches and imperfections. These may be minimized if higher quality machined polystyrene material was used instead of standard commercial plates.

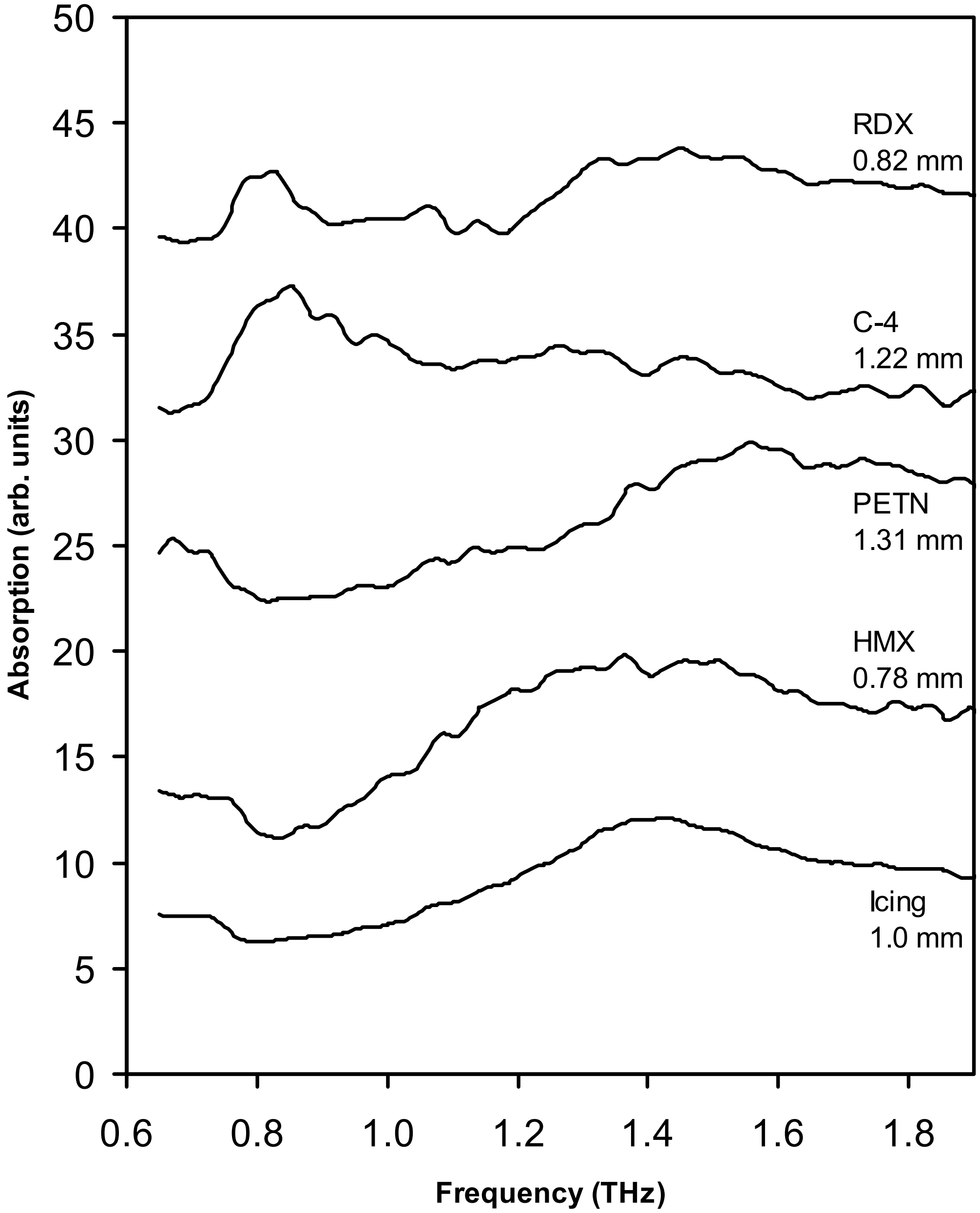

Figure 3.5.1.2: Spectra of explosives samples sandwiched between polystyrene plates. The thicknesses of the samples were selected to be within the criteria of validity.

3.6 Concealed Explosives Spectroscopy

Terahertz spectroscopy has its major appeal stemming from the fact that THz radiation can transmit through most dielectric materials with its spectral power intact. Therefore, spectroscopy can also be performed on materials while they are hidden or concealed behind a dielectric. This would be particularly useful in security checkpoints since there is often a high throughput of packages and luggage. It requires an unreasonable effort to open each package in order to scan the contents for potentially dangerous substances. THz spectroscopy potentially presents a method for scanning inside packages non-invasively and non-destructively.

To test the Firefly OPO system in its capability to detect concealed explosives, various materials were used to obscure the THz output beam before it contacted the explosives samples. The optical set-up was identical to that of the transmission spectroscopy described in the previous Section (Figure 3.2.0.1) except that a dielectric obstruction was placed just in front of the sample. RDX was hidden in an envelope as if in a letter bomb or a package, and covered by fabric as if hidden under an article of clothing. If the obscuring dielectric was not too thick, a clean spectrum could be detected. Figure 3.6.0.1 shows some of these results and compares them to the spectrum of the unobstructed RDX. The envelope, rayon fabric and microfiber cloth obstructions all resulted in similar spectral plots. In order to make each spectrum convenient to read, the plots were offset by 2 arbitrary absorption units. In actuality, the plots of all three spectra overlap. By inspecting the local maxima of the spectra it appears that the 0.83 THz absorption peak of RDX shifts slightly to 0.88 THz and the 1.5 THz absorption peak is largely attenuated. This high frequency attenuation may be due to material scattering rather than absorption that correspond to any molecular vibrations. This was discussed in Section 1.3.6.8. High frequency components are more susceptible to scattering since the material becomes “optically dense” at higher frequencies [66]. Furthermore, the higher frequency output of the OPO is significantly weaker than the lower frequencies. The noise floor of the Golay cell may overwhelm the signal in the high frequency region as it is attenuated by dielectric obstructions. The frequency shift observed from 0.83 THz to 0.88 THz once the RDX is concealed can be attributed to the limited THz radiation power at the low extreme of the tuning range. The frequency emission profile of the Firefly is just on an upward slope in the 0.8 THz region. Although dielectrics have minimal spectral characteristics in the THz regime, radiation that is directed through any dielectric material will be slightly scattered. Assuming the entire THz radiation profile is evenly attenuated by an obstruction, since the Golay cell noise floor remains constant, the usable THz frequencies at the lower extreme (on the upward slope of the frequency profile) become attenuated below the detectability limit. As a result, the true spectral peak in the 0.8 THz region is cut off. Therefore, the observed spectral peak appears slightly shifted toward 0.88 THz.

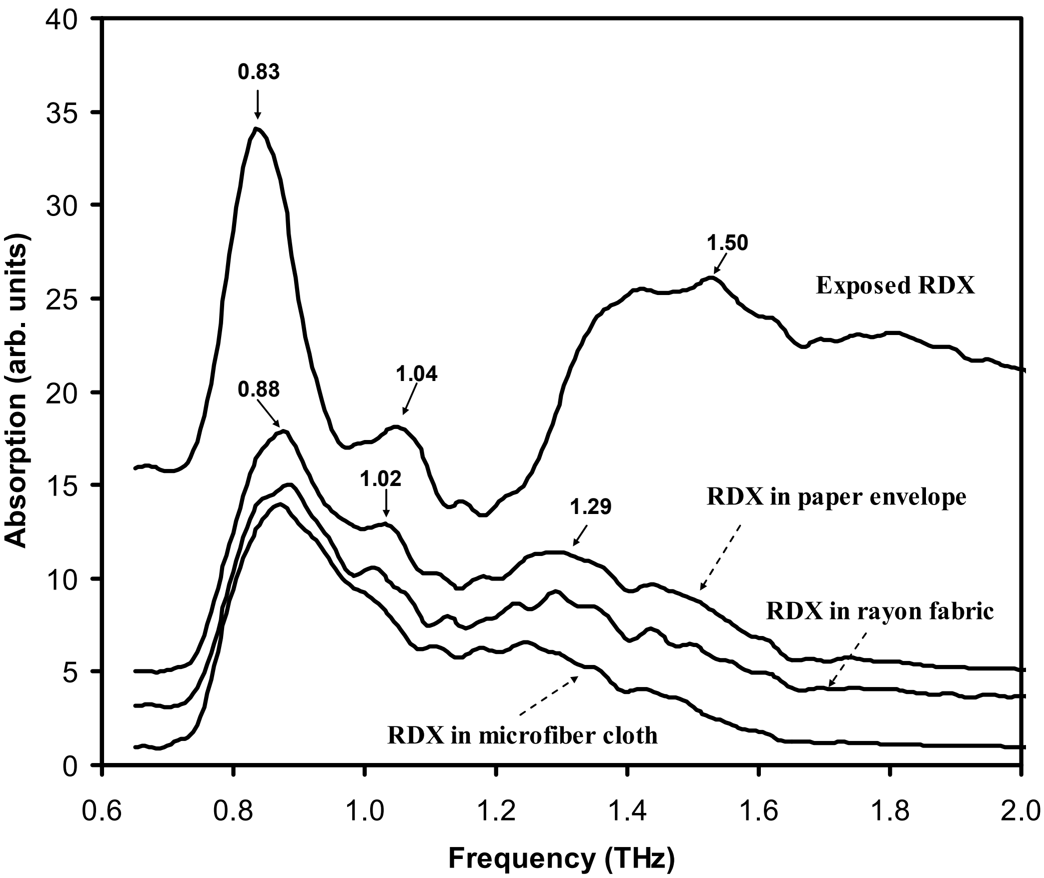

Figure 3.6.0.1**:** Concealed cyclotrimethylene-trinitramine (RDX) spectroscopy. The various dielectric obstructions are compared to the unobstructed RDX spectrum. The rayon fabric spectrum is offset by two arbitrary units and the paper envelope spectrum is offset by four for clarity.

3.7 Continuous Wave Terahertz Radiation Imaging

The major motivation for using THz for security screenings is the prospect that THz spectroscopy can be implemented in concert with THz imaging. This further promotes the Firefly OPO as an attractive alternative to conventional security screening technologies. Not only can the Firefly be used to take spectroscopic scans of luggage, packages, it can be used to take images of these packages and even perform full body image scans of people as they enter a secured area.

To demonstrate the THz firefly capability to image inside of packages and through other obstructions, a simple set-up was constructed similar to the transmission spectroscopy experiments set up (Figure 3.2.0.1). A motorized 2D translation stage was placed in front of the Golay cell instead of a sample holder for explosives. The THz radiation beam was focussed on the target's translation stage using a parabolic mirror. The first sample to be imaged was a small (2.5cm span) "A" made from tinfoil and place inside a 2cm thick Styrofoam slab. The Firefly THz system was tuned to 1.0 THz frequency since it was a relatively high intensity and the beam was set to transmit through the Styrofoam slab. The image was formed by raster scanning the Styrofoam slab with respect to the focused beam. The slab was positioned such that the beam would penetrate the corner of the slab first. Then an intensity measurement was taken by the Golay cell. The motor was then moved in the x-direction by 1 mm increments, taking Golay cell measurements at each step. Once the opposite edge of the slab was reached, the stage was moved in the y-direction by a 1 mm increment and the x-direction translation was reset to its position of origin. This process was repeated until the entire image was formed (Figure 3.7.0.1). The image underwent some basic interpolation processing in order to add clarity, improve the resolution, and define the edges of the object. Still, the result turned out to be "cloudy" and slightly lopsided. This cloudiness could be an effect of the particular processing used. The lopsidedness of the "A" may have been caused by a slight drift in the translation stage or a slight shift in the sample over time due to vibrations of the motor during the scan.

It was found that the spacing of 1mm is the limit of resolution for the optical set-up. Smaller “A” shapes were imaged, but the hole within the “A” could not be resolved if the height of the triangular hole was smaller than 1 mm. The diffraction limit of 1 THz is approximately a 0.3 mm diameter spot size so this resolution was not unreasonable considering focusing optics consisted of a single parabolic mirror.

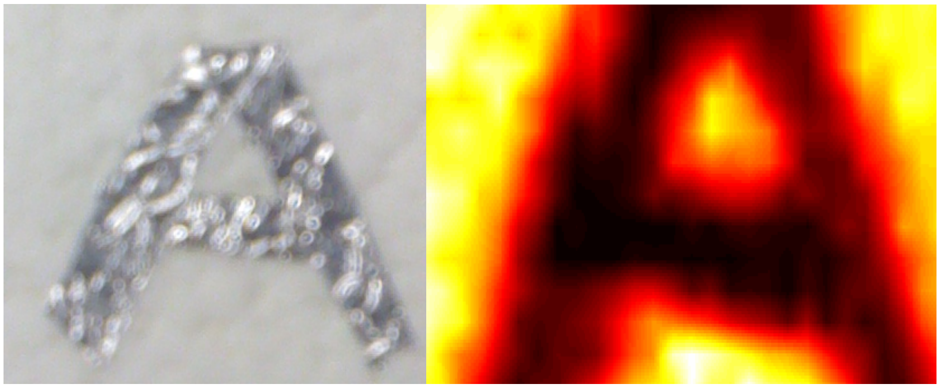

Figure 3.7.0.1: On the left is a photograph of the “A” shaped out of tinfoil to be imaged with THz frequencies. On the right is the raster scan THz image of an “A” shaped tinfoil concealed by a 2 cm thick slab of Styrofoam. The width of the “A” is approximately 2.5 cm. The scan resolution was in 1 mm step intervals.

Another image was taken using the THz system to view a metal paperclip within an envelope. The same procedure was used as for the tinfoil “A” image. The paperclip had to be re-bent to 1.6 cm width to fit into the small scan range of the translation stage. The resulting image is shown in Figure 3.7.0.2. At the curved regions of the image, aliasing is evident as abrupt steps forming the curve.

This is due to the low resolution of the image. Smaller translation intervals may improve upon the curved portions of the image.

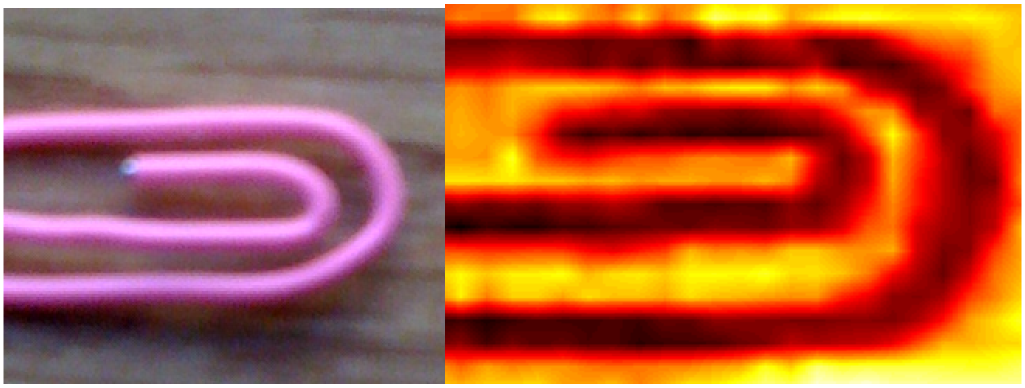

Figure 3.7.0.2: A photograph of a paperclip used for THz frequency imaging is shown on the left. On the right is the THz transmission image taken of the paperclip within a paper envelope. The clip was reshaped to a width of 15 mm in order to fit into the span of the translation stage. The angular appearance of the THz image may be attributed to the 1 mm resolution of the raster scan. Square pixels were smoothed through image processing.

Imaging and spectroscopy can be utilized simultaneously using the Firefly-THz OPO by scanning an object at multiple frequencies. The image contrast at specific frequencies could indicate the nature of the material within a package. To demonstrate this, a 1 cm triangle of RDX powder was imaged within an envelope at three frequencies: 0.90, 0.83 and 0.77 THz. These three frequencies were chosen since they trace out most distinct characteristic spectral peak of RDX at 0.83 THz. The results of the images were normalized against an empty envelope scan at each respective frequency. The results are images shown in Figure 3.7.0.3. By visual inspection, it is clear that at 0.83 THz, the triangle of RDX is most strongly absorbed. The 0.90 THz image resolves the triangular shape the absorption is not as strong. Figure 3.7.0.4 shows a profile of the absorption for each of the frequencies with respect to x-direction translation. The plot is essentially of vertical slice of the previous Figure 3.7.0.3 to illustrate, quantitatively, the difference in absorption. The 0.83 THz absorption coefficient at the peak absorption location (x=14 mm) can be quantified in Figure 3.7.0.4 as 3.7 times as great as the 0.77 and 0.90 THz absorptions.

If this method of imaging was employed in security checkpoints, it may be possible to scan packages for specific explosives using only several key frequency tunings about an expected spectral peak while, simultaneously, imaging for concealed weapons.

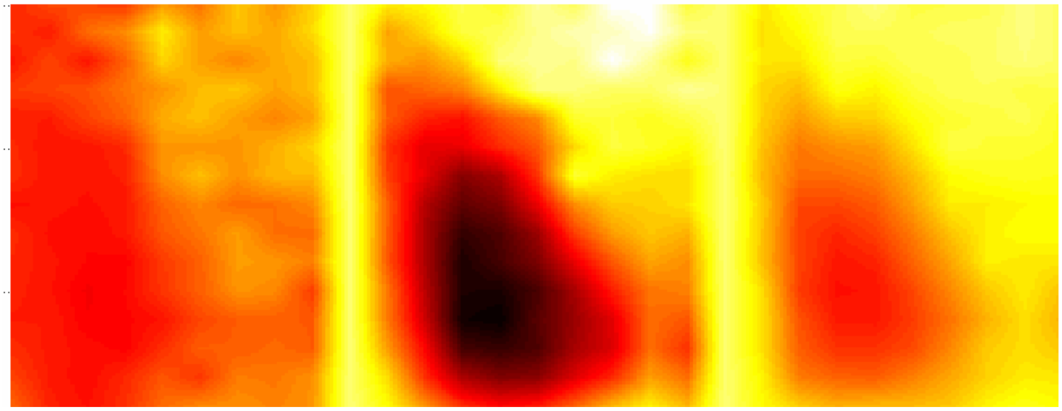

0.77 THz **0.83THz** **0.90 THz**

Figure 3.7.0.3: Images of a triangle of cyclotrimethylene-trinitramine (RDX) explosive concealed within an envelope. Three images are shown using Firefly tuning frequencies of 0.77, 0.83 and 0.90 THz. The highest ratio of absorption in the explosive sample region occurs when transmitting the 0.83 THz frequency.

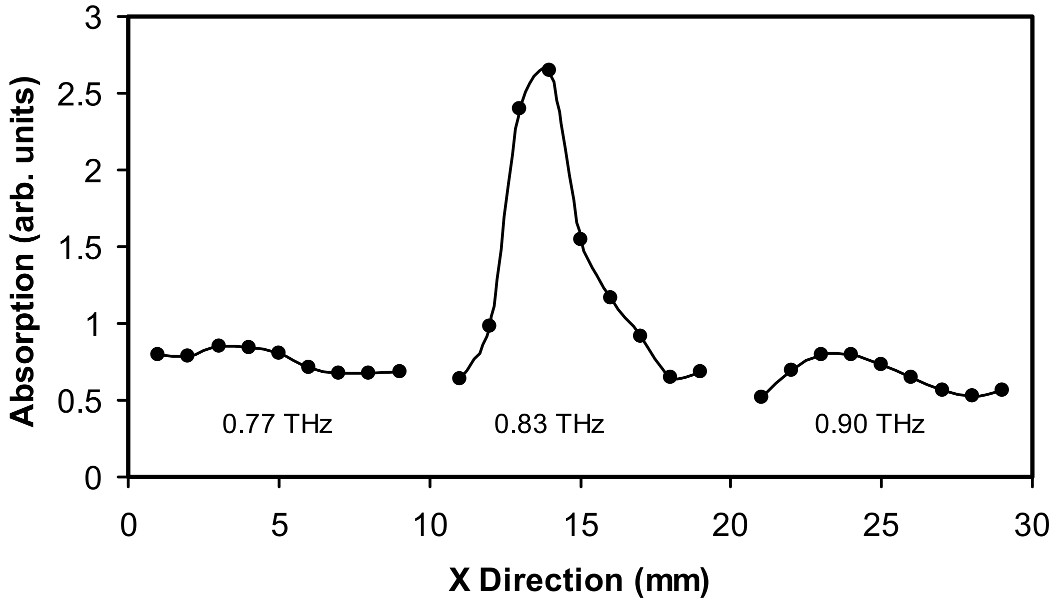

Figure 3.7.0.4: Profile of absorption for cyclotrimethylene-trinitramine (RDX) images at each frequency. This plot is a vertical slice of absorption for the y = 4 mm line in previous figure (Figure 3.7.0.3). The 0.83 THz absorption effect is the most significant as would be expected by the spectroscopy experiments performed in Section 3.3. The x-direction coordinate is arbitrary but the scale is correct.

3.8 Terahertz Time Domain Spectroscopy (THz-TDS)

In addition to continuous wave spectroscopy experiments, THz time domain spectroscopy (THz-TDS) was performed in the lab to confirm the results seen in the continuous wave scans. The THz-TDS method was well established in the lab and was thus a good reference system for testing the functionality of the continuous wave system.

Terahertz time domain spectroscopy is a time resolved excitation and detection scheme that utilizes the properties of photoconductive crystals or other nonlinear processes to generate and detect the THz radiation at room temperature. The technique used here employs a Ti:sapphire laser system (Femtolaser

FEMTOSOURCE Scientific PRO) to generate a short, high powered pulse of approximately 10 fs duration. The laser pulses are generated by means of Kerr-lens mode-locking that operates about a central frequency of 794 nm and with a 75 MHz repetition rate. The short pulse is passed through a 90/10 (reflection/transmission) beamsplitter (BS) into two beams called the pump beam and probe beam. The pump beam is used to generate the THz frequency transients within a photoconductive (PC) switch composed of a biased metallic coplanar strip line antenna. When illuminated by the pump beam, charge carriers are generated within the high mobility, PC switch semiconductor substrate. The biasing electric field accelerates the charges across the antenna gap and generates a THz pulse. A more in-depth treatment on the PC switching technique can be found in [80, 81].

A THz pulse emerging from the antenna is focussed to a point on the sample by two parabolic mirrors. The pulse emerging from the sample on the other side is modulated in such a way that is evident in the characteristic absorption spectrum of the sample. This modulated pulse is then focussed by another pair of parabolic mirrors to copropagate with the probe beam into a <111> zinc selenide (ZnSe) electro-optic (EO) crystal. The EO crystal's refractive index is changed by the instantaneous electric field induced by the THz pump pulse. The linearly polarized probe beam experiences a polarization rotation in the probe beam depending on the EO refractive index. The modulated probe pulse is sent through a quarter wave plate (λ/4) to induce circular polarization, and split into beams of orthogonal polarizations by a Wollaston prism (WP). The separated orthogonally polarized beams are then collected by a pair of balanced diode detectors. The difference of intensity between the two polarizations indicates the extent of the polarization rotation within the ZnSe EO crystal and in turn indicates the electric field of the THz waveform incident on the crystal. For more detail on EO sampling, see [82].

In order to map out the entire THz waveform, the pump beam is variably delayed with respect to the probe beam. This is done by means of a retroreflector mounted on a motorized delay line. The resolution of these steps was 80 femtosecond intervals which is sufficient to generate an accurate representation of the pulse. The entire time-evolution of the THz pulse can be reconstructed by means of repeated pump-probe pulse detections while scanning the delay line. The THz-TDS set up described here is illustrated in Figure 3.8.0.1.

In order to acquire a THz signal to a high degree of sensitivity, a phase-sensitive lock-in detection was utilized in the detection system. The lock-in was achieved by synchronizing with a function generator that induced a 20 V_{pp} square wave bias voltage modulation in the photoconductive switch at a 54.321 KHz frequency. This technique bypasses the typical large acoustic frequency noise associated with DC and low frequency detection measurement. The data was acquired by standard software (MATLAB and LabView).

Before performing THz-TDS experiments on explosives, a waveform time domain scan was performed on an empty cell in order to determine the quality of the pulse and the spectral bandwidth available for spectroscopy. Figure 3.8.0.1 shows the empty cell pulse waveform and the power spectrum indicating the pulse frequency content. The pulse itself was approximately one picosecond long (FWHM) and the resultant bandwidth was approximately 0.7 THz.

Previously, a THz-TDS system in the lab was also used in an experiment to analyze the atmospheric absorption peaks in the THz regime [83]. This absorption spectrum is displayed in Figure 3.8.0.3, and the absorption peaks are listed in the figure inset in comparison to the theoretical values for rotational water vapour absorption lines [84]. The experimental absorption peaks were found to be in agreement with the theoretical lines for water vapour. It is evident that there is a significant number of water vapour absorption peaks within the THz frequency spectrum region of interest. In order to maximize the THz signal, it is necessary to minimize the water absorption process. While it is possible to control atmospheric conditions within a laboratory environment, in a "real world" security screening situation, this may not be feasible. Rather, it is more reasonable to limit the water vapour absorption by limiting the THz radiation beam path length through atmosphere as has been done for the spectroscopy experiments conducted in this study.

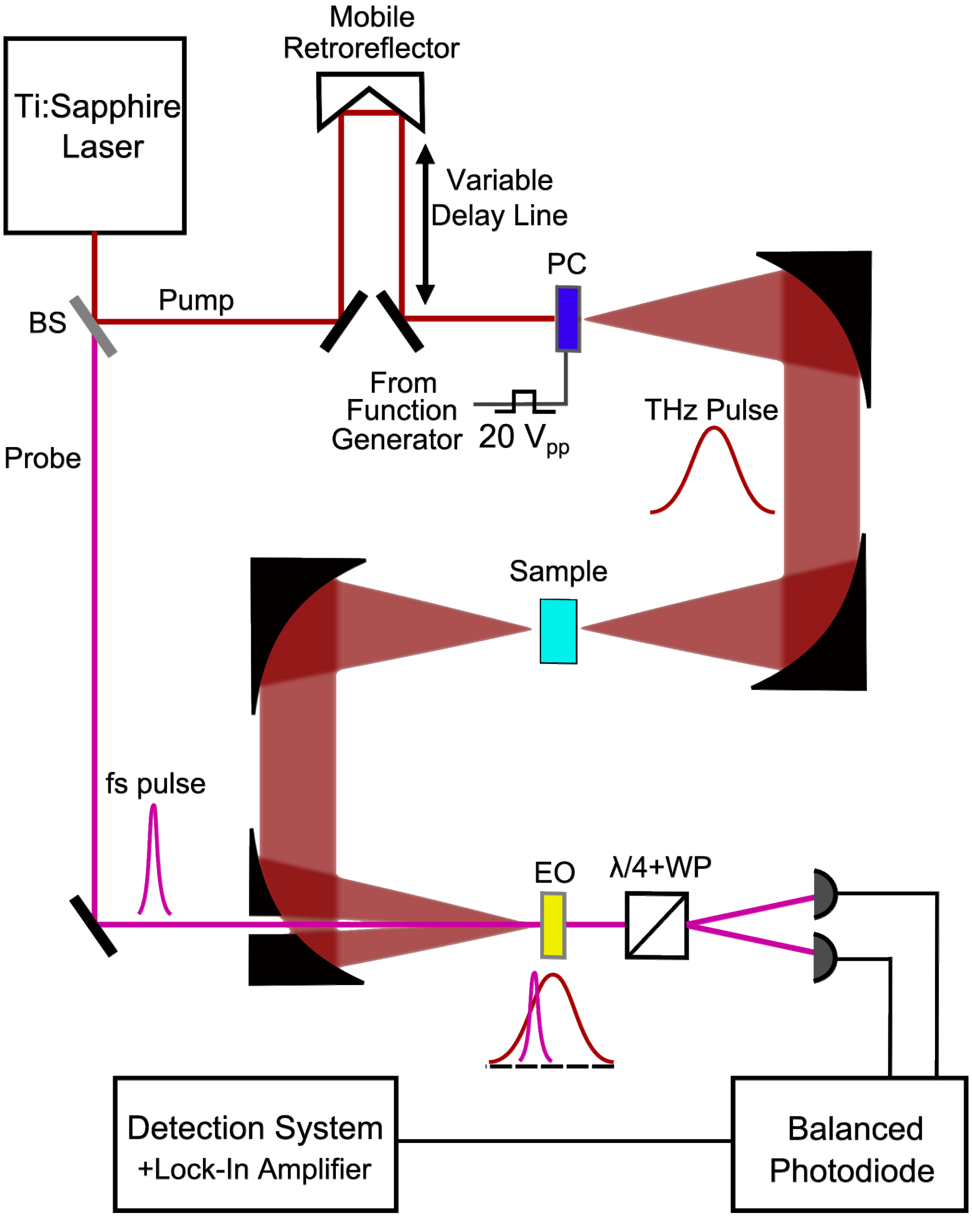

Figure: 3.8.0.1: Illustration of the THz-TDS scheme. The Ti:Sapphire laser emits a femtosecond pulse that is split into a pump beam and probe beam by a 90(R)/10(T) beamsplitter (BS). The pump beam propagates through a variable delay line that controls the relative temporal delay between pump and probe pulses. Then the pump beam irradiates a photoconductive (PC) switch which generates the THz pulse that is focused on to the sample by two 2” diameter off-axis parabolic mirrors. Two more parabolic mirrors focus the transmitted THz pulse to an electro-optic (EO) crystal where it meets with the probe beam and modifies its polarization. The orthogonal polarizations of the probe beam are extracted by a quarter wave plate (λ/4) and a Wollaston prism (WP). The two emergent beams are detected by a balanced photodiode.

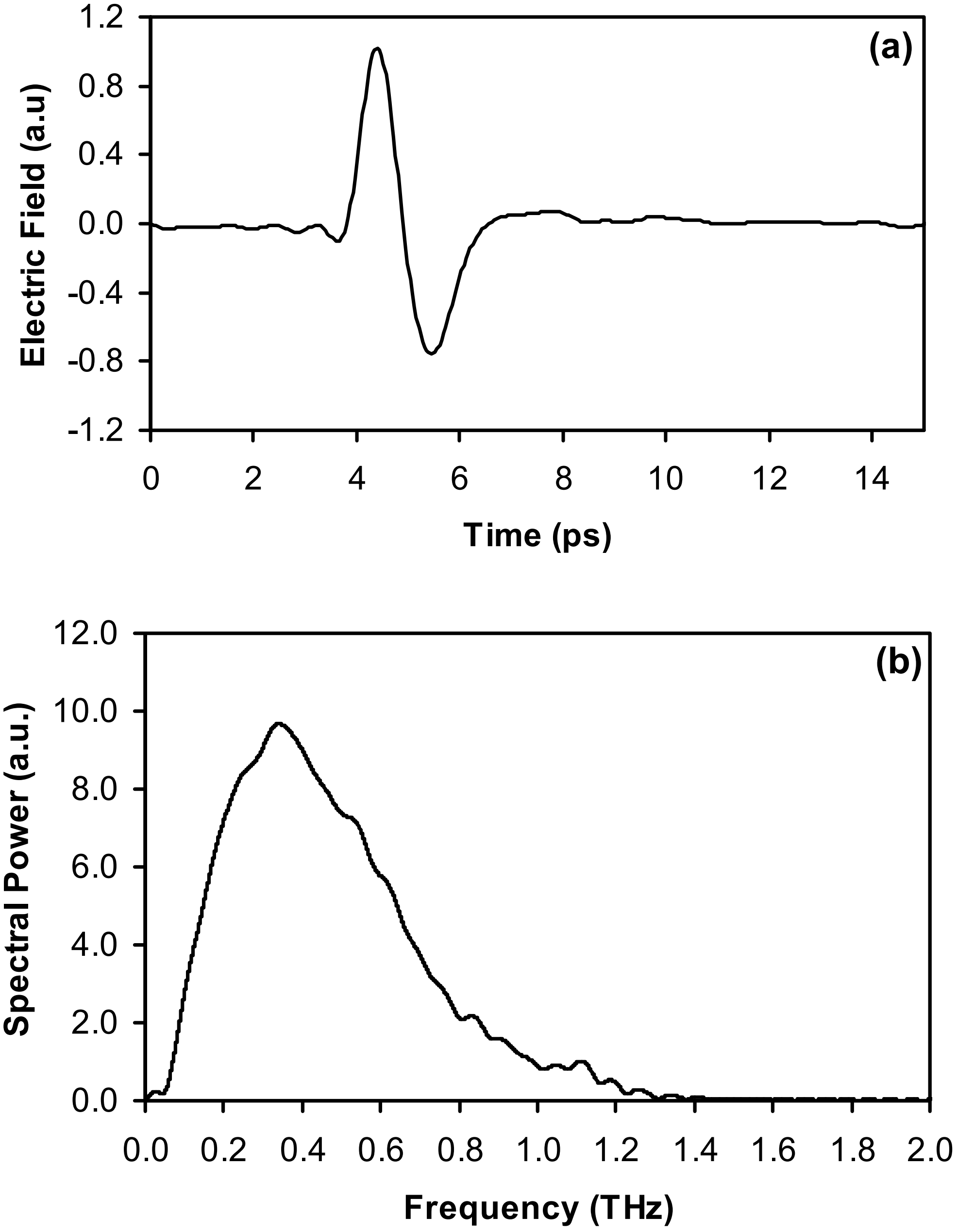

Figure 3.8.0.2: THz-TDS empty cell pulse. (a) The time domain pulse is approximately one picosecond in duration. (b) The power spectrum of the THz TDS pulse displays a bandwidth of approximately 0.7 THz.

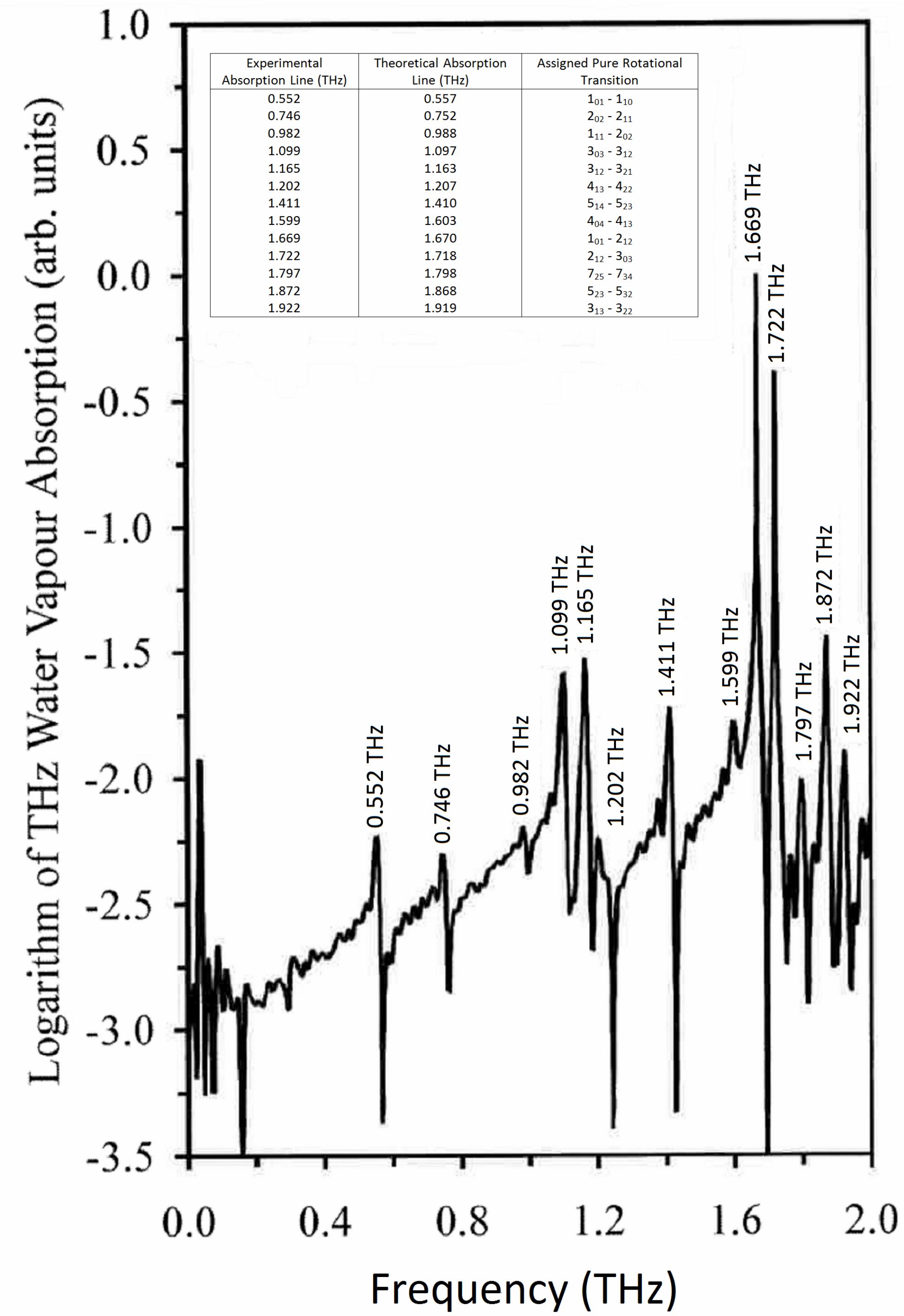

Experimental Absorption Line (THz)	Theoretical Absorption Line (THz)	Assigned Pure Rotational Transition
0.552	0.557	1_{01} - 1_{10}
0.746	0.752	2_{02} - 2_{11}
0.982	0.988	1_{11} - 2_{02}
1.099	1.097	3_{03} - 3_{12}
1.165	1.163	3_{12} - 3_{21}
1.202	1.207	4_{13} - 4_{22}
1.411	1.410	5_{14} - 5_{23}
1.599	1.603	4_{04} - 4_{13}
1.669	1.670	1_{01} - 2_{12}
1.722	1.718	2_{12} - 3_{03}
1.797	1.798	7_{25} - 7_{34}
1.872	1.868	5_{23} - 5_{32}
1.922	1.919	3_{13} - 3_{22}

Figure 3.8.0.3: Absorption spectrum of water vapour in the THz frequency regime. The plot is formed by taking the Fourier transform of a THz pulse traveling through atmospheric water vapour conditions referenced against a pulse traveling in a chamber purged with dry nitrogen. The absorption lines are listed in the inset.

3.8.1 Comparison of TDS Result to CW Spectroscopy Results

Unfortunately, as shown by the Figure 3.8.0.2, the bandwidth of the THz frequency pulse generated by the PC switch method was not wide enough to cover the entire spectrum that could be scanned in the continuous wave spectroscopy section using the Firefly THz system. Figure 3.8.1.1 illustrates this pulse broadening effect as a THz pulse passes through an RDX sample. As could be expected, the HMX and PETN frequency characteristics were out of the range of detection by the THz-TDS system. A broader pulsed system would be required to probe the spectra of HMX and PETN.

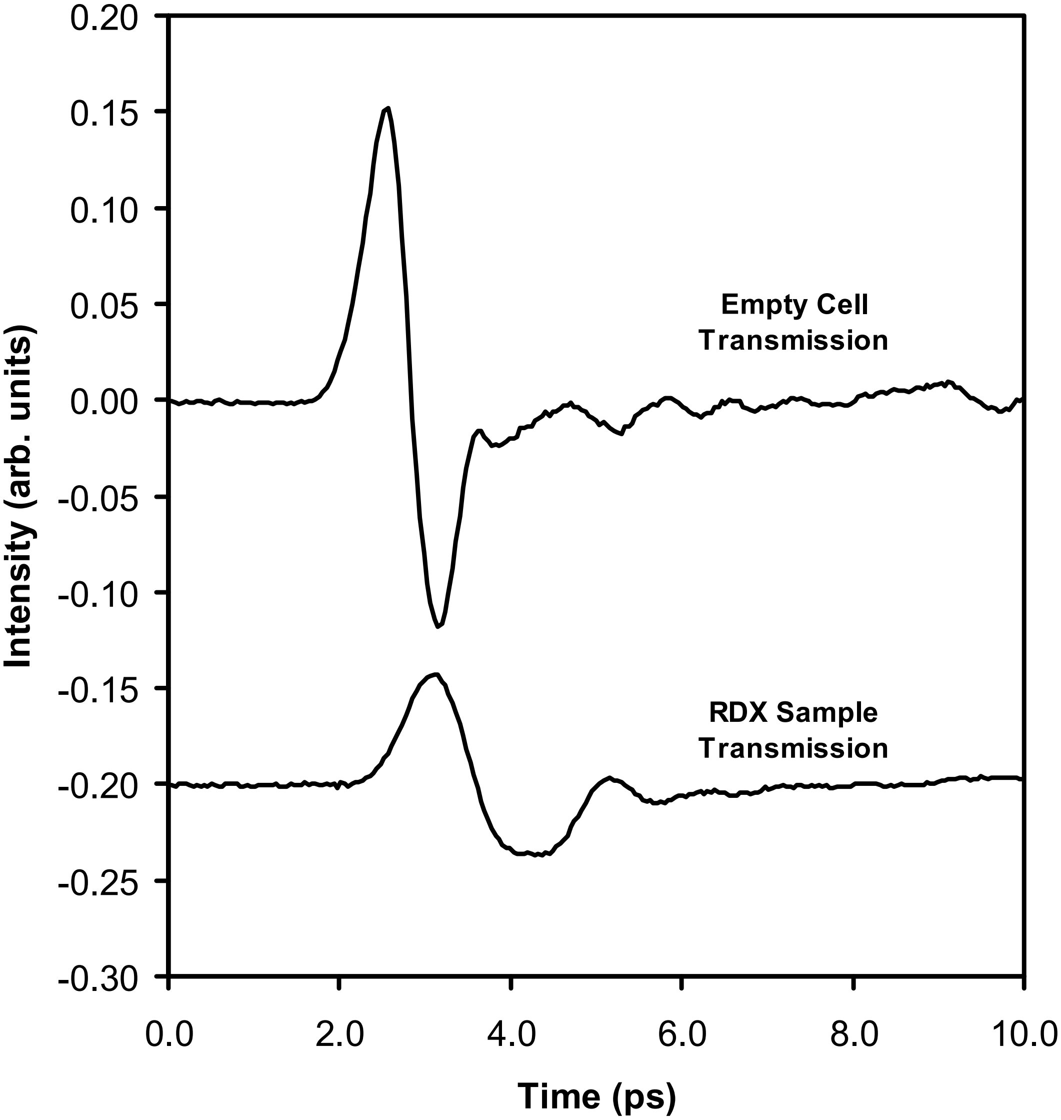

Figure 3.8.1.1: Comparison of THz pulse travelling through empty sample cell and travelling through RDX explosive sample. Note that the RDX transmission experiences a decrease in amplitude and an increase in pulse length due to absorption.

Figure 3.8.1.2 shows that THz TDS compared to the spectrum of RDX attained using the CW Firefly system. Clearly, the THz-TDS method is inferior to the Firefly CW method in this particular case. The only frequency peak distinguishable using the time domain method is the 0.8 THz region peak while the CW result indicates all three peaks of 0.83, 1.04 and 1.5 THz that is expected within the region. Also the 0.8 THz spectral peak seen in the TDS spectrum seems slightly downshifted when compared to the CW result. This downshift may be attributed to the low THz pulse power near the 0.8 THz frequency region as shown in Figure 3.8.0.1. On the plot, the 0.83 THz spectral peak is cut off before it can reach its maximum absorption and hence, it appears shifted lower to 0.8 THz. The THz-TDS method can reach lower THz frequencies than what is accessible by the Firefly OPO. Therefore, explosive samples that have spectral characteristics between 0.2 THz and 0.8 THz would be best analyzed by the pulsed system. However, 0.8 – 1.9 THz frequency region peaks would be best identified by the Firefly THz CW system.

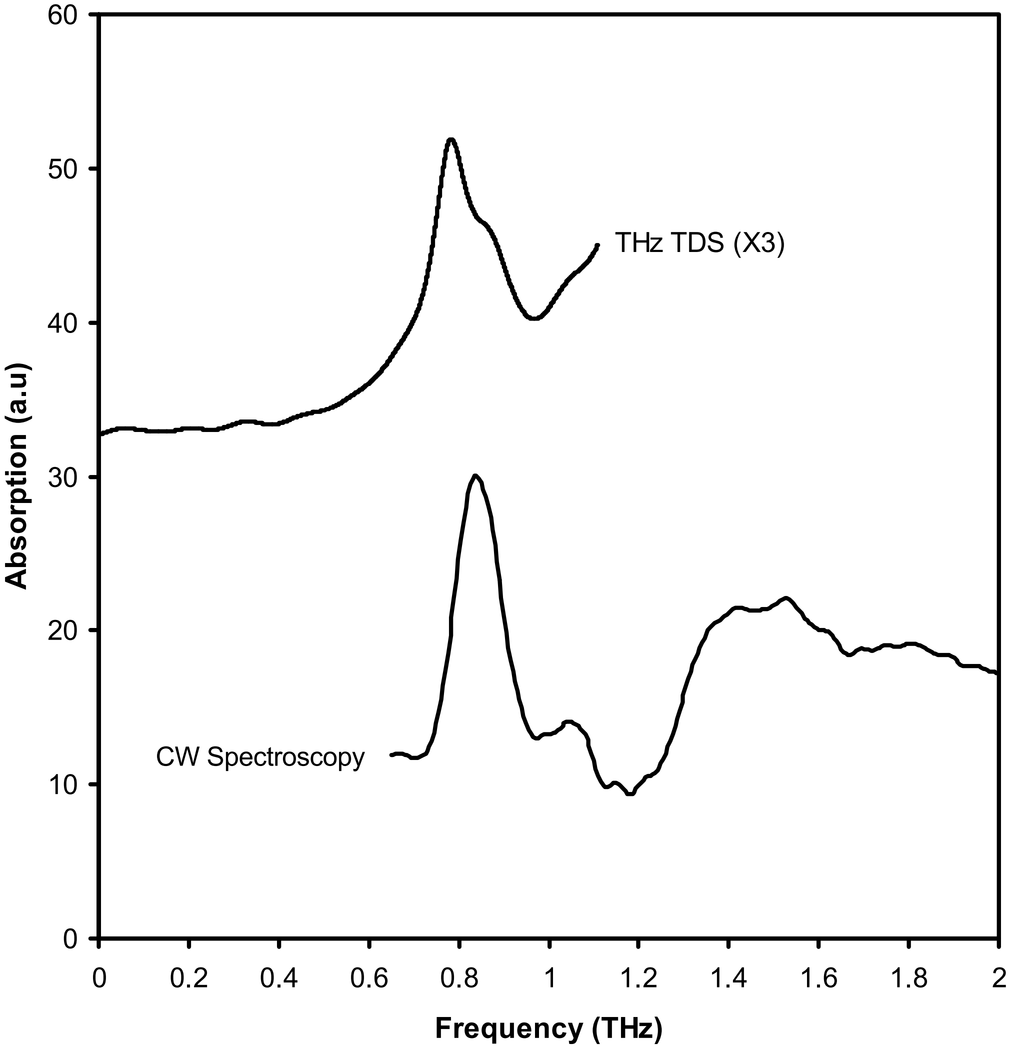

Figure 3.8.1.2: Comparison of terahertz time domain spectroscopy (THz-TDS) to the continuous wave (CW) Spectroscopy of RDX performed using the Firefly THz in the previous section. The TDS spectrum was lower in amplitude so the spectrum was multiplied by three for the comparison. THz-TDS was only able to discern the first 0.8 THz region peak of the RDX spectrum since the lower bandwidth prevented access to the higher frequencies.

Chapter 4

Circuit for THz Frequency Radiation Video Camera

The eventual goal of THz radiation research for security applications is the development of a fast frame rate camera capable of THz frequency ‘vision’. As opposed to the standard detection scheme where only one detector is needed, a camera requires an array of multiple THz radiation detectors, each representing a ‘pixel’ on an image. Currently, there is no such THz frequency video rate camera in existence. The first major obstacle to this development is the unavailability of THz frequency detector elements that are appropriate for such a camera. A suitable THz frequency detector must be both fast responding to yield high frame rates, and be highly compact in order to fit in a high density 2-D array. The second obstacle is that there must be an electronics infrastructure specially designed to interface with the THz frequency detectors and interpret the signals. This is the focus of this thesis chapter. Two circuit designs are presented that perform a data acquisition sequence to read the signal from a 2-D detector array, convert the signal to digital values and communicate the values to a computer terminal. The most viable choice of the two circuit designs depends on the specific electrical characteristics of the THz frequency detector.

4.1 Lack of Suitable THz Frequency Detectors

Modern methods of THz frequency radiation detection were mentioned in the introduction Section 1.1. Most of the detectors are unwieldy, expensive, and complex. Bolometers, electro-optic (EO) crystals, and photo-conductive gated antennas (PCGA) are all singular detectors that cannot image more than a single pixel at a time. Hence, previous THz frequency imaging systems relied on a raster scanning scheme to image an object using these single element THz frequency detectors. Raster scanning involves signal detection while incrementally moving the detector on a 2-D plane with respect to the target object (or vice versa) until an image is constructed. This process is exceedingly time consuming and impractical when considering its application in security screening.

There was some recent progress with multiple element THz frequency video rate imaging which attempts to bypass the need for raster scanning. Aseev et al. [85] developed a 160x120 microbolometer array capable of THz frequency video rate imaging of “up to” 90 frames per second (FPS). However, this device is only capable of monochromatic imaging of frequencies between 1-2 THz. Boldoc [86] also described a video rate microbolometer camera. However, this device is only a 3×2 pixel array detector so it is more useful for constructing still images at high rate raster scans than for video imaging. Further research is required before microbolometer arrays will achieve the fidelity required by a video rate camera that is used in stand-off security screenings.

4.2 Proposed THz Frequency Detectors for the Circuit Design

A simultaneous research effort in our lab, led by Dr. Abdulhakem Elezzabi, is advancing a novel THz frequency detector composed of an antenna coupled with a quantum cascaded metal-insulator-metal tunnel diode (QC-MIM). These devices are theoretically ideal for a video camera circuit since they are miniaturized and have a fast response time. The antenna structural geometry is designed such that THz frequency resonances are optimized. When THz frequencies illuminate the antenna, an AC (alternating current) signal is induced which propagates through the diode region of the device. The diode region rectifies the signal into a DC (direct current) signal via nonlinear current–voltage characteristics of the (QC-MIM) structure. The circuitry presented in the following sections is designed to interpret the DC signal expected from these specific THz antenna detectors.

4.3 Design Constraints

The design was primarily constrained by the limitations of the microfabrication facility in the University of Alberta. It was required that the circuit was kept as simple as possible such that the eventual circuit could be formed on one or two layers of an integrated circuit board. Another consequence of the simplicity requirement was that all components within the matrix of THz frequency detectors had to be passive. Ideally, only the THz frequency detectors and signal transmission lines would be present in the detector matrix area. All active components such as amplifiers and microcontrollers had to be external to the 2-D array.

Conventional camera circuitry used for the visible light regime was considered but found unsuitable for the purposes of THz frequency detection described in Section 4.2. Some of the most common video cameras for the optical frequency regime in use today, employ a charge-coupled-device (CCD) to capture visible light images. A CCD functions by building up charge in a photoactive region (epitaxial layer of silicon) that is proportional to incident light intensity. The charge in one pixel is then sequentially “shifted” down the register until it is collected by an analog to digital converter (ADC) processor and analyzed. This sequence is repeated for each pixel in the array. However, a CCD circuit is not easily applicable to antenna structures since these particular THz frequency detectors function as a current source rather than storing a build up of charge. In order to utilize the register shift mechanism of a CCD, the current must be converted to a charge and trapped at each pixel region before the register shift sequence. This would require active elements at each pixel within the array, which is not possible given the constraints mentioned earlier. A second common detector circuitry for visible regime cameras is complimentary metal-oxide semiconductor (CMOS) detection. The detection circuitry used for CMOS is somewhat faster than CCD systems; however, these require field effect transistors (FET) to be used at each pixel element. Again, the passive element constraint of fabrication capabilities prevents the CMOS scheme of detection from being used in this project. There was a need to design a simpler circuitry system that could function with the THz antenna detectors and still comply with the circuit design requirements.

4.4 Circuit Design

The external circuitry was prototyped on a standard testing breadboard. Several iterations of the prototype were assembled while optimizing the speed and performance. Since the actual THz frequencies detectors were still in development, light emitting diodes (LED) were used in place of the QC-MIM antenna detectors and configured for light detection functionality.

Although, light emitting diodes are conventionally used as light sources, they can also be used as a photodiode by simply switching the polarity of the LED into reverse bias within the circuit. The only difference between a photodiode and an LED is that a photodiode was specifically doped for high sensitivity light detection while an LED is optimized for light emission. The dual functionality of the LED is commonly used to create low cost bidirectional systems in which LEDs are used to emit and detect signals [87]. This capability was exploited in this project as a cost effective proof of principle for THz frequency detection.

Since the noise, impedance, expected current, voltage and AC characteristics of the proposed antenna were unknown; a specialized integrating amplifier was chosen as the heart of the signal processing circuit component. The function of this amplifier will be described here in conjunction with an outline of the overall light sensing action.

Both of the designs were configured such that the elements were in current mode detection. Ideally, since each LED is accessed (selected) individually and sequentially, only one LED is interacting with the circuit at a time. Light incident on an LED causes spontaneous generation of charge carriers within the diode semiconductor. These carriers create a voltage difference across the diode. The induced current travels from the LEDs to an integrating amplifier chip which collects and traps the charge carriers using capacitors and a time-gated switch. The function of the integrating amplifier is illustrated by the schematic in Figure 4.4.0.1. The trapped charge builds up a capacitance within a gated cycle and the resultant voltage is detected using the Analog to Digital conversion module within a control microprocessor chip.

The motivation behind using a charge integrating amplifier rather than a standard differential amplifier was to make the circuit as tolerant as possible to variable current characteristics of the proposed THz frequency detectors. It is expected that the transmission lines in the diode region of the THz frequency detector elements internally rectify the initial THz frequency electrical oscillations. However, neither the quality nor the extent of this rectification is known. A standard amplifier would amplify any imperfection or noise in the signal making the useful DC signal unreadable. In contrast, an integrating amplifier serves its function regardless of the extent of signal rectification, presence of noise, or AC fluctuations. So long as the THz frequency detectors output an average DC value, the integrating amplifier can read and amplify the signal. Furthermore, the integrating amplifier can potentially detect extremely low intensity signals due to the time-gated nature of the amplification. If a DC signal is low, it is possible to extend the time interval for voltage build up in the capacitors. However, this design also has some drawbacks. Since the signal is amplified as a time-gated voltage build up in the internal capacitors, the amplification is intrinsically tied to the detection rate. If there is a low signal, the time required to amplify it increases thus decreasing the frame rate of the camera overall. Also, if the camera contains a large number of detector elements, each detector would require time for signal amplification so frame rate suffers. Therefore, the integrating amplifier may not be ideal for high performance requirements of large scale, high resolution detector arrays. Once the detectors are fabricated and the characteristics become known, it may be advisable to modify the design. This design serves merely serves as a conceptualization for the THz camera external circuit.

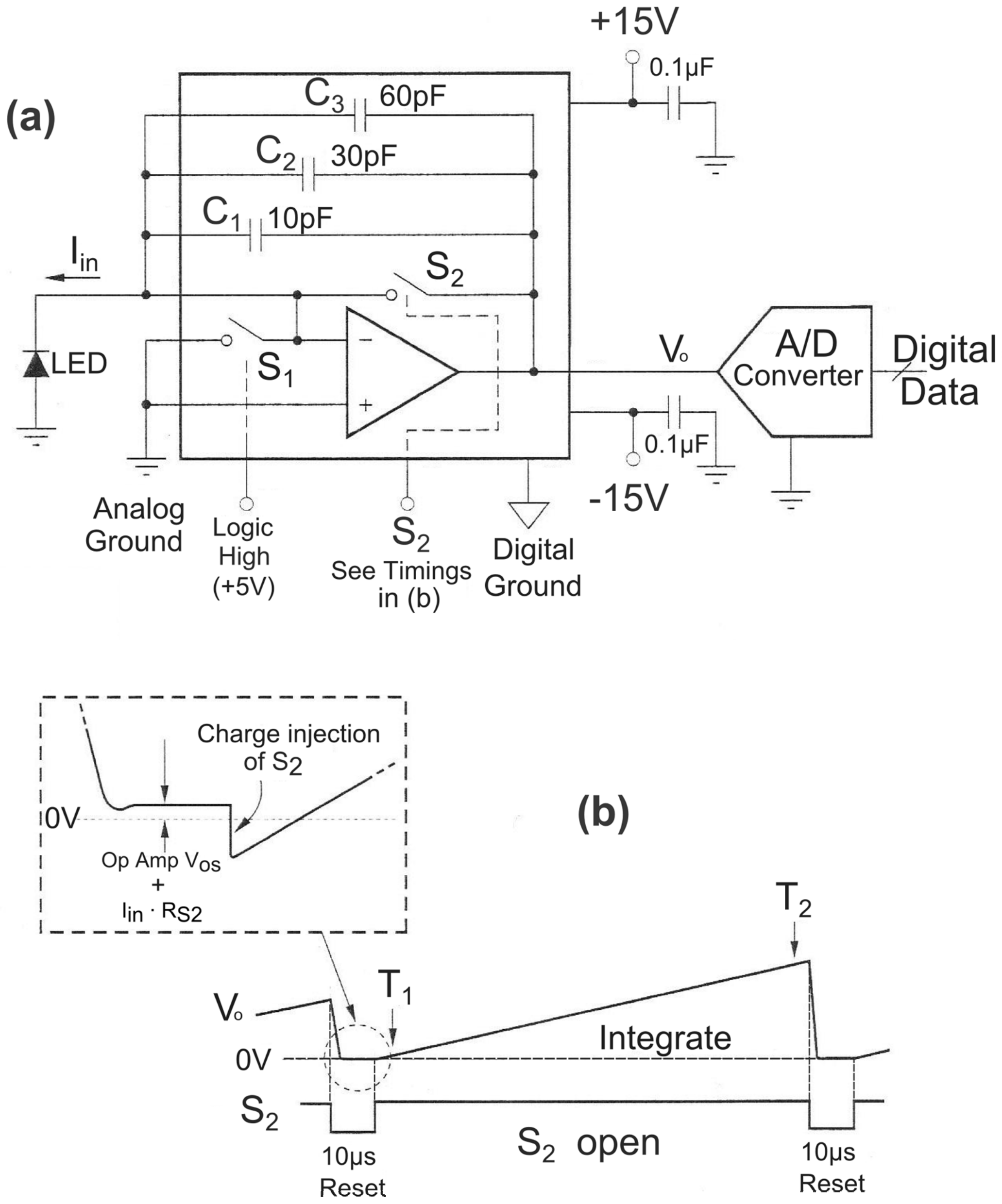

Figure 4.4.0.1: (a) indicates the basic schematic of the integrating amplifier IVC102 integrating amplifier. (b) shows the time-gated integration scheme. The charge is trapped within the capacitors of the amplifier and an analog to digital converter reads the voltage in a time gated scheme. Figure adapted from IVC102 microchip Manual [88].

The first circuit design utilized a PIC16 Microcontroller and two analog switch chips capable of 16 to 1 switching for multiplexing the LEDs. The multiplexing of the LED elements was achieved using minimal wire connections. Figure 4.4.0.2 illustrates the basic design of this circuit. The cathodes of LEDs on a common row were all wired together. The anodes of LEDs on a common column were wired together into the ground of the circuit (in reverse bias configuration). This design is particularly appealing since it saves on the number of leads required for large detector arrays. A single lead is needed for all elements on a common row and a single lead for all elements on a common column. For example, a 10×10 array only requires 20 wire leads.

In order to access an individual LED the two analog switch chips would triangulate the LED by selecting the one row and one column to read. Each LED element was read sequentially (one at a time) by an analog to digital converter. All elements in the top row are read from left to right. Then the next row is scanned in a similar manner until all rows are read. Then the process begins again from the top row for the next image frame.

All the power supply conversions and voltage conversions were performed on the same breadboard to minimize space. However, there was capacitive and inductive noise introduced because these currents were flowing close to the chip components. Programming was written in Assembly language in order to most directly instruct the microcontroller, resulting in maximum control over the sensitive timings of operations. These timings were critical since the ultimate goal was to create a circuit capable of quickly processing full matrices of detectors at 30 frames per second. The code for the microcontroller can be seen in Appendix B and a photograph of the circuit on a breadboard can be seen in Appendix F.

The circuit was tested using a halogen light source (Mitutoyo) and an oscilloscope to characterize the signal quality output from the multiplexed circuit. The signal ADC conversion was performed on the PIC16 module and sent via USB interface to a computer terminal where it was displayed as a value between 0 – 255 representing an amplified voltage of 0-5 V. It was found that there was a great deal of "crosstalk" between the adjacent row LED elements on the same column. If one LED was exposed to light, the signal would be evident from the other LEDs in that row. This crosstalk may be due to the internal capacitive effects of the LEDs. Voltages would be transferred across the circuit to interfere with other LEDs. However, there was a maximum value to which the adjacent LEDs would experience interference. If high enough intensity light is used, there is a maximum threshold that the crosstalk interference reached. It was found that if a high enough intensity light is used in the detections and the data acquisition software is programmed to discard signals lower than the threshold, the circuit could be viable for light detection. Figure 4.4.0.3 illustrates this threshold effect as seen by an oscilloscope diagnosing the integrating amplification of a 3×2 array of LEDs numbered 'one' to 'five'. Although element 'five' is the LED which experiences an incident light signal, element 'two' on the same column (adjacent row) indicates a signal as well, but saturates at a threshold. As the intensity of the light on element 'five' increases, the signal read from element 'two' does not. This behaviour could be a critical limitation when measuring low level light. However, this design should not be disregarded due to the crosstalk problems observed with the LEDs because the THz frequency detectors may not behave in the same way. The proposed antenna structures would not have any internal capacitances. Thus, the crosstalk may not be evident once the actual THz detectors are incorporated into the system. Tuning the timings of the program, it was found that 25 frames per second were possible for an 8×6 array if the integration time for each element was configured for 0.8 ms when illuminated by the halogen light.

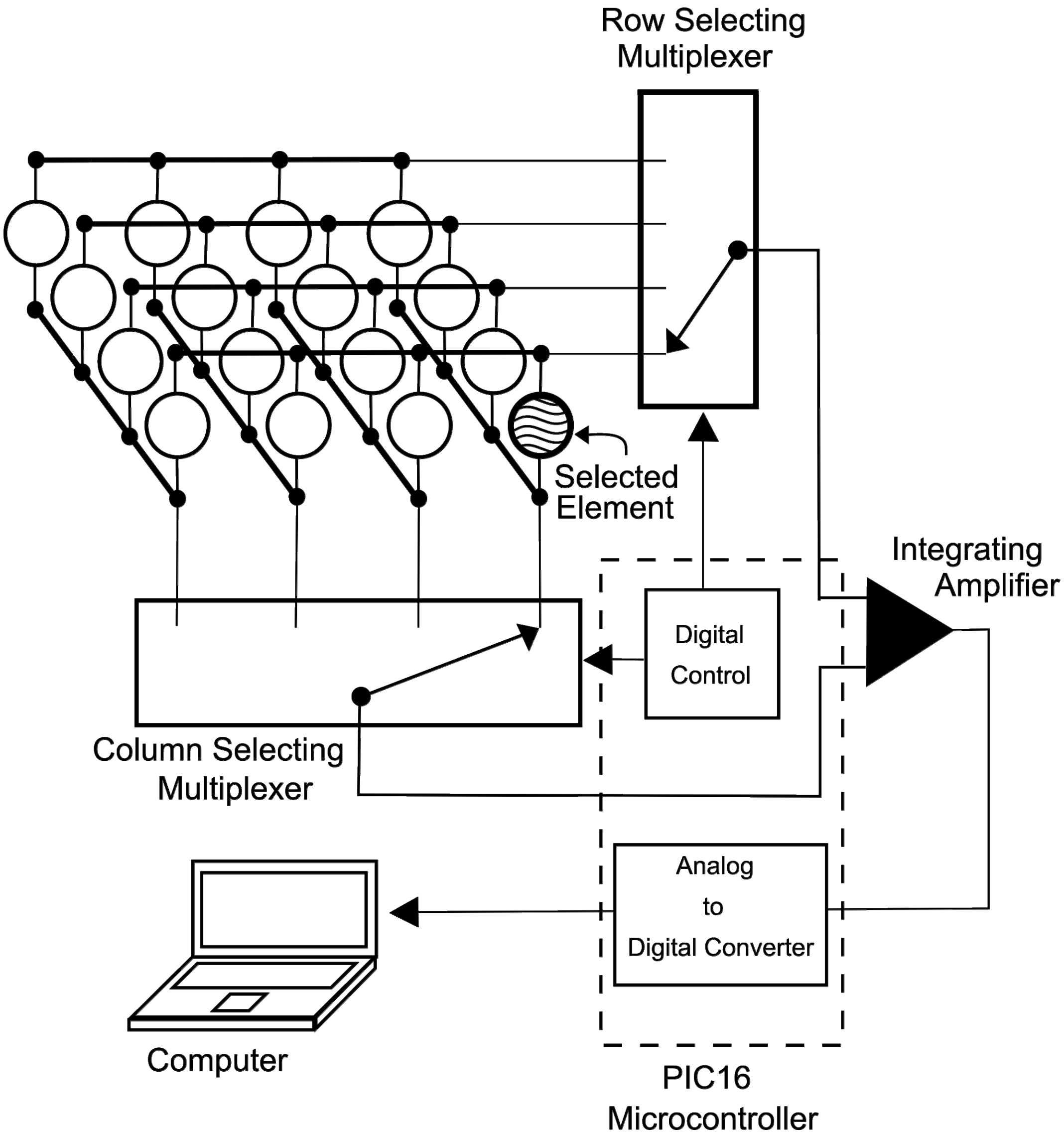

Figure 4.4.0.2: The first proposed design for the THz frequency camera circuit utilizing a PIC16 microcontroller to control an eight by six LED array connected by common rows and common columns in a crosshatched configuration.

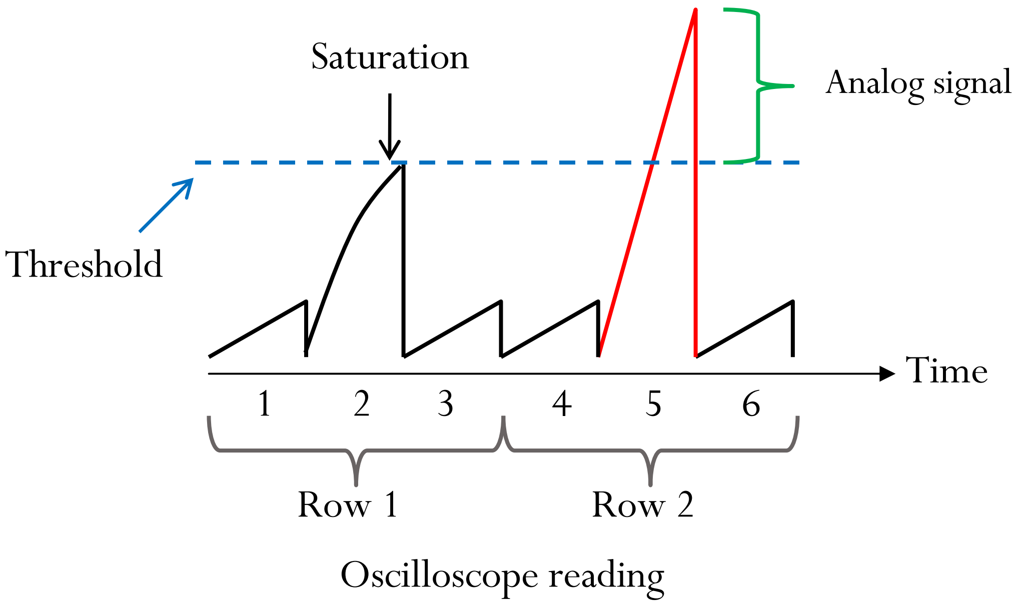

Figure 4.4.0.3: Illustration of the oscilloscope reading that is probing the integrating amplification action for the crosshatched multiplexing design. The triangles represent the voltage accumulated by the integrating amplifier over time until the next element is accessed. Element 5 is being illuminated by light, however, element 2 is also experiencing a signal due to crosstalk effects on common column lines. However, the crosstalk effect only causes the element to build a signal up to a finite threshold. If this is set as the cutoff threshold, the crosstalk effects can be bypassed.

The second design for the THz frequency camera circuitry was realized using the Arduino Duemilanove self-contained microchip package [77]. The essential components were very similar to the first breadboard design but in a smaller form factor with minimized noise effects. The programming (Appendix C) was written using the "processing" [89] Java script based terminal rather than Assembly language. Although Java provided less control over the timings, the crystal oscillator within the Arduino chip itself was considerably faster so the timings were of less concern for this prototype.

The Multiplexing circuit was also modified in order to eliminate the crosstalk experienced when the column cathodes are common and the row anodes are common. Instead of using the standard crosshatched wiring used in the previous circuit, individual leads were connected to each LED anode. This increases the number of wires required, but all LED signals become independent of each other. A photograph of the breadboard circuit can be seen in Appendix F.

In order to test the circuit, a bright Halogen light source (Mitutoyo) was used to illuminate each of the LEDs. The "processing" code (Appendix C) provided a visual representation of which LEDs were illuminated along with a 0-255 integer value indicating the intensity of the signal in a similar fashion as the previous design. Using a small 6 (3 columns and 2 rows) element prototype array of LED detectors assembled on a breadboard, the circuit was able to read the light intensity on the LEDs at approximately 50 frames per second. This was possible by setting the variable integrating amplification time to approximately 3 ms per LED element. First, each isolated LED received light by itself to demonstrate that each LED element was accessed independently with minimal signal crosstalk. Then it was confirmed that the LEDs were detecting at reasonably similar sensitivity by directing the light at multiple elements simultaneously. Since this design required N+1 wire leads for N detectors, a 10×10 array of detectors would require 101 leads. Although this is difficult to test on the breadboard, it could be fabricated on a circuit board without much difficulty.

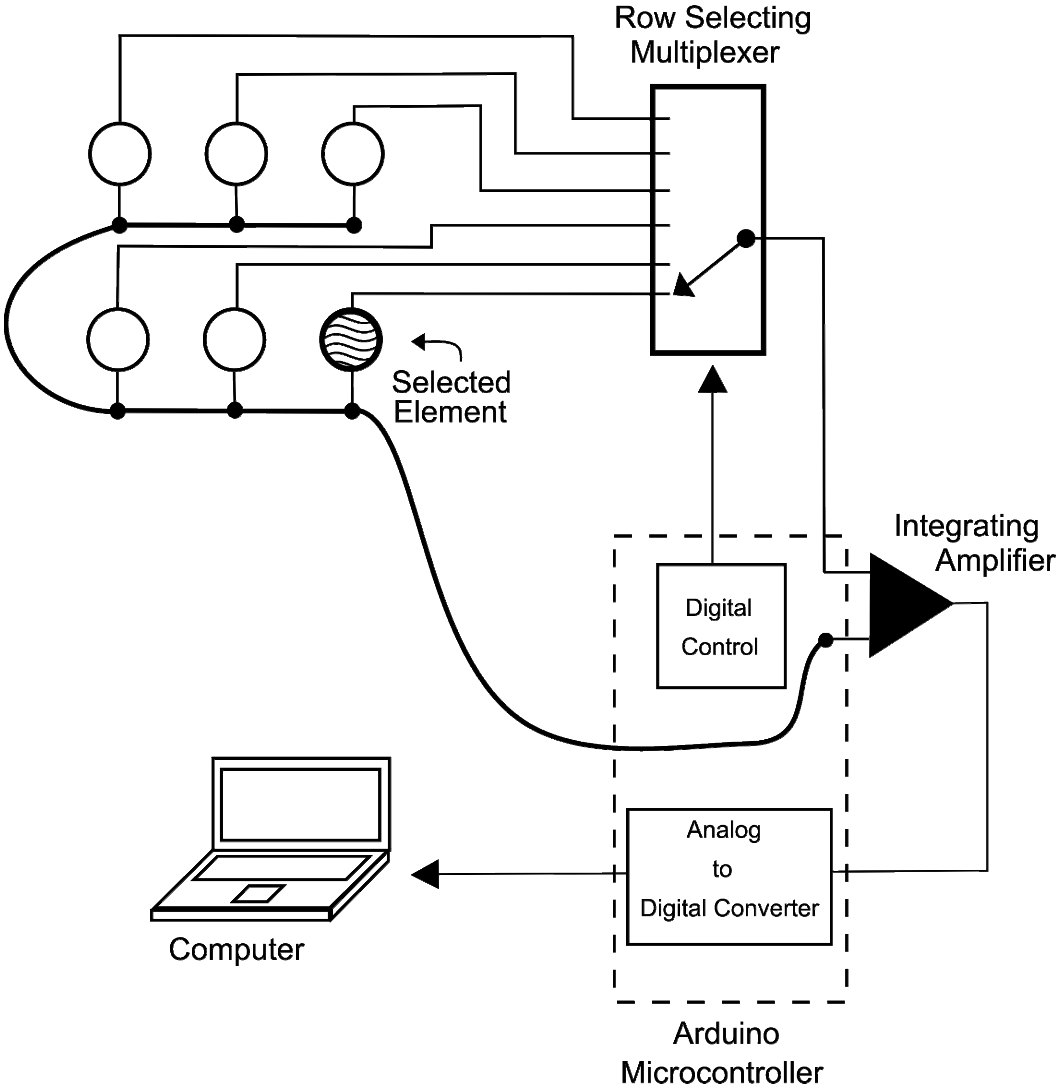

Figure 4.4.0.4: A second proposed design for the THz frequency camera circuit. An Arduino Duemilanove microcontroller was used to control a 2×3 array with independent leads running from the anode and a common wire from the cathodes.

4.5 Frame-rate considerations

It is important to reiterate that the main concern for a real time THz frequency imaging camera is the speed at which elements are accessed. The frame rate is limited by the rate at which each individual element is read. The current design's integration amplifier is a major impeding factor for high speed scanning. The amplifier has an intrinsic time delay associated with charging the capacitors using the LED current. The longer the integration time, the more sensitive the system can be to incident light radiation. However, a longer integration interval results in a significantly lower frame rate since each LED would require more time to acquire a sufficiently amplified signal. With a bright THz frequency source, the charge would build faster and less integration time would be required. Clearly, the frame rate capability of these designs is radiation intensity dependent. For instance, in order to maintain the 50 FPS functionality observed using a 2x3 element array in a 100x100 array, integration time must be lowered from 3 ms to 2 μs. This would decrease the amplification significantly at each element. The design could be modified to decouple the frame rate from the intensity level, but this would require more information about the electrical characteristics of the THz frequency detector elements. While the presented circuits may not be optimal for high speed reading, they were designed to be versatile and capable of interfacing with THz frequency detector elements of various electrical characteristics.

Chapter 5

Summary

The project gave insight into the viability of continuous wave (CW) THz frequency spectroscopy and imaging for security applications. The Firefly THz optical parametric oscillator (OPO) was demonstrated to be a versatile instrument for this purpose, capable of transmission spectroscopy, THz frequency imaging, and detection of concealed explosives.

In Chapter 2, the THz spectroscopy system, consisting of the Firefly-THz OPO system coupled with a Golay cell detector, was characterized and its limitations were quantified. The THz radiation output was found to be collimated and the FWHM spatial profile of the beam was found to be approximately 1.3 cm. THz radiation transmitting through atmospheric vapour was limited to 30 cm of freespace propagation. The Golay cell could not detect radiation further than 30 cm away from the THz output window. However, this result was attained using an additional polyethylene filter which attenuated the THz radiation as well as the non-THz noise. Without the filter, transmission through air could be extended, but there would be less confidence on whether the detected frequency was purely THz.

It was found that although the Firefly OPO system was capable of emitting detectable THz frequency power at tuning frequencies between 0.7 and 2.5 THz when the Golay cell detector was situated directly in front of the THz output window, the upper and lower extremes of this range were of too low power for detection in experimental conditions, which required transmission through atmosphere and reflection from a parabolic mirror. Since the Golay cell detector yielded no frequency information of the THz output, a lamellar split mirror interferometer was designed and assembled for the purpose of characterizing the OPO system and determining realistic limitations for the system. A software graphics user interface was created using MATLAB to control the motor of the translation stage of the interferometer. The program performed the Golay cell signal data acquisition as well as the Fourier transform algorithm to determine the frequency content of the THz radiation. Using the mirror interferometer system and the MATLAB program, the detectable frequency tuning capabilities for spectroscopy were determined to be between 0.75 - 1.8 THz. OPO tunings above and below these frequencies produced radiation power that is below the noise floor of the Golay cell detector. Hence, all spectral plots obtained in subsequent experiments were truncated around 0.65 and 1.9 THz to encompass these apparent limitations. The interferometer also determined that the Firefly OPO had a CW output bandwidth of 48 ± 3 GHz which was consistent with the 50 GHz bandwidth specification cited by the manufacturer.

An instrumental error was quantified regarding the frequency tuning operation of the Firefly OPO. There was a discrepancy between the instructed frequency and the resultant tuning frequency of the OPO of approximately ± 0.75 GHz (standard deviation) and a maximum deviation of ± 1.30 GHz. This discrepancy was suspected to be an intrinsic rounding error in the Firefly software since the error appeared periodic for tuning instructions of equal intervals. Since the bandwidth of the OPO was 50 GHz, this tuning discrepancy was deemed insignificant.

In addition to characterising the Firefly OPO, the interferometer limitations were also quantified. For 10 mm mirror translation, encompassing 4000 data points (using 2.5 µm step intervals), the interferometer was capable of 15 GHz resolution. This could be further increased by extending the scan. However, the 10 mm maximum mirror displacement was found to be optimal for the optical set-up used in this thesis. Since the resolution of the Firefly tuning system was limited by the bandwidth to approximately 50 GHz, the interferometer could be useful in future studies to perform finer resolution spectroscopy of sharper spectral peaks that would be expected for gas phase explosives spectroscopy.

In Chapter 3, continuous wave (CW) spectroscopy was performed on Cyclotetramethylene-tetranitramine (HMX), cyclotrimethylene-trinitramine (RDX), and pentaerythritol tetranitrate (PETN) and Composition 4 (C-4). Spectral peaks of RDX were found to be broad signatures at 0.83, 1.04, and 1.51 THz. HMX displayed a single spectral peak at 1.45 THz. PETN showed a single spectral peak at 1.78 THz. These results were compared with the findings of Liu [39] and Tribe [37] and the occasional inconsistencies of spectral peak locations suggested that explosives spectral signatures may be dependent on the specific manufacturing process. Explosives of the same type may yield differing spectral characteristics in the THz frequency range depending on the fillers used, powder grain sizes, and moisture content of the explosives. The frequency range limitation of the Firefly resulted in a limited ability to identify HMX and PETN explosives. Specifically, icing sugar was found to yield a similar spectral shape to HMX. Explosives identifiable using the Firefly system should yield multiple spectral absorption peaks within the 0.75 – 1.8 THz range to reduce the possibility of false alarms. A spectroscopic map of Composition 4 (C-4) resulted in a spectrum similar to that of RDX. This result was expected since C-4 is composed of 91% RDX. A systematic approach to identify explosives was proposed using the Lorentz lineshape function fit algorithm in the "Origin" data analysis program. In addition to determining the spectral peaks with the spectral data, the Lorentz lineshape fit also computed the peak widths. This approach essentially provided additional numerical criteria (i.e. the coefficients of the Lorentz lineshape functions) that could be used for explosives spectra comparison.

Explosives were also tested for thickness threshold of detection. The THz radiation beam path transmission length through a sample was varied using polystyrene windows. As would be expected, spectroscopy of samples prepared too thick, or too thin resulted in erroneous results. A criterion of validity was proposed such that the results could be confidently assessed. Specifically, it was found average absorption ratios between 3 – 9 (arb. units) across the spectrum are likely to yield reliable explosive spectra.

Spectroscopy of concealed explosives was performed through various dielectric materials. It was found that RDX could be detected through envelopes and fabrics using transmission spectroscopy configuration. THz radiation imaging was performed using a raster scan method. Specifically, a tinfoil "A" shape was imaged through 2 cm of Styrofoam and THz imaging detected a paperclip hidden within an envelope.

In addition to imaging concealed objects, a method was proposed for imaging explosives and simultaneously chemically identifying the specific explosive. Imaging was performed on a triangular shape of RDX powder within an envelope at three frequency tunings about the first characteristic peak of RDX at 0.83 THz. These three tunings (0.77, 0.83, and 0.90 THz) essentially "searched" for the signature 0.83 THz peak. If the image produced by 0.83 THz tuning indicated the triangle was strongly absorbing in relation to the 0.77 and 0.90 THz absorptions, then the chemical composition of the triangle could be identified as RDX. This method successfully demonstrated the identification of RDX within an envelope.

In Chapter 4, a circuit was designed for a proposed THz frequency, video rate camera that would be capable of imaging and spectroscopy simultaneously. The circuit was intended as an external electronics system for a high density array of novel THz detectors composed of an antenna structure coupled to a quantum cascade metal-insulator-metal (QC-MIM) diode region. The circuitry was designed within the constraints of the microfabrication capabilities of the available equipment. Since the THz detectors were not yet available, the circuit prototypes were tested using light emitting diodes (LED) set in light detection mode. Two viable circuit designs were proposed which have advantages and disadvantages depending on the specific electrical properties of the final THz Detectors. The first design was simplest in terms of the wiring required to connect each individual detector. However, a significant amount of "crosstalk" was evident between LEDs. The signal observed by one LED could affect the signal read from an adjacent LED on the same column in the matrix. This was attributed to the capacitive effects of LEDs so the intended THz detectors, which are expected to have low capacitance, may not experience such a “crosstalk” between elements on the array. The second design eliminated the “crosstalk” effect by providing a single wire for each LED anode lead in the array. However, this required much more wiring than the first design.

This work has made contributions toward the ultimate goal of developing a practical and viable scheme for “real world” THz radiation security screening. However, the particular explosives detection system studied here, consisting of an OPO coupled with Golay cell detector, should undergo further optimizations and experimentation before it can be implemented into a security screening system. The limited effective tuning range of the system resulted in some difficulties in identifying explosives with broad spectral characteristics like HMX and PETN. While a recalibration of the OPO cavity could result in a wider effective spectroscopic scan range, there remains a possibility that there exist other non-explosive materials that could confuse the spectroscopy results. This possibility was illustrated by the similarities between the spectrum of icing sugar and that of HMX. Further optimizations in computational spectral assessments like the Lorentz fit could also lead to more reliable discernment of explosive materials.

For future studies, we are motivated to perform experiments into reflection spectroscopy, which is considered more practical for stand-off imaging security screenings. Spectroscopic experiments into a greater variety of explosives could provide more insight into the complex THz frequency vibrational motions. Liquid and gas phase explosives would be of great interest since their spectral characteristics are expected to be sharper and more intricate.

In addition to security applications stated above, future work employing the same technology studied here can be utilized for biomedical applications. Since Terahertz frequency radiation is inherently safe and compatible with biological systems, it may be utilized for early detection of cancers and abnormalities in teeth and dental work [90]. THz frequencies are highly absorbed by water. This property can be exploited to scan for abscesses and infections in teeth since these abnormalities have distinctly higher moisture contents than healthy teeth. Skin cancers also show distinctions from healthy skin in a THz frequency image. When comparing this non-invasive method to the conventional biopsy method for cancer diagnosis, the advantage of THz frequencies is clear. The work performed on explosives in this project can be readily extended toward biomedical applications since the logistical and technical issues are common to both fields of research.

Bibliography

[1] Mehta, and Smith-Bindman, “Airport Full-Body Screening: What Is the Risk?,” *Archives of internal medicine. PMID 21444831*, 2011.

[2] Board of Radiation Effects Research Division on Earth and Life Sciences National Research Council of the National Academies, “Committee on the Biological Effects of Ionizing Radiation, Health Effects of Exposure to Low Levels of Ionizing Radiation: ,” *BEIR V. Washington, DC: National Academies Press*, 1990.

[3] David Brenner, “Cancer risks attributable to low doses of ionizing radiation: Assessing what we really know,” *Proceedings of the National Academy of Sciences* vol. 100, no. 24, 2003.

[4] Smiths Detection. "Developement of airport security technologies," [July 30; http://www.airport-int.com/article/securitynet-the-shape-of-things-to-come.html.

[5] Dana A. Shea, and Daniel Morgan. "Detection of Explosives on Airline Passengers: Recommendation of the 9/11 Commission and Related Issues," [July 2, 2011]; http://www.fas.org/sgp/crs/homesec/RS21920.pdf.

[6] M. R. Scarfi, M. Romano, R. Di Pietro, O. Zeni, A. Doria, G. P. Gallerano, E. Giovenale, G. Messina, A. Lai, G. Campurra, D. Coniglio, and M.

D’Arienzo, “THz exposure of whole blood for the study of biological effects on human lymphocytes,” *J. Biol. Phys.,* vol. 29, pp. 171-177, 2003.

[7] G. P. Gallerano. "THz-bridge -Terahertz Radiation in Biological Research, Investigation on Diagnostics and Study of Potential Genotoxic Effects," [August 20, 2011]; http://www.frascati.enea.it/THz-BRIDGE/reports/THz-BRIDGE%20Final%20Report.pdf.

[8] Robert L. Wathen, “Genesis of a generator--The early history of the magnetron,” *Journal of the Franklin Institute,* vol. 255, no. 4, pp. 271-287, 1953.

[9] Russell H. Varian, and Sigurd F. Varian, “A High Frequency Oscillator and Amplifier,” *Journal of Applied Physics,* vol. 10, pp. p.321-327, 1939.

[10] Shulim E. Tsimring, *Electron beams and microwave vacuum electronics*: John Wiley and Sons, 2007, pp. 298.

[11] A. Kupiszezwki., *The Gyrotron: A High Frequency Microwave Amplifier*, R. F. a. M. S. Section, 1979.

[12] R. Mitra, *Microwave Semiconductor Devices*: Prentice-Hall Of India Pvt. Ltd., 2004.

[13] P. F. Moulton, “Spectroscopic and laser characteristics of Ti:Al2O3,” *J. Opt. Soc. Am.*, no. B 3, pp. 125-133, 1986.

[14] J. Shikata, K. Kawase, K. Karino, T. Taniuchi, and H. Ito, “Tunable terahertz-wave parametric oscillators using LiNbO3 and MgO:LiNbO3 crystals,” *IEEE Trans. Microw. Theory Tech.,* vol. 48, no. 4, pp. 653-661, 2000.

[15] E. R. Mueller. "Optically-Pumped THz Laser Technology," [July 20, 2011]; www.coherent.com.

[16] M. Mineo, D. Bariou, J. F. David, A. J. Durand, and C. Paoloni, "Backward wave oscillator for THz frequency range based on double corrugation slow-wave structure." 35th International Conference on Infrared, Millimeter, and Terahertz Waves, IRMMW-THz, 2010.

[17] T. Hidaka, S. Matuura, M. Tani, and K. Sakai, "Application of a novel two-longitudinal-mode LD as a source for CW THz wave generation by photomixing." Vertical-Cavity Lasers, Technologies for a Global Information Infrastructure, WDM Components Technology, Advanced Semiconductor Lasers and Applications, Gallium Nitride Materials, Processing, and Devi, pp. 19-20, 1997.

[18] S. Barbieri, J. Alton, S. S. Dhillon, H. E. Beere, M. Evans, E. H. Linfield, A. G. Davies, D. A. Ritchie, R. Kohler, A. Tredicucci, and F. Beltram, “Continuous-wave operation of terahertz quantum-cascade lasers,” *IEEE J. Quantum Elect.,* vol. 39, no. 4, pp. 586-591, 2003.

[19] Marcel J. E. Golay, “Theoretical Consideration in Heat and Infrared Detection, with Particular Reference to the Pneumatic Detector,” *Rev. Sci. Instrum.,* vol. 18, no. 5, pp. 347-356, 1947.

[20] P. L. Richards, “Bolometers for infrared and millimeter waves,” *J. Appl. Phys.,* vol. 76, no. 1, pp. 1, 1994.

[21] Q. Wu, P. Campbell, X. C. Zhang, and L. Libelo, "Ultrafast electro-optic field sensors for terahertz beams." Lasers and Electro-Optics, pp. 85, 1996.

[22] J. Darmo, and K. Unterrainer, "Electro-optic field and power detector of a new generation." 35th International Conference on Infrared Millimeter and Terahertz Waves (IRMMW-THz), pp. 1-1, 2010.

[23] S. Winnerl, F. Peter, S. Nitsche, A. Dreyhaupt, O. Drachenko, H. Schneider, M. Helm, and K. Kohler, "Large-area photoconductive terahertz detectors." Joint 32nd International Conference on Infrared and Millimetre Waves, and 15th International Conference on Terahertz Electronics, IRMMW-THz, pp. 740-741, 2007.

[24] M. C. Kemp, P. F. Taday, B. E. Cole, J. A. Cluff, A. J. Fitzgerald, and W. R. Tribe, "Security applications of terahertz technology," *Proceedings of SPIE - The International Society for Optical Engineering.* Terahertz for Military and Security Applications, pp. 44-52, 2003.

[25] M. C. Kemp, "A review of millimetre-wave and terahertz technology for detection of concealed threats." 33rd International Conference on Infrared, Millimeter and Terahertz Waves. IRMMW-THz, pp. 1-2, 2008.

[26] M. C. Kemp, "Millimetre wave and terahertz technology for detection of concealed threats - a review." Joint 32nd International Conference on Infrared and Millimeter Waves and the 15th International Conference on Terahertz Electronics. IRMMW-THz, pp. 647-648, 2007.

[27] P. U. Jepsen, D. G. Cooke, and M. Koch, “Terahertz spectroscopy and imaging - Modern techniques and applications,” *Laser and Photonics Reviews,* vol. 5, pp. 124-166, 2011.

[28] M. Hangyo, T. Nagashima, and S. Nashima, “Spectroscopy by pulsed terahertz radiation,” *Measurement Science and Technology,* vol. 13, pp. 1727-1738, 2002.

[29] "TSA Frequently asked questions on using full body scanners using millimeter waves and xray backscattering," [July 20, 2011]; http://www.tsa.gov/approach/tech/ait/faqs.shtm.

[30] Colin Baker, William R. Tribe, Thomas Lo, Bryan E. Cole, Simon Chandler, and Michael C. Kemp, "People screening using terahertz technology," *Proceedings of SPIE - The International Society for Optical*

Engineering. Terahertz for Military and Security Applications III, pp. 1-10, 2005.

[31] M. Oshman, and S. Harris, “Theory of optical parametric oscillation internal to the laser cavity,” *IEEE Journal of Quantum Electronics,* vol. 4, no. 8, pp. 491-502, 1968.

[32] S. Hayashi, K. Maki, C. Otani, and K. Kawase, "Terahertz wave parametric sources," *Proceedings of SPIE - The International Society for Optical Engineering.* Topical Problems of Nonlinear Wave Physics, 2005.

[33] K. Kawase, H. Hoshina, A. Iwasaki, Y. Sasaki, and T. Shibuya, “Mail screening applications of terahertz radiation,” *Electronics Letters,* vol. 46, no. 26, pp. s66-s68, 2010.

[34] D.L. Woolard, W.R. Loerop, and M. Shur, *Terahertz Sensing Technology: Electronic devices and advanced systems technology*: World Scientific, 2003.

[35] McIntosh, Brown, Nichols, McMahon, DiNatale, Lyszczarz, and “Terahertz photomixing with diode lasers in low-temperature-grown GaAs,” *Appl. Phys. Lett,* vol. 67, no. 3844, 1995.

[36] M. R. Hofmann, M. Scheller, C. Brenner, K. Baaske, and M. Koch, "Cost-effective THz spectroscopy with continuous-wave laser sources."

Proceedings of the Fourth European Conference on Antennas and Propagation (EuCAP), pp. 1-4, 2010.

[37] William R. Tribe, David A. Newnham, Philip F. Taday, and Michael C. Kemp, “Hidden object detection: Security applications of terahertz technology,” *P. Soc. Photo-opt. Ins.,* vol. 5354, pp. 168-176, 2004.

[38] Megan R. Leahy-Hoppa, Michael J. Fitch, and Robert Osiander, “Terahertz spectroscopy techniques for explosives detection,” *Chem. & Mat. Sci.*, no. 395, pp. 247-248, 2009.

[39] Hai-Bo Liu, Hua Zhong, Nicholas Karpowicz, Yunqing Chen, and Xi-Cheng Zhang, “Terahertz Spectroscopy and Imaging for Defense and Security Applications,” *Proc. IEEE,* vol. 95, no. 8, 2007.

[40] D. J. Cook, B. K. Decker, G. Maislin, and M. G. Allen, "Through container THz sensing: applications for explosives screening," *Proc. SPIE - Int. Soc. Opt. Eng. (USA).* Terahertz and Gigahertz Electronics and Photonics III, pp. 55-62, 2004.

[41] J. F. Federici, B. Schulkin, F. Huang, D. Gary, R. Barat, F. Oliveira, and D. Zimdars, “THz imaging and sensing for security applications-explosives, weapons and drugs,” *Semicond. Sci. Tech.,* vol. 20, pp. S266-S280, 2005.

[42] J. S. Melinger, S. S. Harsha, N. Laman, and D. Grischkowsky, “Guided-wave terahertz spectroscopy of molecular solids,” *Journal of the Optical Society of America B (Optical Physics),* vol. 26, pp. A79-A89, 2009.

[43] Nathan Argaman, and Guy Makov, “Density Functional Theory -- an introduction,” *American Journal of Physics* vol. 68, pp. 69-79, 2000.

[44] N. M. Harrison. "An Introduction to Density Functional Theory," [Aug 10,, 2011]; http://www.engr.ucsb.edu/~mjgordon/courses/che240a/intro-to-dft.pdf.

[45] M.J. Frisch. "Gaussian 03 (Revision B.05), Gaussian Inc," [August 17, 2003]; http://www.gaussian.com/.

[46] Gordon-Research. "General Atomic and Molecular Electronic Structure System Software," [Aug 10, 2011]; http://www.msg.ameslab.gov/gamess/.

[47] Damian G. Allis, and Timothy M. Korter, “Theoretical Analysis of the Terahertz Spectrum of the High Explosive PETN,” *ChemPhysChem,* vol. 7, no. 11, pp. 2398-2408, 2006.

[48] D. Allis, “First principles analysis of the terahertz spectrum of PETN,” *Proc. SPIE,* vol. 6212, no. 1, pp. 62120F, 2006.

[49] Damian G. Allis, “Development of computational methodologies for the prediction and analysis of solid-state Terahertz spectra ” *International*

Journal of High Speed Electronics and Systems, vol. 17 no. 2, pp. 193-212, 2007.

[50] Damian G. Allis, Darya A. Prokhorova, and Timothy M. Korter, "Solid-State Modeling of the Terahertz Spectrum of the High Explosive HMX," *The Journal of Physical Chemistry A,* vol. 110, no. 5, pp. 1951-1959, 2006.

[51] Damian G. Allis, J. Axel Zeitler, Philip F. Taday, and Timothy M. Korter, "Theoretical analysis of the solid-state terahertz spectrum of the high explosive RDX," *Chemical Physics Letters,* vol. 463, no. 1-3, pp. 84-89, 2008.

[52] B. Delley, "Density functional study of iron(II)-porphine," *Physica B: Condensed Matter,* vol. 172, no. 1-2, pp. 185-193, 1991.

[53] W. H. Fan, A. Burnett, P. C. Upadhya, J. Cunningham, E. H. Linfield, and A. G. Davies, "Far-infrared spectroscopic characterization of explosives for security applications using broadband terahertz time-domain spectroscopy," *Applied Spectroscopy,* vol. 61, pp. 638-643, 2007.

[54] D. Steele, *Theory of vibrational spectroscopy*: W.B. Saunders, 1971.

[55] P. Gans, *Vibrating molecules*: Chapman and Hall, 1971.

[56] S. Califano, *Vibrational states*: Wiley, 1976.

[57] Brian C. Smith, *Fundamentals of Fourier Transform Infrared Spectroscopy*: CRC Press LLC, 1996.

[58] Daniel Mittleman, *Sensing with Terhertz Radiation*, Berlin/DE: Springer-Verlag Berlin and Heidelberg GmbH & Co. KG, 2010, pp. 40-43.

[59] O. Esenturk, and E. J. Heilweil, "Ultrafast transient THz spectroscopy of azobenzene." The Joint 30th International Conference on Infrared and Millimeter Waves and 13th International Conference on Terahertz Electronics, pp. 479-480, 2005.

[60] Peter Griffiths, and James A. De Haseth, *Fourier Transform Infrared Spectrometry*, 2nd ed ed.: Wiley-Interscience, 2007.

[61] Helmut Gunzler, and Hans-Ulrich Gremlich, *IR Spectroscopy: An Introduction*: Wiley-VCH, 2002.

[62] David Jeffery Griffiths, *Introduction to quantum mechanics*, 2nd ed. ed.: Pearson Prentice Hall, 2005.

[63] Anthony C. Phillips, *Introduction to quantum mechanics*: Wiley, 2003.

[64] Shuji Ye, Kenichi Tonokura, and Mitsuo Koshi, “Vibron dynamics in RDX, β-HMX and Tetryl crystals,” *Chemical Physics,* vol. 293, no. 1, pp. 1-8, 2003.

[65] Bohren, and Huffman, *Absorption and Scattering of Light by Small Particles*: Wiley, 1983.

[66] J. E. Bjarnason, T. L. J. Chan, A. W. M. Lee, M. A. Celis, and E. R. Brown, "Millimeter-wave, terahertz, and mid-infrared transmission through common clothing," *Applied Physics Letters,* vol. 85, no. 4, 2004.

[67] Charles R. Dietleina, Jon E. Bjarnasonb, Erich N. Grossmanb, and Zoya Popovića, "Absorption, transmission, and scattering of expanded polystyrene at millimeter-wave and terahertz frequencies," *Proc. of SPIE* vol. 6948, no. 69480E, 2008.

[68] *Firefly-THz High Power, Widely Tunable Pulsed Terahertz Laser Operator Manual Version 1.3*, 2010.

[69] A. Yariv, and W. Louisell, "5A2--Theory of the optical parametric oscillator," *IEEE Journal of Quantum Electronics,* vol. 2, no. 9, pp. 418-424, 1966.

[70] J. Falk, J. Yarborough, and E. Ammann, "Internal optical parametric oscillation," *IEEE Journal of Quantum Electronics* vol. 7, no. 7, pp. 359-369, 1971.

[71] B. P. Lathi, *Signal Processing & Linear Systems*: Oxford University Press, 2001.

[72] Julius Smith, *Mathematics of the Discrete Fourier Transform (DFT) with Audio Applications, Second Edition*: W3K Publishing, 2007.

[73] Hall, Vrabec, Dowling, and "A high-resolution, far infrared double-beam lamellar grating interferometer," *Appl. Opt.,* vol. 5, pp. 1147–58, 1966.

[74] John Strong, and G A Vanasse, "A Lamellar-grating far-infrared interferometer," *J. Opt. Soc. Am,* vol. 50 no. 113-8, 1960.

[75] Heribert Eisele, Mira Naftaly, and John R Fletcher, "A simple interferometer for the characterization of sources at terahertz frequencies," *Meas. Sci. Technol.,* vol. 18, pp. 2623–2628, 2007.

[76] Henry, and Tanner, "A lamellar grating interferometer for the far-infrared," *Infrared Phys.,* vol. 19 pp. 163-74, 1979.

[77] "Arduino Duemilanove Microcontroller Documentation," [July 10, 2011]; http://www.arduino.cc/.

[78] "Global Security website: Composition of Explosives.," [July 2, 2011]; http://www.globalsecurity.org/military/systems/munitions/explosives-compositions.htm.

[79] "OriginLab graphing and data analysis software," [Aug 10, 2011]; http://www.originlab.com/.

[80] D. H. Auston, “Picosecond optoelectronic switching and gating in silicon,” *Applied Physics Letters,* vol. 26, no. 3, pp. 101-103, 1975.

[81] J. Zhang, Y. Hong, S. L. Braunstein, and K. A. Shore, “Terahertz pulse generation and detection with LT-GaAs photoconductive antenna,” *IEEE Proceedings on Optoelectronics,* vol. 151, no. 2, pp. 98-101, 2004.

[82] P. C. M. Planken, Nienhuys Han-Kwang, H. J. Bakker, and T. Wenckebach, “Measurement and calculation of the orientation dependence of terahertz pulse detection in ZnTe,” *Journal of the Optical Society of America B Optical Physics,* vol. 18, pp. 313-317, 2001.

[83] Jonathan F. Holzman, “Ultrafast Photonic Applications for Terahertz Waveform Generation,” PhD, Thesis, Univerisity of Alberta, 2003.

[84] Richard T. Hall, Dale Vrabec, and Jerome M. Dowling, “A High-Resolution, Far Infrared Double-Beam Lamellar Grating Interferometer,” *Appl. Opt.,* vol. 5, no. 7, pp. 1147-1158, 1966.

[85] A.L Aseev, D.G. Esaev, and M.A. Dem'yanenko, “Terahertz Imaging and Radioscopy with 160x120 Microbolometer 90 FPS Camera,” in Free Electron Lasers Conference, Novosibirsk, Russia, 2007.

[86] M. Bolduc, L. Marchese, B. Tremblay, M. Doucet, M. Terroux, H. Oulachgar, L. Le Noc, C. Alain, H. Jerominek, and A. Bergeron, "Video-rate THz imaging using a microbolometer-based camera." 35th International

Conference on Infrared, Millimeter, and Terahertz Waves, IRMMW-THz, 2010.

[87] Paul Dietz, William Yerazunis, and Darren Leigh, “Very Low-Cost Sensing and Communication Using Bidirectional LEDs,” *Mitsubishi electric research laboratories*, 2003.

[88] Burr-Brown. "IVC102 Integrating Amplifier Datasheet," [July 2, 2011]; http://focus.ti.com/lit/ds/symlink/ivc102.pdf.

[89] "Processing: Open source programming development environment," [July 2, 2011]; http://processing.org/.

[90] R.M. Woodward, V.P. Wallace1, D.D. Arnone, and E.H. Linfield and M. Pepper, “Terahertz Pulsed Imaging of Skin Cancer in the Time and Frequency Domain,” *Journal of Biological Physics,* vol. 29, no. 2-3, 2003.

Appendices

APPENDIX A

Photographs of Lamellar Split Mirror

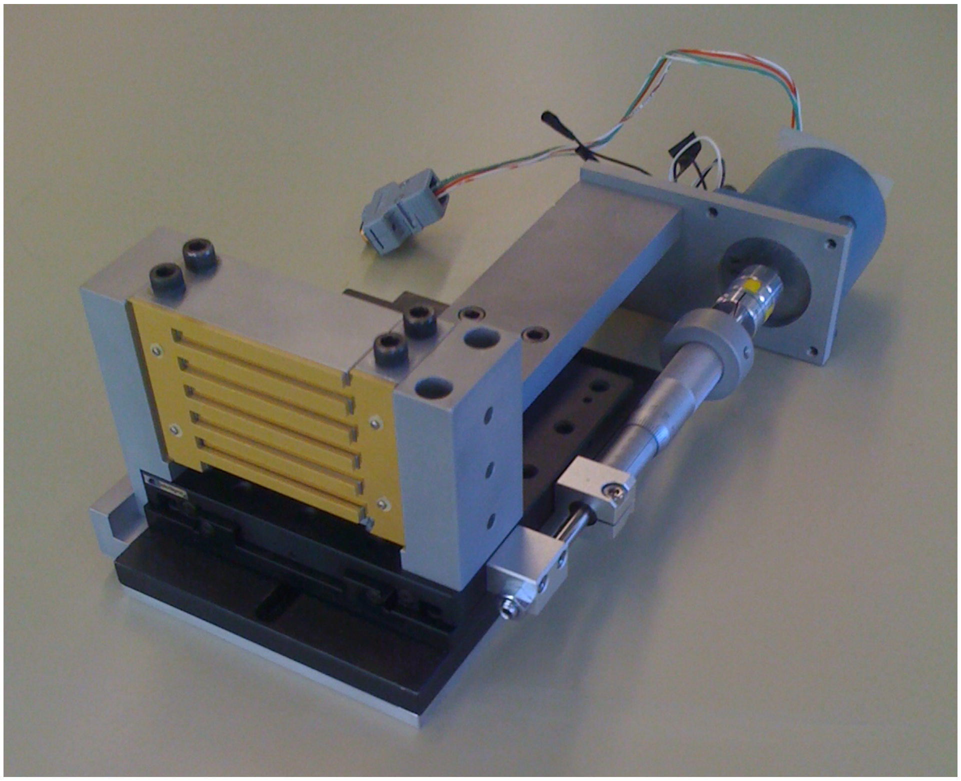

Figure A1: View of the lamellar split mirror interferometer

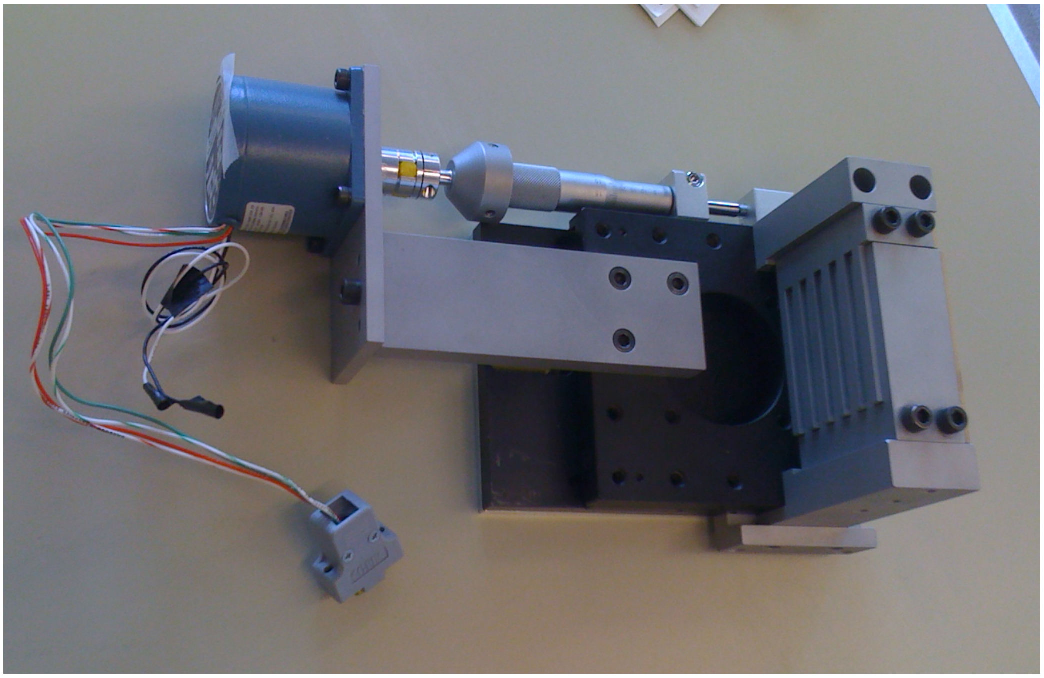

Figure A2: Rear view of lamellar split mirror interferometer

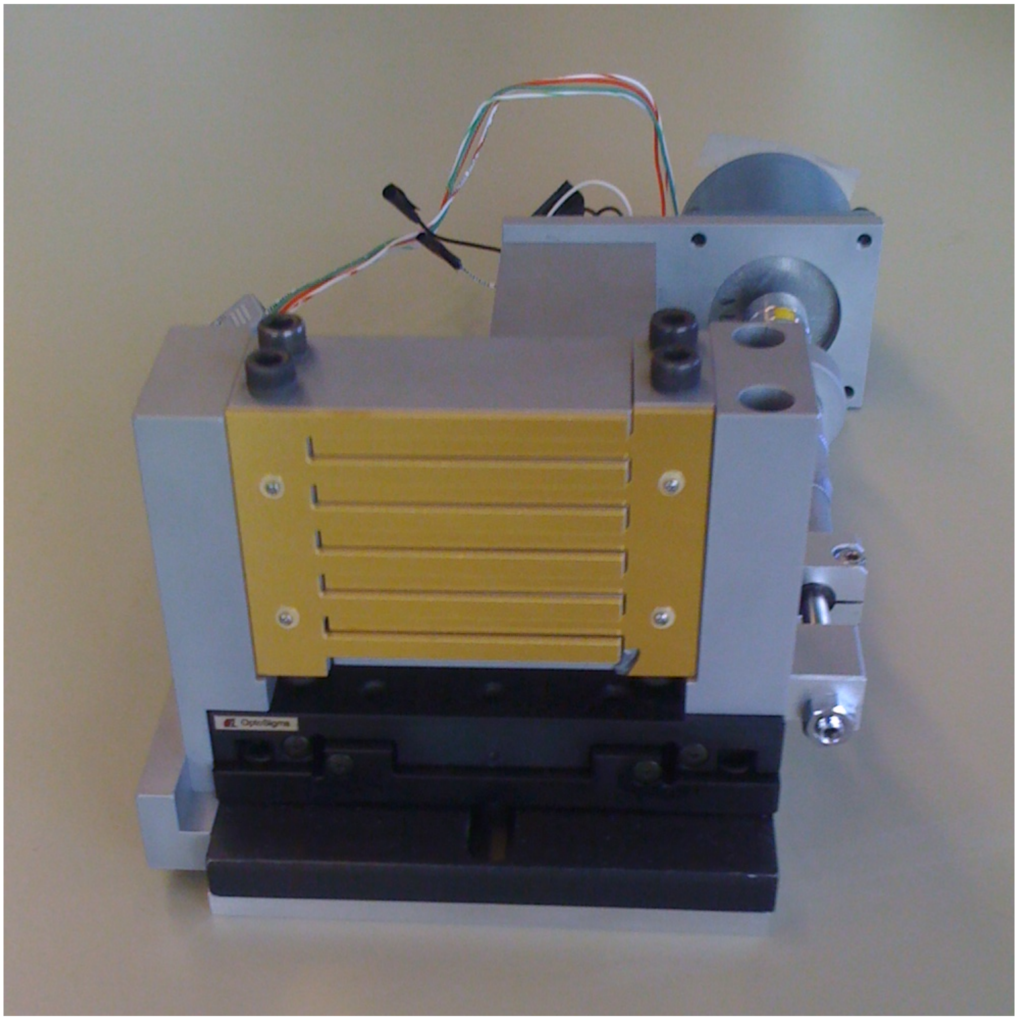

Figure A3: Frontal view of lamellar split mirror interferometer.

APPENDIX B

Multiplexing program for PIC16 microchip design

```
	Title "PIC16multiplex"
;;; *****************************************************************
;;; Filename:	PIC15multiplex.asm
;;; Purpose:	Multiplexing and Analog to Digital conversion for Raster scanning pixel
;;; detection camera
;;; Date: June 2010
;;; Author:	Michael Startsev
;;; *****************************************************************
;;; Revision History: 1.0
;;;
;;; *****************************************************************


	list				; Turn on list output.

	;; Include register, bit, and other info specific to
	;; the specified device.
	ifdef	__16F873
	#include <p16f873.inc>
	messg "Assembling for PIC16F873."
	endif
	ifdef	__16F874
	#include <p16f874.inc>
	messg "Assembling for PIC16F874."
	endif
	ifdef	__16F876
	#include <p16f876.inc>
	messg "Assembling for PIC16F876."
	endif
	ifdef	__16F877
	#include <p16f877.inc>
	messg "Assembling for PIC16F877."
	endif
	ifdef	__16F873A
	#include <p16f873a.inc>
	#define A_Device
	messg "Assembling for PIC16F873A."
	endif
	ifdef	__16F874A
	#define A_Device
	#include <p16f874a.inc>
```

```
          messg "Assembling for PIC16F874A."
          endif
          ifdef     __16F876A
          #define A_Device
          #include <p16f876a.inc>
          messg "Assembling for PIC16F876A."
          endif
          ifdef     __16F877A
          #define A_Device
          #include <p16f877a.inc>
          messg "Assembling for PIC16F877A."
          endif


;;; ---------------------------------------------------------------
;;; Assembler Equates Section.  Define assembly-time constants here
;;;                             using the EQU assembler directive.
;;;       eg)  DEBUGGING EQU  1
;;; ---------------------------------------------------------------
;**** CONFIGURED BIT DEFINITIONS
CTS_PIN             EQU    0x02     ; On Port B
RTS_PIN             EQU    0x01     ; On Port B
Tx_PIN      EQU     0x06    ; On Port C
Rx_PIN              EQU    0x07     ; On Port C

;** General
BANK0               EQU    0x0000 ; Data Memory start positions
BANK1               EQU    0x0080
BANK2               EQU    0x0100
BANK3               EQU    0x0180

PAGE0       EQU     0x0000 ; Program Memory start positions
PAGE1       EQU     0x0800

;;; ----------------------------------------------------------------
;;; Variable Address Assignments.
;;; ----------------------------------------------------------------
          UDATA                      ; Start of uninitialized data section.
                              ; Reserve memory for variables using the
                              ; "RES" directive here.  Note that the
                              ; linker will assign addresses.
                              ; eg)  ADcounter  res  1
                              ;      (reserves 1 byte for ADcounter).
                              ; variable in RAM for context saving

Column       res     1        ; reserve 1 byte for column variable
maxcolumn    res     1        ; reserve for x dimension variable of matrix
Row          res     1        ; reserve 1 byte for row variable
maxrow       res     1        ; reserve for y dimension variable of matrix
```

```
diffrow         res     1
diffcolumn      res     1
EXAMPLE         res     1       ; variable in access RAM

        UDATA_ACS

        UDATA_OVR               ; Uninitialized data overlay section.
                                ; Upon occasion, temporary variables
                                ; can be over-written by other temporary
                                ; variables.  These would appear here.
                                ; BUT!  If you ever intend on time-sliced
                                ; or pre-emptive multitasking
                                ; don't *ever* use this directive!

        UDATA_SHR               ; Uninitialized data shared section.
                                ; Variables that appear here appear
                                ; across all banks, meaning that no
                                ; bank selection will be required.
Delay1          res     1       ; reserve 1 byte for the variable Delay1
Delay2          res     1       ; reserve 1 byte for the variable Delay2
Delay3          res     1
Delay4          res     1
Delay5          res     1
Delay6          res     1

dataL           res     1       ; startup timer delay


;;; ------------------------------------------------------------------
;;; Establish the OPTION register bit values.
;;; ------------------------------------------------------------------
;;; The '__CONFIG' directive is used to embed PIC configuration data
;;; within an assembly file. The labels following the directive
;;; are located in the .inc file.  See the device data sheet for
;;; additional information on the configuration word.
        ifndef A_Device
        __CONFIG _CP_OFF & _WDT_OFF & _BODEN_ON & _PWRTE_ON &
_HS_OSC & _WRT_ENABLE_ON & _LVP_OFF & _CPD_OFF
        endif
;;; _CP_OFF:    turn off code protection.  Don't change this unless you
;;;             want a device that can never be programmed again.  This
;;;             is a "bug" in some PIC devices.
;;; _WDT_OFF:turn off the watchdog timer.
;;; _BODEN_ON:          turn on power brown-out reset.
;;; _PWRTE_ON:          turn on power-up timer.
;;; _HS_OSC:    specify that the device is using an HS oscillator for 20MHz, use XT for
;;;4MHz.
;;; _WRT_ENABLE_ON:  enable writing to data EEPROM.
;;; _LVP_OFF:  disable low-voltage in-circuit programming.
```

```
;;; _CPD_OFF:  disable data EEPROM write protection.

        ifdef A_Device
        messg "A revision device."
         __CONFIG _CP_OFF & _WDT_OFF & _BODEN_ON & _PWRTE_ON &
_HS_OSC & _WRT_OFF & _LVP_OFF & _CPD_OFF
endif

;;; _CP_OFF:    turn off code protection.  Don't change this unless you
;;;          want a device that can never be programmed again.  This
;;;          is a "bug" in some PIC devices.
;;; _WDT_OFF:turn off the watchdog timer.
;;; _BODEN_ON:        turn on power brown-out reset.
;;; _PWRTE_ON:        turn on power-up timer.
;;; _XT_OSC:   specify that the device is using an XT oscillator. (we use HS for 20MHz)
;;; _WRT_OFF:disable write-protection of program FLASH.
;;; _LVP_OFF:  disable low-voltage in-circuit programming.
;;; _CPD_OFF:  disable data EEPROM write protection.


Reset:  CODE  0x0000
        pagesel Main            ; Selects page of program memory with.
        goto    Main            ; the actual program, then goes to it.

;;; ------------------------------------------------------------------
;;; Main Program.
;;; ------------------------------------------------------------------
        CODE                    ; Start of the code section.

        org     0x004

Main:
;;;;;   initializeChip          ; Set all Pins to output (low) (high impedence)

        banksel BANK0                   ; Move to Bank 0
        clrf            PORTA                   ; Clear Port A
        clrf            PORTB           ; Clear Port B
        clrf            PORTC           ; Clear Port C

        banksel BANK1                   ; Move to Bank 1


        clrf            TRISA           ; Set Port A to digital out
        clrf            TRISB           ; Set Port B to digital out (column coordinate)
        clrf            TRISC           ; Set Port C to digital out (row coordinate)

        banksel BANK0                   ; Move to Bank 0
        clrf            ADCON0          ; Shutoff all ADC function and set available
                                        ;  channel to AN0
```

```
        banksel TRISA
        movlw           B'00000001'     ; set input pin for ANO analog input and AN1 as
                                                ;output for integrating
        movwf           TRISA           ; amplifier synchronization
        banksel PORTB
        clrf            PORTB           ; Clear Port B
        clrf            PORTC           ; Clear Port C


        banksel PORTD
        CLRF            PORTD                   ;clear Port D
        banksel TRISD
        CLRF            TRISD           ; set PORT D to output the digital conversion of
        the                                     ;analog signal
;;;;;;;;;;

        banksel ADCON1
        MOVLW           B'00001110'     ; ADCON1 setup: VSS,VDD ref. AN0 analog
        only.                                   ; Left justified
        MOVWF           ADCON1

        banksel ADCON0
        movlw           B'01000000'     ; TAD is 8TOSC to make conversion 1.6 us
        movwf           ADCON0          ; set ADCON0 to select channel RA0 (AN0)


        BSF             ADCON0,ADON             ; Enable A/D Conversion Module

Initialize
        banksel maxcolumn
        movlw           D'8'                    ; assign square dimensions to working
                                                ; register for 8*10 matrix
        movwf           maxcolumn               ; assign x max
        movlw           D'5'
        movwf           maxrow                  ; assign y max
        clrf            Column                  ; initialize column counter to zero
        clrf            Row                     ; initialize row counter to zero


InitializeUART:

        banksel BANK0                           ; Set to bank0
        bcf             PORTC,Tx_PIN            ; Initial condition for the Tx line
        bcf             PORTC,Rx_PIN            ; Initial condition for the Rx line

        banksel BANK1                   ; Set to bank1
        bsf             TRISC,Tx_PIN ;  set Rx and Tx Pins to default as
        bsf             TRISC,Rx_PIN ;  high impedance
```

```
        bcf             PIE1,RCIE       ; Disable uart interrupts
        bcf             PIE1,TXIE

                                ; Set baud Rate to one of the following
        movlw           D'20'   ; 0x19 for 9600 baud 4MHz, D'129' for 20Mhz

        movwf           SPBRG

        movlw  b'00100100'      ; brgh = high
        movwf  TXSTA            ; enable Async Transmission, set brgh

        banksel BANK0           ; Set to bank0

        movlw  b'10010000'      ; enable Async Reception
        movwf  RCSTA

PicALIVE
; This portion first tests if controller chip is working by sending a message stating that
; the chip is "alive" through Serial communication terminal
; -----------------------------------
; PROVIDE A SETTLING TIME FOR START UP
; -----------------------------------
;
      clrf dataL
settle  decfsz dataL,F
      goto settle

      movf RCREG,W
      movf RCREG,W
      movf RCREG,W           ; flush receive buffer
;
; ---------
; MAIN LOOP
; ---------
;
      call message           ; send "16F877 alive"
loop    call receive         ; wait for a char
      call send              ; send the char
      goto MainLoop                          ;(originally: goto loop)
;
; -----------------------------------------
; RECEIVE CHARACTER FROM RS232 AND STORE IN W
; -----------------------------------------
; This routine does not return until a character is received.
;
receive
                clrw
                btfsc PIR1,RCIF         ; (5) check for received data
```

```
    goto Stopfunction                  ; if data recieved, stop the multiplex function
                                       ; so no value is sent to txreg

    return


; ---------------------------------------------------------
; STOP SENDING UART ANALOG TO DIGITAL INFORMATION (STOP
FUNCTION)
; ---------------------------------------------------------
Stopfunction
        movf RCREG,W            ; save received data in W (not sent)
                call stopmessage
Stopfunctionloop
                btfss PIR1,RCIF
                goto    Stopfunctionloop

                clrf    RCREG
                return

;
; ---------------------------------------------------------
; SEND CHARACTER IN W VIA RS232 AND WAIT UNTIL FINISHED SENDING
; ---------------------------------------------------------
;
send    movwf TXREG             ; send data in W

TransWt bsf STATUS,RP0          ; RAM PAGE 1
WtHere  btfss TXSTA,TRMT        ; (1) transmission is complete if hi
    goto WtHere

    bcf STATUS,RP0          ; RAM PAGE 0
    return
;
; -------
; MESSAGE
; -------
;
message movlw  '1'
    call send
    movlw  '6'
    call send
    movlw  'F'
    call send
    movlw  '8'
    call send
    movlw  '7'
    call send
    movlw  '7'
```

```
        call send
        movlw  ' '
        call send
        movlw  'a'
        call send
        movlw  'l'
        call send
        movlw  'i'
        call send
        movlw  'v'
        call send
        movlw  'e'
        call send
        movlw  0x0D ; CR
        call send
        movlw  0x0A ; LF
        call send
        return

; ------------
; STOP MESSAGE
; ------------

stopmessage
        movlw  '1'
        call send
        movlw  '6'
        call send
        movlw  'F'
        call send
        movlw  '8'
        call send
        movlw  '7'
        call send
        movlw  '7'
        call send
        movlw  ' '
        call send
        movlw  'i'
        call send
        movlw  's'
        call send
        movlw  ' '
        call send
        movlw  't'
        call send
        movlw  'i'
        call send
        movlw  'r'
```

```
	call send
	movlw  'e'
	call send
	movlw  'd'
	call send
	movlw  0x0D ; CR
	call send
	movlw  0x0A ; LF
	call send
	return


; --------------------
; MULTIPLEXING PROGRAM
; --------------------
; Scan through the Pixels of the camera and read a signal

MainLoop:
		movfw		Column;output the column coordinate out of Port B bits
		movwf		PORTB
		movfw		Row		; output the Row Coordinate out of Port C bits
		movwf		PORTC


AmplifyDelay:	;delay here to allow for signal to reach the A/D converter
		bsf		PORTD, 0	; open S2 on Amplifer to allow for time
integration amplification
		movlw	D'3'	;create delay of 100us
		movwf	Delay1
		nop
		movlw	D'2'
		movwf	Delay2
		movlw	D'1'
		movwf	Delay3
		call	superdelay

		banksel ADCON0
		BSF		ADCON0,GO_DONE	; Start A/D Conversion
		BTFSC ADCON0,GO_DONE
		GOTO $-1
		movfw	ADRESH



Uartpixel
		bsf STATUS,RP0		; RAM PAGE 1
UARTpixelloop
		btfss TXSTA,TRMT			; transmission is complete if hi
		goto UARTpixelloop
```

```
        bcf     STATUS,RP0                      ; RAM PAGE 0
        movwf   TXREG                           ; output through UART module

Amplifiersync
        banksel PORTD
        bcf             PORTD, 0        ; set the AN1 bit to low (S2 = 0v) in order to
close the circuit (reset)
Resetdelay:                             ; need 10us to reset the charge in amplifier
        banksel Delay1
        movlw           D'35'           ; allow all the charge to dissipate in 10us  (D'17')
        movwf           Delay1
        call            Delay


Changecolumn:
        incf    Column, 1       ; count value is increased and placed in Column again.

; minisuperdelay to slow program. Only use to debug

;       call    minisuperdelay
        movf    Column, w               ; compare column coordinate to maximum
        subwf   maxcolumn, 0            ; subtract w from maxcolumn and store in w
        movwf   diffcolumn
        nop                             ; pause required for processing
        incf    diffcolumn, 1           ; must add one pixel since decfsz function skips
        decfsz  diffcolumn, 0           ; (skip next instruction if maxcolumn minus
                                        ; column = 0)
        goto    MainLoop                ; if column not at max, go back to analog read
loop


Changerow:                      ; shift to the next row and reset column to zero
        incf    Row, 1          ; increase row, store in row
        clrf    Column
        movf    Row,W           ; compare maximum row value with current Row value
                                ; if row at max
        subwf   maxrow, 0
        movwf   diffrow
        nop
        incf    diffrow, 1
        decfsz  diffrow, 0      ;skip next instruction if maxrow minus Row = 0)

        goto    MainLoop        ;back to analog reading loop
        call    Completedframe
        goto    loop            ;temporary system for input output.
Completedframe:
        clrf    Row                     ;clear row (we have finished frame)
```

```
;;;;;; SUPERDELAY segment would linger on 16th column 16th row
superdelayset

;          movlw  0xff         ;for long delay (pixel light watching)
           movlw  D'5'
           movwf  Delay1
           movwf  Delay2
           movlw  0x01              ; for pixel watching (us 0x30)
           movwf  Delay3
           call      superdelay
           return


Delay:
           DECFSZ  Delay1,1 ;Decrement Delay1 by 1, skip next instruction if Delay1 is 0
           GOTO  Delay

           Return
;******************************************************************
*******
;End of program

           ;; Don't let execution fall down to here, otherwise the
           ;; subroutines (or whatever follows) will be executed without
           ;; parameters, and chaos reigns when a "return" instruction
           ;; executes with no return address on the stack.

;;; -----------------------------------------------------------------
;;; Application-specific Subroutines.
;;; -----------------------------------------------------------------
;;;inbetween delays

minisuperdelay:            ; this is not used during reading operation
           movlw  0xff
           movwf  Delay1
           movwf  Delay2
           movlw  0x03
           movwf  Delay3
           goto      superdelay
           return

;;;;;;;;;;;;;;;;;;;;;;;;;;superdelay;;;;;;;;;;;;;;;;;;;;
; this is used to create delay for integration of current
superdelay:
           DECFSZ  Delay1,1 ;Decrement Delay1 by 1, skip next instruction if Delay1 is 0
           GOTO  superdelay
           DECFSZ              Delay2,1          ; extra delay if needed
           GOTO superdelay
           DECFSZ  Delay3,1 ;Decrement Delay1 by 1, skip next instruction if Delay1 is 0
```

```
        GOTO  superdelay
        return



;;; ------------------------------------------------------------------
;;; Code-section Constant Data.
;;; ------------------------------------------------------------------


;;; -------------------------------------------------------------------
;;; Vectors Section.
;;; -------------------------------------------------------------------
;;; Establish the reset vector.  Note that the "0x0000" after the CODE
;;; directive ensures that the linker places the code at program memory
;;; location 0x0000.


        END
```

APPENDIX C

Multiplexing Program for Arduino Microchip
Title: “linear_multiplex.pde”

This program uses the Arduino Java environment to instruct the multiplexing action of the prototype circuit. For reading the signal from the analog to digital converter, see the next section : “Processing code”

```
/*
  Analog to digital conversion of signal received from matrix of LEDs

 * LED anode (long leg) attached to digital output 13
 * LED cathode (short leg) attached to ground

 •   Note: because most Arduinos have a built-in LED attached
 to pin 13 on the board, the LED is optional.

 */

int maxrow = 3;      //define size of LED array (originally 8)
int maxcolumn = 2;  //originally 10

unsigned int ot[3][2];        //output variable

int sensorPin = 0;    // select the input pin for the potentiometer
int ledPin = 13;      // select the pin for the LED
int sensorValue = 0;  // variable to store the value coming from the sensor

int switchPin = 13;

void setup() {
  // declare the ledPin as an OUTPUT:
  pinMode(ledPin, OUTPUT);
  //declare multiplexing pins
  pinMode(2, OUTPUT);
  pinMode(3, OUTPUT);
  pinMode(4, OUTPUT);
  pinMode(5, OUTPUT);

  pinMode(8, OUTPUT);
  pinMode(9, OUTPUT);
  pinMode(10, OUTPUT);
  pinMode(11, OUTPUT);
    Serial.begin(9600);
}
```

```
void loop() {


 for (int column = 0; column <= maxcolumn-1;){
  transferToColumnPins(column);      //assign the column access in array
  for (int rowSel = column*maxrow; rowSel <= column*maxrow+maxrow-1;){
   transferToRowPins(rowSel);

   int row=rowSel-column*maxrow;            //determines actual row for the serial signal

   digitalWrite(switchPin, LOW);         //Low closes circuit and drains charge
   delayMicroseconds(10);               //sufficient to drain charge
   digitalWrite(switchPin, HIGH);       //Open circuit allows to build voltage
   delayMicroseconds(100);              //build up voltage for 100 microseconds

   // read the value from the sensor:
   ot[row][column]=analogRead(sensorPin);

  //Serial.println(analogRead(sensorPin));     read them all together instead
      //   delay(10);    //delay to stabilize signal milliseconds
        rowSel++;
  }

  column++;
 }

 //allow pause where there is no LED accessed choose 8 since unaccessed

  transferToColumnPins(8);
  transferToRowPins(8);
  // turn the ledPin off:
 digitalWrite(switchPin,LOW);
 delay(20);    //set for 2000 for observing LEDs

// delayMicroseconds(10);

//Send data across serial port
  if(Serial.available()>0){
   print_ot();
  }
}


/************************** FUNCTIONS*************************/

//set a function to convert an interger counted to a binary output on pins
void transferToRowPins(int x){
 byte y = 0;
```

```
  y=byte(x);          //converts any data type to byte
  digitalWrite(2,bitRead(y,3));
  digitalWrite(3,bitRead(y,2));
  digitalWrite(4,bitRead(y,1));
  digitalWrite(5,bitRead(y,0));

}
//set a function to convert an interger counted to a binary output on colomn pins
void transferToColumnPins(int x){
  byte y = 0;
  y=byte(x);          //converts any data type to byte
  digitalWrite(8,bitRead(y,0));
  digitalWrite(9,bitRead(y,1));
  digitalWrite(10,bitRead(y,2));
  digitalWrite(11,bitRead(y,3));
}

//Serial output function to display the array
void print_ot(){

  for(int i=0;i<maxrow;i++){
    for(int j=0;j<maxcolumn;j++){
      Serial.print(ot[i][j],DEC);ot[i][j]=0;
      Serial.print(",");
    }
  }
  Serial.println();
  //Serial.read();
}
```

Analog to Digital Reading using Arduino and "Processing"
Title: "Led_Sense_Processing.pde"

This program runs parallel with the above program to read the signal data to the connected computer and display a video image representing the pixels signal received.

```
import processing.serial.*;

Serial port;

PFont font;
int maxcol = 2;
int maxrow = 3;

int [][] x =new int[maxrow][maxcol];
int [][] clip = x;
```

```
void setup(){
  size(200,200);
  font = loadFont("TimesNewRomanPSMT-20.vlw");
  textFont(font,10);
  textAlign(RIGHT);


  //Serial myPort;        // The serial port

 // List all the available serial ports
 println(Serial.list());
 // I know that the first port in the serial list on my mac
 // is always my  Arduino, so I open Serial.list()[0].
 // Open whatever port is the one you're using.
port = new Serial(this, Serial.list()[1], 9600);  //38400
//myPort.clear();
 // don't generate a serialEvent() unless you get a newline character:
 //myPort.bufferUntil('\n');


  //port = new Serial(this,"/dev/tty.usbserial-A6008ieP",38400);
  //port.clear();
  //port.bufferUntil(10);        //
    port.clear();
  port.bufferUntil('\n');
}

void draw(){
  background(120);
  for(int i=0;i<maxrow;i++){
    for(int j=0;j<maxcol;j++){
      text(x[i][j],55+45*j,55+45*i);
      clip[i][j]=x[i][j];
      if (x[i][j] > 255){
       clip[i][j] = 255;
      }
      fill(255-clip[i][j]);
      ellipse(j*45+30,i*45+30,40,40);  // ellipse(x,y,width,height)
    }
  }
}

void serialEvent(Serial port){
  String stringData=port.readStringUntil('\n');
  if(stringData!=null){
    stringData=trim(stringData);              //trim removes whitespace characters
    int data[]=int(split(stringData,','));     //split breaks strings into pieces using
    for(int i=0,k=0;i<maxrow;i++){                //character or string as a divider
```

```
      for(int j=0;j<maxcol;j++){
        x[i][maxcol-1-j]=data[k++];
      }
    }
    port.write(65);    //should this be myPort?
  }
}

void mousePressed(){
  port.write(65);
}
```

APPENDIX D

Spectroscopic Scan Program
Titled: “Spectrumscan.m”

This program reads and writes wavelengths to the Firefly OPO system to instruct the spectroscopic scan procedure.

Note: This program must be in the same directory as the “OscilloscopeRead.m” program described below

```
%Code to scan frequencies in Firefly OPO and collect spectrum data from
%oscilloscope connected to a golay cell


%close all
%clear all
%*****parameters*******
c=299792458; %light speed
pumpwave=1.064170640025218e-006; %merely calculated, should be about 1064e-9;
pumpfreq=c/pumpwave;
Num_of_Averages=3;

%***************Initialize USB interface with Oscilloscope***********
% Create a VISA-USB object.
interfaceObj = instrfind('Type', 'visa-usb', 'RsrcName',
'USB0::0x0699::0x0372::C010455::0::INSTR', 'Tag', '');

% Create the VISA-USB object if it does not exist
% otherwise use the object that was found.
if isempty(interfaceObj)
   interfaceObj = visa('NI', 'USB0::0x0699::0x0372::C010455::0::INSTR');
else
   fclose(interfaceObj);
   interfaceObj = interfaceObj(1);
end

% Create a device object.
% deviceObj = icdevice('tektronix_tds2012.mdd', interfaceObj);
deviceObj = icdevice('DPO4032.mdd', interfaceObj);

set(interfaceObj, 'InputBufferSize', 3000000);
```

```
% Connect device object to hardware.
connect(deviceObj);

%******************initialize Firefly OPO communication**********
dbstop if error
disp(' ');

%Test parameters
ip_address = '192.168.1.111';   % ip_address is the ICEBLOC address
access_port = 9371;                  % port number for ICEBLOC access
temp_file_path = 'C:\M2_temp\';
read_back_flag = 1;
delete_temp_file_flag = 1;
display_flag = 1;
integral = [];



[num,txt,raw] = xlsread('tuningset.xls', 'Sheet1', 'basic');
if strfind(txt[86],'frequency')      %check if first line is frequency
   disp('Thz frequency input converted to wavelength')
   inputthzfreq=num.*10.^12;
   idlerfreq=abs(pumpfreq-inputthzfreq);
    wavelength = (c./(idlerfreq))*10^9 ;  %format in nm units
else
wavelength= num;

end
wavelength = round(wavelength.*100)./100;    %round to acceptable values
freqvector = zeros(size(wavelength));

%******************Connect to TCP******************
try
   tcp_object = tcpip(ip_address, access_port); %connect to Iceblock
   fopen(tcp_object);                  %open connection
catch
   disp('Failed: Couldn''t connect to TCP server');
   return
end
%************************************************
%get ready to start the scan by moving to initial position

fprintf(tcp_object,['WAVELENGTH ', num2str(wavelength(1))]);
pause(0.2);
test= strfind(fscanf(tcp_object), 'OK');
if isempty(test)
   disp('Failed to upload instruction')
else
   disp('Initializing Motor, Please Wait')
```

```
   pause(20);         % Pause to allow for motor to reach destination
end

for n=1:length(wavelength)
   %current test display
disp(['tuning wavelength instruction ', num2str(n), ' out of
',num2str(length(wavelength))]);

%find frequency of signal thz beam
idlerfreq=c/(wavelength(n)*10^-9);
Thzfreq=abs(pumpfreq-idlerfreq);
freqvector(n)=Thzfreq;

% Function to write a new wavelength to the ICEBLOC (for tcp, send entire
% wavelength vector)
%************************************************************
status = -1;

%Function parameters specific the the ICEBLOC products.
ftp_dir_name = 'M_Squared/'



%Create a temporary file with the wavelength to be uploaded.


if display_flag == 1; disp(['requested wavelength: ',num2str(wavelength(n))]); end;

%write to tcp server

fprintf(tcp_object, ['WAVELENGTH ', num2str(wavelength(n))]);    %Write the
wavelength to tcp server
pause(1.3);
disp(fscanf(tcp_object));

%**********************************************************

% Display result - for debug
% if status == 1
%     disp('Success');
% else
%     disp('Failed!');
% end

%*************Read data from Oscilloscope************************
[X, Y, absintegral] = OscilloscopeRead(deviceObj,Num_of_Averages);
integral = [integral absintegral];
end
fclose(tcp_object);
```

```
delete(tcp_object);
% clear tcp_object;
plot(freqvector,integral)
xlabel('Frequency (Hz)')
ylabel('amplitude (arb. units)')
M=[freqvector integral'];
xlswrite('output.xls',M)

disp('Scan Complete')
%close all device objects
delete([deviceObj interfaceObj]);
```

Read Oscilloscope (part of spectroscopic code)
Titled: “OscilloscopeRead.m”

```
%Code to scan frequencies in Firefly OPO and collect spectrum data from
%oscilloscope connected to a golay cell

function [X, Y, absintegral]=OscilloscopeRead(deviceObj,Num_of_Averages)

% Query property value(s).
get1 = get(deviceObj.Acquisition(1), 'Timebase');
% Set property value(s).
% set(deviceObj.Acquisition(1), 'Timebase', 5.0E-2);


% Execute device object function(s).
groupObj = get(deviceObj, 'Waveform');
groupObj = groupObj(1);
Yarray=[];
Xarray=[];
% Extract waveform
for n = 1:Num_of_Averages
[Y, X, YUNIT, XUNIT] = invoke(groupObj, 'readwaveform', 'channel1');
Yarray=[Yarray; Y];
Xarray=[Xarray; Y];
end
Yave_vector=mean(Yarray);
Yave_vector=Yave_vector-mean(Yave_vector);
disp(['Performed averages: ', num2str(Num_of_Averages)])
absintegral = trapz(X,abs(Yave_vector));
% plot(X,Y)
% xlabel(XUNIT); ylabel(YUNIT);
%ylim([-1 1])
```

APPENDIX E

Interferometer Motor Control Code

Graphical user interface used to control the motor and read an oscilloscope signal

```
function varargout = Motor_GUItest(varargin)
% MOTOR_GUITEST M-file for Motor_GUItest.fig

% Edit the above text to modify the response to help Motor_GUItest

% Last Modified by GUIDE v2.5 07-Mar-2011 13:01:11

% Begin initialization code - DO NOT EDIT
gui_Singleton = 1;
gui_State = struct('gui_Name',       mfilename, ...
                   'gui_Singleton',  gui_Singleton, ...
                   'gui_OpeningFcn', @Motor_GUItest_OpeningFcn, ...
                   'gui_OutputFcn',  @Motor_GUItest_OutputFcn, ...
                   'gui_LayoutFcn',  [] , ...
                   'gui_Callback',   []);
if nargin && ischar(varargin[86])
    gui_State.gui_Callback = str2func(varargin[86]);
end

if nargout
    [varargout{1:nargout}] = gui_mainfcn(gui_State, varargin{:});
else
    gui_mainfcn(gui_State, varargin{:});
end
% End initialization code - DO NOT EDIT


% --- Executes just before Motor_GUItest is made visible.
function Motor_GUItest_OpeningFcn(hObject, eventdata, handles, varargin)
% This function has no output args, see OutputFcn.
% hObject    handle to figure
% eventdata  reserved - to be defined in a future version of MATLAB
% handles    structure with handles and user data (see GUIDATA)
% varargin   command line arguments to Motor_GUItest (see VARARGIN)
set(handles.Direction_buttongroup,'SelectionChangeFcn',@Direction_buttongroup_Selec
tionChangeFcn);
set(handles.Start_Push_Button, 'Enable', 'off');
```

```
set(handles.Stop_Button, 'Enable', 'off');
global STOP_RUNNING
global ARDUINO_CONNECTED
global OSCILLO_CONNECTED
ARDUINO_CONNECTED = 0;   %initialize arduino as disconnected
OSCILLO_CONNECTED = 0;
STOP_RUNNING = 0;
handles.Direction = 'Forward';
set(handles.Record_Scan_CHECKBOX, 'Enable', 'off');

% Choose default command line output for Motor_GUItest
handles.output = hObject;

% set(hObject,'toolbar','figure');    %Not necessary... only for figure tools
% Update handles structure
guidata(hObject, handles);

% UIWAIT makes Motor_GUItest wait for user response (see UIRESUME)
% uiwait(handles.figure1);


% --- Outputs from this function are returned to the command line.
function varargout = Motor_GUItest_OutputFcn(hObject, eventdata, handles)
% varargout  cell array for returning output args (see VARARGOUT);
% hObject    handle to figure
% eventdata  reserved - to be defined in a future version of MATLAB
% handles    structure with handles and user data (see GUIDATA)

% Get default command line output from handles structure
varargout{1} = handles.output;


% --- Executes on button press in Start_Push_Button.
function Start_Push_Button_Callback(hObject, eventdata, handles)
% hObject    handle to Start_Push_Button (see GCBO)
% eventdata  reserved - to be defined in a future version of MATLAB
% handles    structure with handles and user data (see GUIDATA)
%matlab script to control motor
global STOP_RUNNING
global ARDUINO_CONNECTED
STOP_RUNNING = 0;  %allow start running if stopped before
set(handles.Start_Push_Button, 'Enable', 'off');       %Disable button after press
set(handles.Status_STATICtext, 'String', 'Status: Running');
Total_Steps=str2num(get(handles.Number_of_Steps, 'String'));
number_of_steps=Total_Steps;
Steps_Between_Measure = str2num(get(handles.Edit_Steps_Between_Measure,
'String'));
if isempty(Steps_Between_Measure)      %set default value of steps
   Steps_Between_Measure = 1;
```

```
end
global arduino_OBJECT
motordirection = get(get(handles.Direction_buttongroup,'SelectedObject'),'Tag')
interferPlotting= get(handles.Record_Scan_CHECKBOX, 'Value');

Step_Motor(arduino_OBJECT,motordirection,number_of_steps,Steps_Between_Measur
e, interferPlotting, hObject, eventdata, handles);
Is_GUI_Open=handles.figure1; %check if open
axes(handles.axes1);


if interferPlotting == 0;
    for n=1:5
        x=0;
        y=rand(1);
        plot(x,y); pause(0.5);
        for k=0:20
            x=[x , length(x)+1];
            y=[y , rand(1)];
            plot(x,y); pause(0.5);
            if STOP_RUNNING == 1; break; end;
        end

        if STOP_RUNNING ==1; break; end
    end
end
% n=0;
%     while n<5 && STOP_RUNNING ~= 1 && ishandle(Is_GUI_Open)
%     if STOP_RUNNING == 1; break; end; plot(sin(1:0.01:Total_Steps)); pause(0.5);
%     if STOP_RUNNING == 1; break; end; plot(sin(1:0.01:2*Total_Steps)); pause(0.5);
%     if STOP_RUNNING == 1; break; end; plot(sin(1:0.01:3*Total_Steps)); pause(0.5);
%     n=n+1;
%     end

if STOP_RUNNING ~= 1 && ishandle(Is_GUI_Open)
    set(handles.Status_STATICtext, 'String', 'Status: Completed');
    set(handles.Start_Push_Button, 'Enable', 'on');
    guidata(hObject,handles);
else if ~ishandle(Is_GUI_Open) && ARDUINO_CONNECTED  %if still connected to
arduino
        delete(arduino_OBJECT);
        disp('Scan interrupted, arduino disconnected')
    end
end


function Number_of_Steps_Callback(hObject, eventdata, handles)
% hObject    handle to Number_of_Steps (see GCBO)
% eventdata  reserved - to be defined in a future version of MATLAB
```

```
% handles    structure with handles and user data (see GUIDATA)
input1 = str2num(get(hObject, 'String'));
if isempty(input1)
   set(hObject, 'String', '0');
end
guidata(hObject, handles);
% Hints: get(hObject,'String') returns contents of Number_of_Steps as text
%        str2double(get(hObject,'String')) returns contents of Number_of_Steps as a double


% --- Executes during object creation, after setting all properties.
function Number_of_Steps_CreateFcn(hObject, eventdata, handles)

if ispc && isequal(get(hObject,'BackgroundColor'),
get(0,'defaultUicontrolBackgroundColor'))
   set(hObject,'BackgroundColor','white');
end



% --- Executes on button press in Pause_Button.
function Pause_Button_Callback(hObject, eventdata, handles)
% hObject    handle to Pause_Button (see GCBO)
% eventdata  reserved - to be defined in a future version of MATLAB
% handles    structure with handles and user data (see GUIDATA)
global STOP_RUNNING
if STOP_RUNNING ~=1         %only pause if not already stopped by button
   set(handles.Status_STATICtext, 'String', 'Status: Paused');
   uiwait(handles.figure1);
end

% --- Executes on button press in Resume_Button.
function Resume_Button_Callback(hObject, eventdata, handles)
global STOP_RUNNING
if STOP_RUNNING ~=1
   set(handles.Status_STATICtext, 'String', 'Status: Running');
   uiresume(handles.figure1);
end




%*****************motor control*******************8
%matlab motor control function
function [] = Step_Motor(a, DirectTEXT, number_of_steps, Steps_Between_Measure,
interferPlotting, hObject, eventdata, handles)

global STOP_RUNNING

if strcmp(DirectTEXT,'Forward_Radio_Button')
   Direction = 1;
```

```
else if strcmp(DirectTEXT,'Backward_Radio_Button')
        Direction = 0;
    end
end
a.digitalWrite(3,Direction);    %give direction instruction to pin 3
Countdown_to_Measure=0;         %initialize counter
x=[];                           %initialize growing, plotting x vector
y=[];                           %initialize growing, plotting y vector
%Step the motor
for current_step = 0:number_of_steps
    if STOP_RUNNING == 1  %stop running if button pressed
        return
    end
            %update step monitor in the GUI to current step
    set(handles.Current_StepText, 'String', num2str(current_step));
    pause(0.001);            %allow time for GUI to update

     %********perform motor stepping by controllin pin 2 high and low
     if current_step ~=0        %don't step initially.
    a.digitalWrite(2,1);
    pause(0.01);        %pause is 0.01 normally
    a.digitalWrite(2,0);
    pause(0.01);
     end
    %**********perform countdown of steps until measurement*****
    if Countdown_to_Measure == Steps_Between_Measure || current_step == 0;   %take
data at intervals and once at beginning
        if interferPlotting == 1
            disp('Taking a measurement on Oscilloscope')
            [X, Y, absintegral]=OscilloscopeRead(handles.deviceObj,1);
            pause(0.5);
        x=[x, current_step];
        y=[y, absintegral];
        plot(x,y);
        end
        Countdown_to_Measure = 0;  %reset counter if reached the desired number
    end

    %***********Update the counter*************
     Countdown_to_Measure = Countdown_to_Measure + 1;       %Update Counter
end

%     guidata(hObject, handles);         %not necessary?
 interferPlotting= get(handles.Record_Scan_CHECKBOX, 'Value');
 if interferPlotting == 1;

Matrix = [x;y]';     %create data array to output to file
csvwrite('interferometer output.csv',Matrix);
%perform FFT calculation
```

```
[FFT_intensity frequency] = FFT(x,y);
freqMatrix = [frequency; FFT_intensity]';
csvwrite('FFT output.csv',freqMatrix);
 end
disp(['number of steps taken: ', num2str(number_of_steps)]);


function Direction_buttongroup_SelectionChangeFcn(hObject, eventdata)

%retrieve GUI data, i.e. the handles structure
handles = guidata(hObject);

switch get(eventdata.NewValue,'Tag')   % Get Tag of selected object
   case 'Forward_Radio_Button'
     %execute this code when fontsize08_radiobutton is selected
     handles.Direction = 'Forward';

   case 'Backward_Radio_Button'
     %execute this code when fontsize12_radiobutton is selected
     handles.Direction = 'Backward';

   otherwise
      % Code for when there is no match.
       handles.Direction = 1;
end

%updates the handles structure
guidata(hObject, handles);

% --------------------------------------------------------------------
function File_Callback(hObject, eventdata, handles)
% hObject    handle to File (see GCBO)
% eventdata  reserved - to be defined in a future version of MATLAB
% handles    structure with handles and user data (see GUIDATA)


% --------------------------------------------------------------------
function Close_Callback(hObject, eventdata, handles)
% hObject    handle to Close (see GCBO)
% eventdata  reserved - to be defined in a future version of MATLAB
% handles    structure with handles and user data (see GUIDATA)
global ARDUINO_CONNECTED
global OSCILLO_CONNECTED           %invoke global variables.
global arduino_OBJECT
global STOP_RUNNING
selection = questdlg(['Close ' get(handles.figure1,'Name') '?'],...
                     ['Close ' get(handles.figure1,'Name') '...'],...
                     'Yes','No','Yes');
if strcmp(selection,'No')
```

```
    return;
end

STOP_RUNNING=1;
delete(handles.figure1)
if OSCILLO_CONNECTED
  delete([handles.deviceObj handles.interfaceObj]);       %Disconnects for oscilloscope
  disp('Oscilloscope disconnected in exit proceedure')
end
if ARDUINO_CONNECTED
delete(arduino_OBJECT);            %disconnect from arduino board
clear('arduino_OBJECT');
disp('completed and disconnected');
end


function Edit_Steps_Between_Measure_Callback(hObject, eventdata, handles)

% Hints: get(hObject,'String') returns contents of Edit_Steps_Between_Measure as text
%        str2double(get(hObject,'String')) returns contents of
Edit_Steps_Between_Measure as a double


% --- Executes during object creation, after setting all properties.
function Edit_Steps_Between_Measure_CreateFcn(hObject, eventdata, handles)

if ispc && isequal(get(hObject,'BackgroundColor'),
get(0,'defaultUicontrolBackgroundColor'))
    set(hObject,'BackgroundColor','white');
end


% --- Executes on button press in Record_Scan_CHECKBOX.
function Record_Scan_CHECKBOX_Callback(hObject, eventdata, handles)


% --- Executes on button press in Stop_Button.
function Stop_Button_Callback(hObject, eventdata, handles)
global STOP_RUNNING
STOP_RUNNING=1;
set(handles.Status_STATICtext, 'String', 'Status: Stopped');
set(handles.Start_Push_Button, 'Enable', 'on');


% --- Executes on button press in Connect_Oscillo_Push_Button.
function Connect_Oscillo_Push_Button_Callback(hObject, eventdata, handles)
global OSCILLO_CONNECTED
if ~OSCILLO_CONNECTED
    set(handles.Connect_Oscillo_Push_Button, 'String', 'Please Wait');
```

```
   set(handles.Connect_Oscillo_Push_Button, 'Enable', 'off');
   pause(0.01);        %give GUI time to adjust
   [handles.interfaceObj handles.deviceObj] = Connect_Oscilloscope;
   set(handles.Record_Scan_CHECKBOX, 'Enable', 'on');
   set(handles.Connect_Oscillo_STATICtext, 'String', 'Oscilloscope: Connected');
   OSCILLO_CONNECTED = 1;
   guidata(hObject, handles);    %update handles
   set(handles.Connect_Oscillo_Push_Button, 'String', 'Disconnect');
   set(handles.Connect_Oscillo_Push_Button, 'Enable', 'on');
else if OSCILLO_CONNECTED
      delete([handles.deviceObj handles.interfaceObj]);        %Disconnects for
oscilloscope
         set(handles.Connect_Oscillo_Push_Button, 'String', 'Connect');
         set(handles.Record_Scan_CHECKBOX, 'Enable', 'off');
         set(handles.Connect_Oscillo_STATICtext, 'String', 'Oscilloscope: Disconnected');
         OSCILLO_CONNECTED = 0;      %disconnect the oscilloscope
         set(handles.Record_Scan_CHECKBOX, 'Value', 0);

   end
end

% --- Executes on button press in Connect_Arduino_Push_Button.
function Connect_Arduino_Push_Button_Callback(hObject, eventdata, handles)
global ARDUINO_CONNECTED
global arduino_OBJECT;
if ~ARDUINO_CONNECTED
   set(handles.Connect_Arduino_Push_Button, 'String', 'Please Wait');
   set(handles.Connect_Arduino_Push_Button, 'Enable', 'off');
   pause(0.01);                          %allow GUI to update
   arduino_OBJECT=arduino('COM9');          %connect to board
   %set pin modes
   arduino_OBJECT.pinMode(2,'output');      %step pin
   arduino_OBJECT.pinMode(3,'output');      %direction pin
   ARDUINO_CONNECTED=1;
   set(handles.Connect_Arduino_STATICtext, 'String', 'Stepper Motor Control:
Connected');
   set(handles.Start_Push_Button, 'Enable', 'on');
   set(handles.Stop_Button, 'Enable', 'on');
   %use delete(instrfindall) to disconnect in case of problems
      set(handles.Connect_Arduino_Push_Button, 'Enable', 'on');
   set(handles.Connect_Arduino_Push_Button, 'String', 'Disconnect');
else if ARDUINO_CONNECTED == 1;
      set(handles.Connect_Arduino_Push_Button, 'String', 'Please Wait');
      delete(arduino_OBJECT);
      ARDUINO_CONNECTED = 0;
         set(handles.Connect_Arduino_Push_Button, 'String', 'Connect');
         set(handles.Connect_Arduino_STATICtext, 'String', 'Stepper Motor Control:
Disconnected');
            set(handles.Start_Push_Button, 'Enable', 'off');
```

```
            set(handles.Stop_Button, 'Enable', 'off');
        disp('Arduino disconnected');
    end
end

function [interfaceObj deviceObj] = Connect_Oscilloscope()
%****************Initialize USB interface with Oscilloscope***********
% Create a VISA-USB object.
interfaceObj = instrfind('Type', 'visa-usb', 'RsrcName',
'USB0::0x0699::0x0372::C010455::0::INSTR', 'Tag', '');

% Create the VISA-USB object if it does not exist
% otherwise use the object that was found.
if isempty(interfaceObj)
    interfaceObj = visa('NI', 'USB0::0x0699::0x0372::C010455::0::INSTR');
    disp('oscilloscope interface configured')
else
    fclose(interfaceObj);
    interfaceObj = interfaceObj(1);
end

% Create a device object.
% deviceObj = icdevice('tektronix_tds2012.mdd', interfaceObj);
deviceObj = icdevice('DPO2012custom.mdd', interfaceObj);

set(interfaceObj, 'InputBufferSize', 3000000);

% Connect device object to hardware.
connect(deviceObj);
disp('connected to oscilloscope successfully')
% Query property value(s).
 get1 = get(deviceObj.Waveform(1), 'EndingPoint');
 disp(get1);
% Configure property value(s).
set(deviceObj.Waveform(1), 'EndingPoint', 1000000.0);




function [X, Y, absintegral]=OscilloscopeRead(deviceObj,Num_of_Averages)

% Query property value(s).
get1 = get(deviceObj.Acquisition(1), 'Timebase');
% Set property value(s).
% set(deviceObj.Acquisition(1), 'Timebase', 5.0E-2);


% Execute device object function(s).
groupObj = get(deviceObj, 'Waveform');
```

```
groupObj = groupObj(1);
Yarray=[];
Xarray=[];
% Extract waveform
for n = 1:Num_of_Averages
[Y, X, YUNIT, XUNIT] = invoke(groupObj, 'readwaveform', 'channel1');
Yarray=[Yarray; Y];
Xarray=[Xarray; Y];
end
if Num_of_Averages == 1;
   Yave_vector=Yarray;
else
Yave_vector=mean(Yarray);
Yave_vector=Yave_vector-mean(Yave_vector);
end
disp(['Performed averages: ', num2str(Num_of_Averages)])
absintegral = trapz(X,abs(Yave_vector));
% plot(X,Y)
% pause(0.2);



function [intensity, frequency]= FFT(x,y)
c=299792458;            %speed of light
motor_step_size= 2.5E-6;      %microns for full steps
y1=y;
d= x.*motor_step_size;
t = d./c;   %convert distance into time
dt=t(2)-t(1);              %sample time (distance between datapoints)

%Figures 8 and 9 can be used to help debug problems and alignment issues during scans

% figure(8)

% hold on
% plot(t,y1)
% xlabel('time');
n=length(y1);

L=n*500;           %number of data points *(multiply to get higher resolution)
Fs=1/dt;              %sampling frequency
NFFT = 2^nextpow2(L);   % Next power of 2 from length of y
Y1 = fft(y1,NFFT);
f1 = Fs/2*linspace(0,1,NFFT/2);

% Plot single-sided amplitude spectrum for sample wave.
figure(9)
% % hold on         %if plotting multiple functions
% xlim([0 2E12])
```

```
plot(f1,2*abs(Y1(1:NFFT/2)))
xlabel('Frequency (Hz)')
% ylabel('Intensity')
title('FFT result')

intensity = 2*abs(Y1(1:NFFT/2));
frequency = f1;
```

APPENDIX F

Photographs of Circuit Designs for THz Video Camera

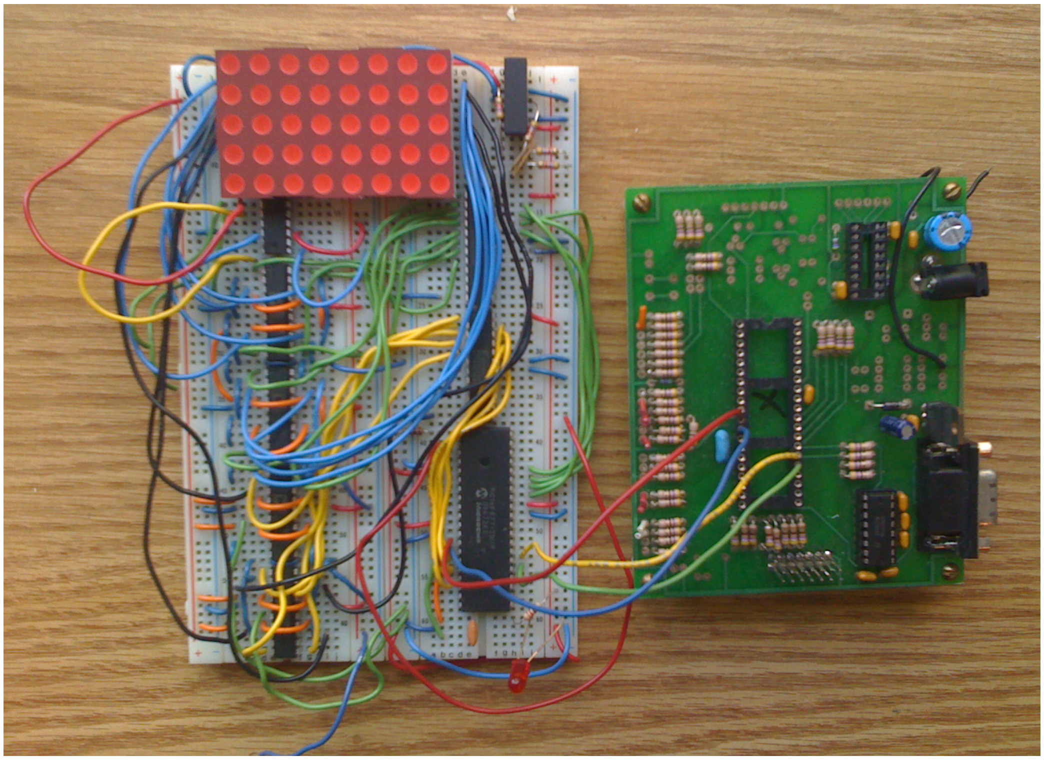

Figure F1: Photograph of first circuit design utilizing the PIC16 microcontroller

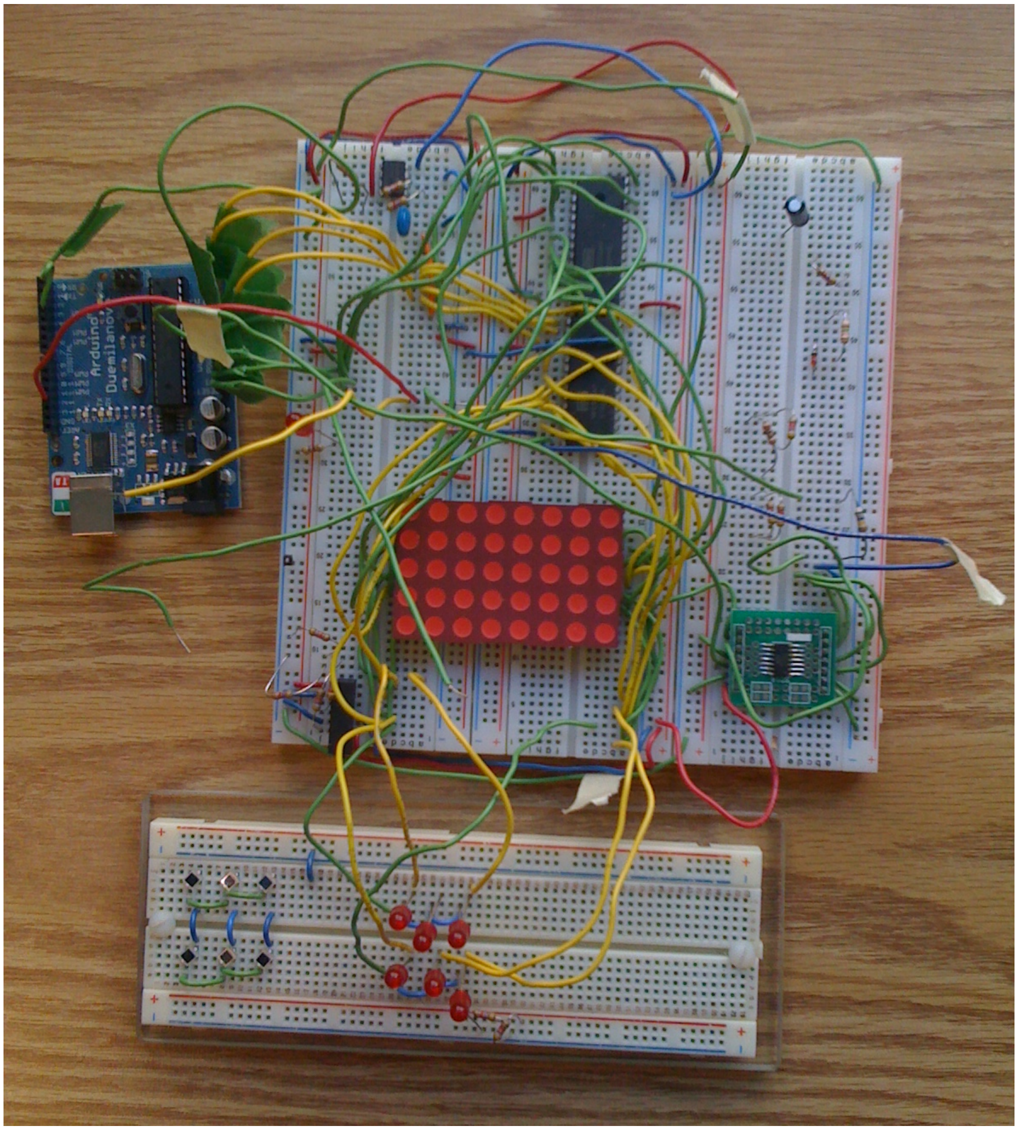

Figure F2: Photograph of second circuit design utilizing the Arduino Duemilanove microcontroller board seen on the left. The individual LEDs at the bottom of the photo are in use for this design.